Water mass properties in the Amundsen Sea, Antarctica, using seal-borne tags

A thesis submitted for the degree of Doctor of Philosophy

Helen Mallett

August 2019

Centre for Ocean and Atmospheric Sciences

School of Environmental Sciences

University of East Anglia

Supervised by:

Prof. Karen J. Heywood (University of East Anglia)

Prof. David Stevens (University of East Anglia)

Prof. Mike Fedak (Sea Mammal Research Unit, University of St Andrews)

Dr. Lars Boehme (Sea Mammal Research Unit, University of St Andrews)

Funded by NERC PhD Studentship NE/L002582/1 as part of the EnvEast Doctoral Training Partnership, and as a part of the iSTAR project.

Word count: 24,781

Abstract

Global attention is focused on the melting of the West Antarctic Ice Sheet and the impacts of associated sea level rise. Glaciers in the Amundsen Sea Embayment are some of the biggest contributors, yet difficulty collecting data in this area, especially during winter when harsh weather and ice cover prevent many traditional observation techniques, means detailed understanding of the relevant processes is limited. This thesis presents a dataset of $>$11,000 new seal-borne hydrographic profiles from the summer, autumn and winter seasons of 2014, enabling seasonal comparisons of deep water, and for the first time, the upper ocean. A through evaluation of the quality of the seal tag dataset is presented, along with details of the appropriate corrections. The magnitude of corrections derived from pre-deployment tests suggest that some tag datasets lacking these pre-deployment tests might not meet the stated accuracies. One of the drivers of increased glacial melt in this region is warm Circumpolar Deep Water (CDW) increasingly crossing the continental shelf, and contributing to increased ice mass loss. Seasonal analysis reveals a CDW layer on average 49 db thicker in late winter (August to October) than in late summer (February to April), the reverse seasonality of that seen at moorings in the western trough. This layer contains more heat in winter. In the upper ocean, salinification, cooling and the deepening of the mixed layer begins in or before February, and continues until June/July. The distance to which mooring-top observations can be extrapolated upward into the upper ocean is examined, and found to be between 110 and 230 m, although dependent on local conditions and the depth of the mooring. These observations form a crucial building block for future study on seasonality and variability in the area, and are essential for verifying model simulations of ice shelf melt.

Publication

Chapter 3 has previously been published as a paper in *Geophysical Research Letters*, under the title 'Variation in the distribution and properties of circumpolar deep water in the eastern Amundsen Sea, on seasonal timescales, using seal-borne tags', with co-authors Karen J. Heywood, David P. Stevens, Lars Boehme, Mike Fedak and Fabien Roquet. Writing and analysis was undertaken by H. K. W. Mallett, with comments and input from collaborators. It is included as published, with the addition of the supplementary figures, followed by some additional sections added in order to make full use of the available data.

Mallett, H. K. W., Boehme, L., Fedak, M., Heywood, K. J., Stevens, D. P., & Roquet, F. (2018), Variation in the distribution and properties of circumpolar deep water in the eastern Amundsen Sea, on seasonal timescales, using seal-borne tags, *Geophysical Research Letters*, 45. https://doi.org/10.1029/2018GL077430

Figure 4.18 has previously been published within the paper 'Between the Devil and the Deep Blue Sea: The Role of the Amundsen Sea Continental Shelf in Exchanges between Ocean and Ice Shelves', in *Oceanography* by the authors: Heywood, K., L. Biddle, L. Boehme, P. Dutrieux, M. Fedak, A. Jenkins, R. Kones, J. Kaiser, H. Mallett, A. Naveira Garabato, I. Renfrew, D. Stevens and B. Webber. The figure was created by H. Mallett, with comments and input from collaborators. It is included as published.

Heywood, K., L. Biddle, L. Boehme, P. Dutrieux, M. Fedak, A. Jenkins, R. Kones, J. Kaiser, H. Mallett, A. Naveira Garabato, I. Renfrew, D. Stevens and B. Webber (2016), Between the Devil and the Deep Blue Sea: The Role of the Amundsen Sea Continental Shelf in Exchanges between Ocean and Ice Shelves, *Oceanography*, 29(4), 118-129.

Acknowledgements

Thanks to the crew of the JCR and the iSTAR team, Simon Moss for seal tagging, and of course the seals, without whom there would be nothing to write about.

To Karen and Dave for your endless patience and perseverance, and for all of the guidance. To Lars and Fedak for all of the above and for providing the opportunity to spend time with some seals face to furry face, to Fabien too, for your help with all things tag, and to Andy, for giving me the chance to see the icy beauty for myself. To Rob and Mark for managing to make the dreaded viva an enjoyable experience.

To Marina, Peter, Dennis, Michael, Stuart and Elise, and the rest of 3.16, for the Portuguese swearing, the belly laughs, the late-night dancing and the early morning boot camps, and to Marina and Elise for those saxophone lessons, and not minding that my teaching style apparently consists of hysterical laughing and youtube.

To Avani, George, Sara and Bobble for still inviting me to play even when I'm grumpy, and for not talking about science. To Rosie and Chris for giving some perspective in the low moments, and to Rosie, so much, for sharing the struggle(s).

Thanks for putting up with me Chris, and always giving me the stare when I'm procrastinating. For apparently inexhaustible patience talking through my frustrations and for reminding me how nice exercise is. To Julia and Jos for your repeated requests for something to proofread, and to Anna for distracting you. To Jo and John for getting me there, and the supportive phone calls, and to Marjorie for providing an example of a liberating back-up plan.

And to the roller derby kids, for keeping me on the round and narrow for the home straight, and to the great bourbon biscuit factory, and your endless supply of surprisingly vegan fuel.

Acronyms

AABW - Antarctic Bottom Water

AASW - Antarctic Surface Water

ACC - Antarctic Circumpolar Current

AIS - Abbott Ice Shelf

ASO - August, September, October

BI - Burke Island

CDW - Circumpolar Deep Water

CoIS - Cosgrove Ice Shelf

CrIS - Crosson Ice Shelf

CT - Central Trough

CTD - Conductivity-Temperature-Depth

CTD-SDRL - Conductivity-Temperature-Depth - Satellite Relayed Data Logger

DMQC - Delayed Mode Quality Control

EI - Edwards Islands

EIS - Eastern Ice Shelf

ET - Eastern Trough

FMA - February, March, April

IBCSO - International Bathymetric Chart of the Southern Ocean

IMM - Interacting Multiple Model

iSTAR - Investigating the Stability of the West Antarctic Ice Sheet

LCDW - Lower Circumpolar Deep Water

MASTS - The Marine Alliance for Science and Technology for Scotland

mCDW - modified Circumpolar Deep Water

MEOP - Marine Animals Exploring the Oceans Pole to Pole

MJJ - May, June, July

MLD - Mixed Layer Depth

NEAS - North Eastern Amundsen Sea

NERC - UK Natural Environment Research Council

OASIIS - Observing and Understanding the Ocean below Antarctic Sea Ice and Ice

Shelves

ORCHESTRA - Ocean Regulation of Climate through Heat and Carbon Sequestration and Transports

PIB - Pine Island Bay

PIB-C - Pine Island Bay - Central

PIB-N - Pine Island Bay North mooring (ISTAR8)

PIB-NW - Pine Island Bay - North West

PIB-S - Pine Island Bay South mooring (ISTAR9)

PIB-SE - Pine Island Bay - South East

PIG - Pine Island Glacier

PIIS - Pine Island Ice Shelf

PIT - Pine Island Trough

PRT - Platinum Resitance Temperature detector

RMS - Root Mean Square

SOFLUX - Southern Ocean Fluxes

SOOS - Southern Ocean Observing System

SMRU - Sea Mammal Research Unit

SW - Shelf Water

TARSAN - Thwaites-Amundsen Regional Survey and Network Integrating Atmsphere-Ice-Ocean Processes Affecting the Sub-Ice-Shelf Environment

TEOS-10 - The Equation Of State, 2010

TIS - Thwaites Ice Shelf

TS - Temperature - Salinity

UCDW - Upper Circumpolar Deep Water

WAIS - West Antarctic Ice Sheet

WT - Western Trough WW - Winter Water

Contents

List of tables

List of figures

Chapter 1

Introduction

1.1 Introduction

The Amundsen Sea (Figure 1.1) is home to water masses derived from regional and global ocean circulation, influenced by ice shelf melting, sea ice, and the seasonal cycle in air temperatures, wind, and solar radiation. Much attention is focused on the region due to concerns about sea level rise from the thinning of the West Antarctic Ice Sheet (WAIS), which has several glaciers with outlets in the Amundsen Sea. 10% of observed sea level rise is thought to be the result of the thinning of the WAIS (Rignot *et al.*, 2008). There are suggestions that freshening of the Ross Sea caused remotely by the melting of the WAIS (Nakayama *et al.*, 2014) could lead to changes in the characteristics of the Antarctic Bottom Water (AABW) formed there, perhaps affecting global thermohaline circulation (Jacobs *et al.*, 2002; Rintoul, 2007; Dinniman *et al.*, 2018). Despite this, relatively little is known about the water masses in the Amundsen Sea, especially during the winter season. For instance, it is hypothesised that warm Circumpolar Deep Water (CDW) crosses the continental shelf from the open ocean to the ice shelves and provides heat for melting from below, but how does it get to the ice shelf, how variable is it in space and in time, and what are the details of the seasonal cycle? These knowledge gaps are in great part due to the inaccessibility of the region, which is remote and covered with sea ice in winter, making it hard to get ship based measurements. Other data collection techniques are also difficult to use in these conditions, or are restricted, for example deploying and recovering moorings requires ice-free access over the mooring site, and moorings cannot be full depth where icebergs might drag the moorings as they pass.

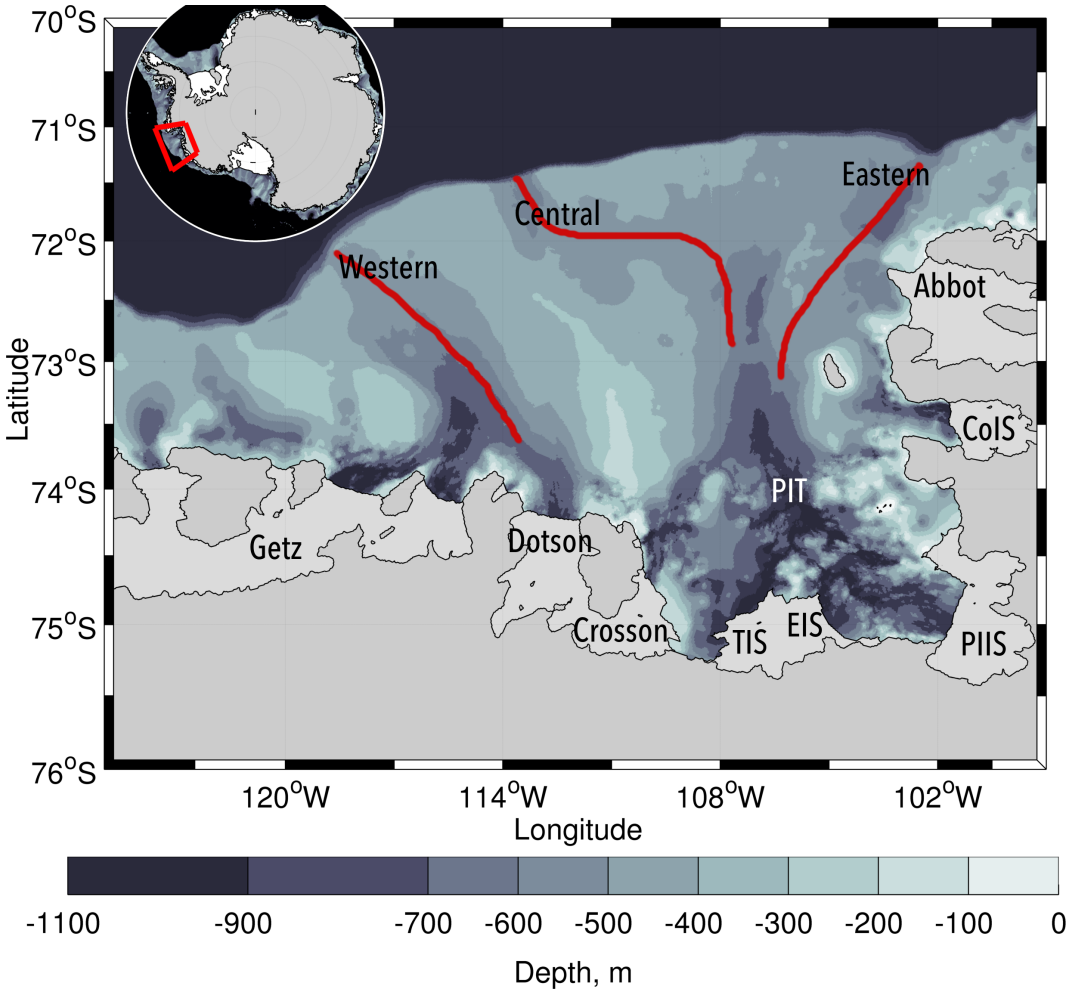

Figure 1.1: Bathymetry of the Amundsen Sea. Marked are the three submarine troughs (red). Also marked are Getz Ice Shelf (Getz), Dotson Ice Shelf (Dotson), Crosson Ice Shelf (Crosson), Thwaites Ice Shelf (TIS), Eastern Ice Shelf (EIS, often considered a part of Thwaites), Pine Island Ice Shelf (PIIS), Cosgrove Ice Shelf (CoIS), Abbot Ice Shelf (Abbot) and Pine Island Trough (PIT). Inset is location within Antarctica. Bathymetry is IBCSO (Arndt *et al.*, 2013), and coastline and grounding line are Bedmap2 in white and grey (Fretwell *et al.*, 2013). IBCSO = International Bathymetric Chart of the Southern Ocean.

The Amundsen Sea has three submarine troughs, here described as the western, central and eastern (Figure 1.1, red lines). Also marked in Figure 1.1 are the locations of the ice shelves and Pine Island Trough (PIT).

1.2 Water masses of the Amundsen Sea

The CDW is the deeper part of the Antarctic Circumpolar Current (ACC), an eastward current circling Antarctica (Orsi *et al.*, 1995). At between 300 and approximately 3000

m depth and with potential temperatures between 0°C and 2°C the CDW is warmer than the surface water above. Salinities are between 34.67 and 34.75, also greater than in the surface water above. In the Amundsen Sea, and other Antarctic coastal zones, the CDW mixes with local shelf waters to form the Modified Circumpolar Deep Water (MCDW). The CDW can be split into upper (UCDW) and lower (LCDW) parts, where the former has low oxygen and high nutrient concentrations, and the latter higher salinities (Orsi *et al.* (1995), figure 1.2 (Walker *et al.* (2013))).

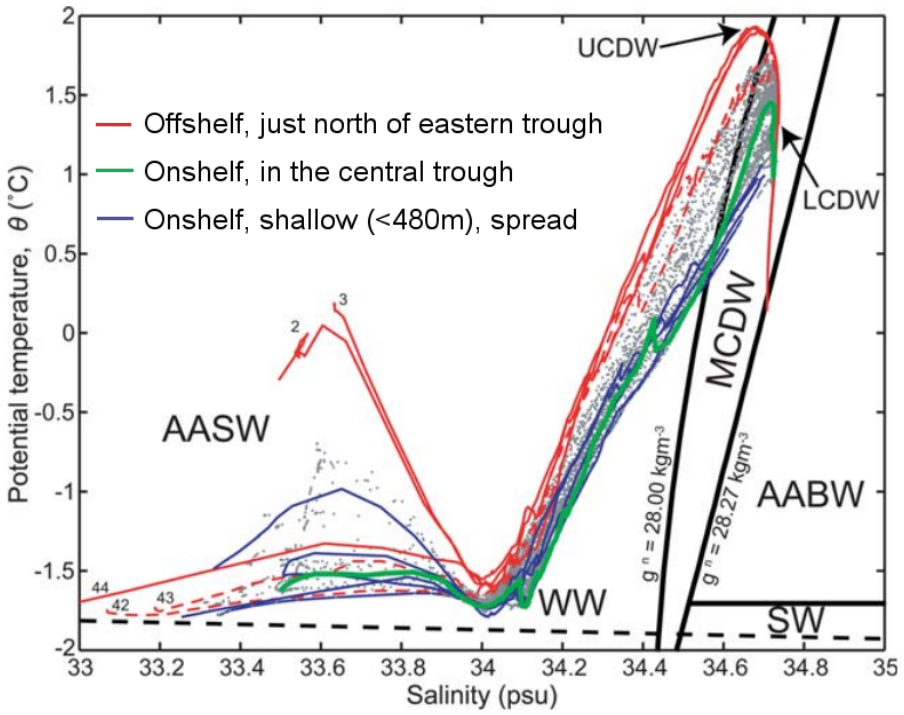

Figure 1.2: Water mass properties in the Amundsen Sea. Potential temperature and practical salinity of sample Amundsen Sea continental shelf CTD profiles (March 2003, all but red), with water masses marked. In red are CTD profiles from the continental shelf slope to the north east of the Amundsen Sea. Antarctic Surface Water - AASW, Winter Water - WW, Shelf Water - SW, Antarctic Bottom Water - AABW, Modified Circumpolar Deep Water - MCDW, Lower Circumpolar Deep Water - LCDW, and Upper Circumpolar Deep Water - UCDW. Note greater temperatures and salinities of CDW waters. Adapted from Walker *et al.* (2013).

Wåhlin *et al.* (2010) consider the structure of Amundsen Sea water masses in the western trough to be Antarctic Surface Water (AASW), including Winter Water (WW), down to 200 - 400 m depth with neutral density γN $<$28.03kg m^{-3} (Whitworth III *et al.*, 1998). At the shelf sea floor, MCDW inflow approximately 60 m thick enters along the eastern flank of the western trough, with γN $>$28.27 kg m^{-3} (Whitworth III *et al.*, 1998). The

remaining water mass between is named MCDW-meltwater, a layer approximately 150 m thick of MCDW mixed with ice-shelf meltwater. MCDW-meltwater is distinguished by neutral density 28.03 $<\gamma$N $<$28.27 kg m^{-3} (Whitworth III *et al.*, 1998), temperature T $\approx$ 0°C, salinity S $\approx$ 34.3 (practical salinity) and dissolved oxygen O_2 $<$4.8 mL/L (Wåhlin *et al.*, 2010). Most of the literature does not make this distinction (for many observations, dissolved oxygen measurements are not available), and refers simply to warm salty CDW or MCDW on the shelf.

1.2.1 MCDW source water: UCDW or LCDW?

Wåhlin *et al.* (2013) use observations in the western and central troughs from 2008 to 2012, along with prior historical data from across the Amundsen Sea and offshelf (Figure 1.3, top right panel), plotted against mixing lines between glacier meltwater and LCDW (Figure 1.3 panel b, red dashed line) and between glacier meltwater and UCDW (Figure 1.3 panel b, black dashed line), to suggest that water on the Amundsen shelf (Figure 1.3 panel a, red points) is a mix between source LCDW and glacier meltwater, and not UCDW.

Nakayama *et al.* (2017) use a regional model including dynamic/thermodynamic sea ice and thermodynamic ice shelves, modeling both UCDW and LCDW in all three troughs in 2006 and 2007. They find more LCDW in the central than the eastern trough, as observed by Nakayama *et al.* (2013), but that the intrusion of UCDW occurs much faster than LCDW.

These studies observe and model different years and different troughs, and it appears that there is variability, if not disagreement, on whether LCDW or UCDW or both can be found in each of the three troughs.

1.2.2 CDW circulation

The path of circulation the CDW takes once on the continental shelf is widely debated. Models suggest horizontal circulating cells (Schodlok *et al.*, 2012; St-Laurent *et al.*,

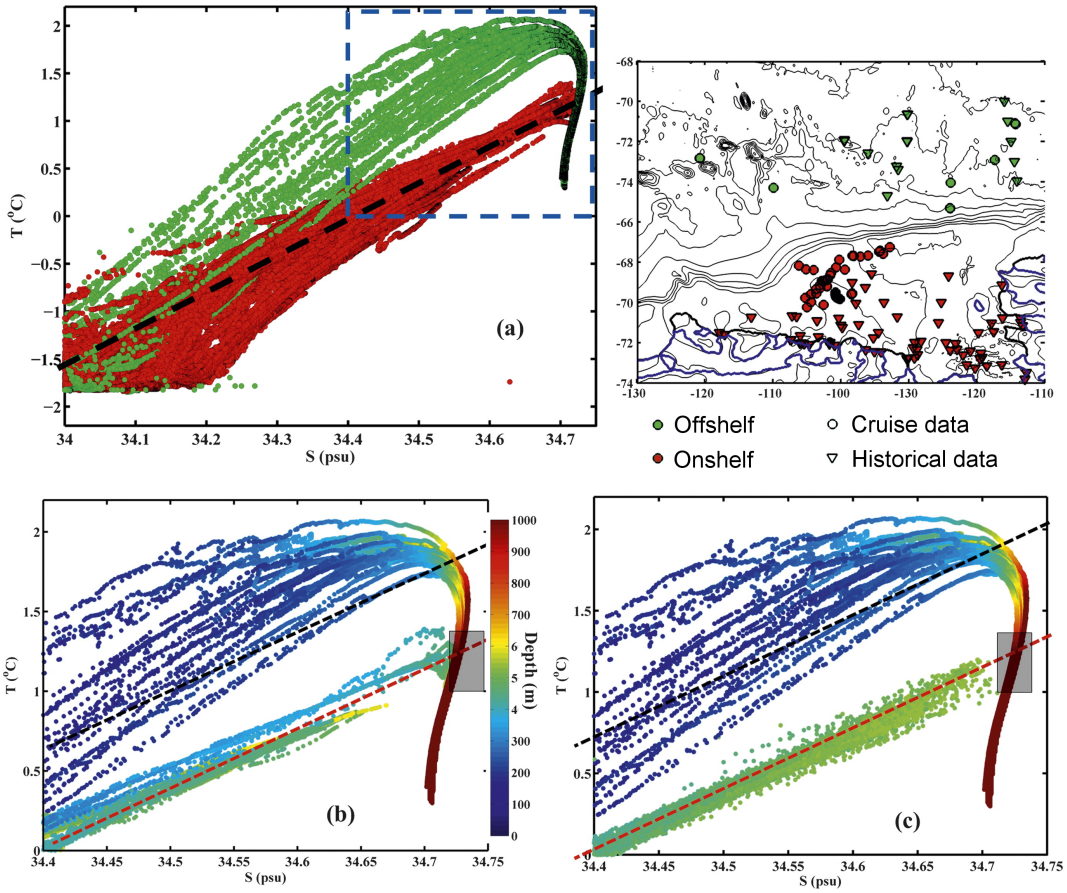

Figure 1.3: T-S diagram for a) Oden (2008/2009) and Aaron cruises (2010/2011 and early 2012), and historical data, on-shelf data - red, off-shelf data - green, dashed blue box shows axes limits for panels b and c, b) historical off-shelf data and Oden & Aaron observations all coloured by depth, c) historical off-shelf data and mooring data all coloured by depth. Dashed lines in b and c are mixing lines between glacier meltwater and UCDW (black) and LCDW (red). Top right panel is a map of cruise data - circles, historical data - triangles, where on-shelf - red, and off-shelf - green. Note the cruise and mooring data lie on the LCDW mixing line. Adapted from Wåhlin *et al.* (2013).

2013), and Mankoff *et al.* (2012) observe a large cyclonic gyre in the Pine Island Bay (PIB) using Landsat data (Figure 1.6c). Wåhlin *et al.* (2013) note that once on the shelf, near bottom flow is forced by gravity, as the dense CDW descends from shallow shelf edge to deep inner shelf troughs. Table A.1 contains details of the models referenced in chapter 1, for convenient comparison.

A pattern of circulation whereby LCDW is forced on the shelf in the eastern trough, primarily by upslope benthic Ekman pumping (Wåhlin *et al.*, 2012, see section 1.4.1), and then flows south to Pine Island Glacier (PIG) forced by gravity, before being mixed with glacial meltwater and following topography northward into the central trough as MCDW-meltwater, is proposed by citetWahlin2013. This circulation pattern is supported

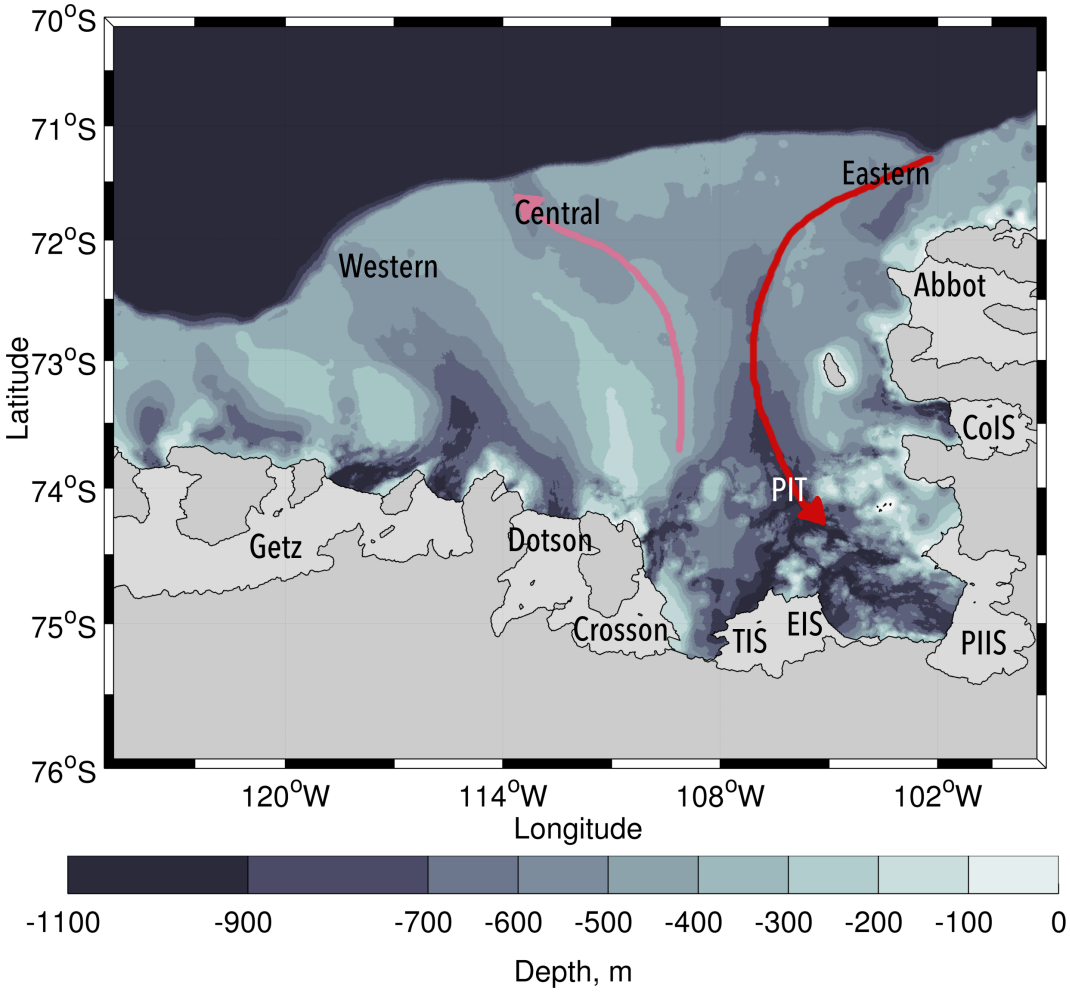

Figure 1.4: Circulation proposed by Wåhlin *et al.* (2013), CDW inflow path (red), where LCDW is forced onto shelf at eastern trough and flows to PIG, mixes with glacial meltwater and then heads north along the mid-shelf ridge (pink), before turning west with topography into the central trough.

by observations of warmer CDW at the east of the shelf, and only fresher, colder CDW in the centre of the shelf (Wåhlin *et al.*, 2012; Jacobs *et al.*, 2012). Nakayama *et al.* (2013) agree that the eastern trough is the entrance point on the shelf for warm CDW, although they also find a colder, denser form of CDW enters at the central trough. They hypothesise that only the dense CDW from the thicker eastern intrusion flows all the way to the PIT, but that it is modified by the central intrusion as it travels (Figure 1.5), reducing the temperature maximum from $\sim$ 1.4 to $\sim$ 1.2 °C. This circulatory theory is derived from observational data over the central and eastern troughs.

In Pine Island Bay a cyclonic gyre brings CDW to the northern edge of the ice shelf cavity, while at the southern edge of the cavity the gyre transports away the majority of

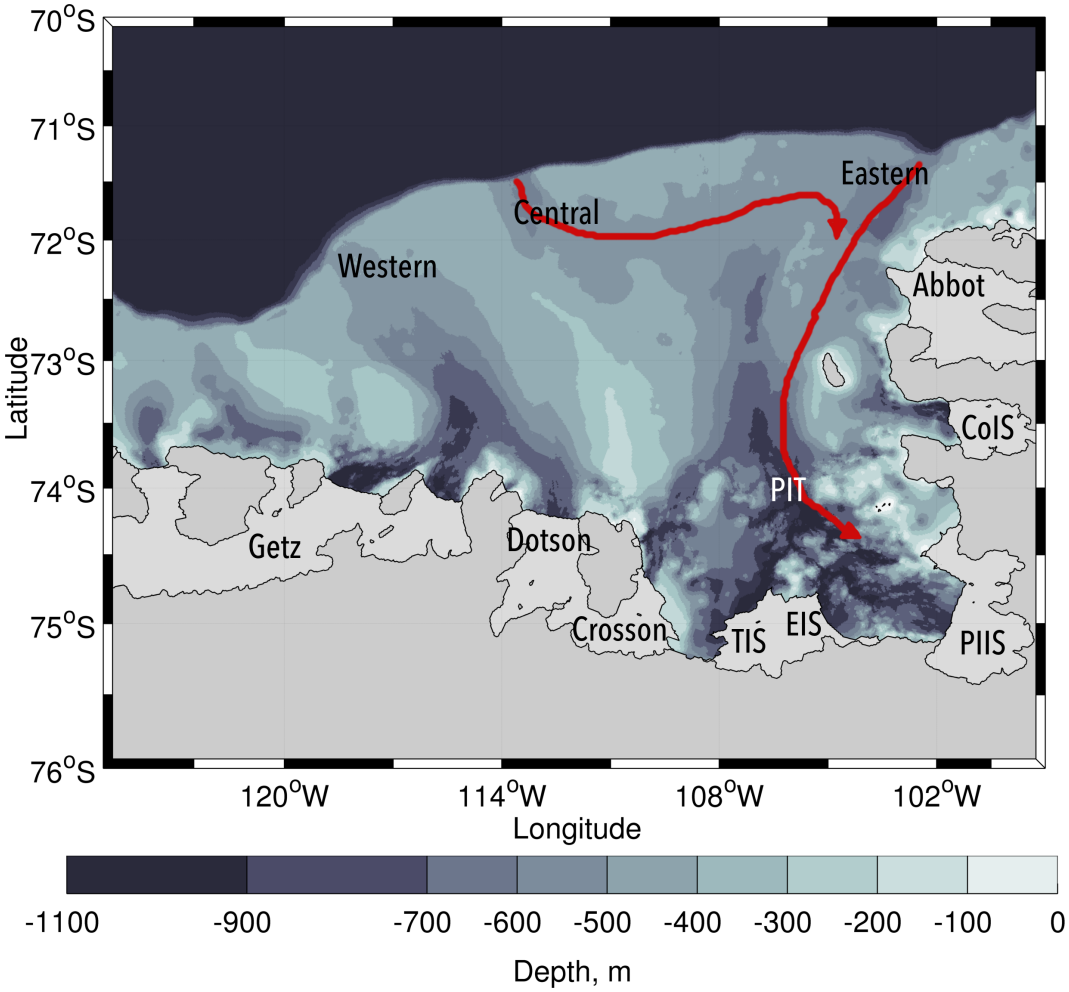

Figure 1.5: Circulation proposed by Nakayama *et al.* (2013) (red), CDW from the eastern trough flows to PIG, modified by CDW from the central trough.

the glacial meltwater (Mankoff *et al.*, 2012, figure 1.6c). This feature has been observed multiple times, in November 2008 by Mankoff *et al.* (2012) using Landsat data (Figure 1.6c), and in January 2009 by Thurnherr *et al.* (2014) using a ship-mounted acoustic Doppler current profiler (Figure 1.6d), but during a cold period from October 2011 to May 2013 Webber *et al.* (2017) observed, using average mooring velocity, a reversal in the direction of flow within PIB (Figure 1.6a,b). In February 2014, Garabato *et al.* (2017) again observed the gyre rotating in the cyclonic direction, using a ship-mounted acoustic Doppler current profiler. Schodlok *et al.* (2012) model, using a high resolution (1km) grid, not only this gyre in PIB, but another at the Dotson and Getz ice shelves, separated from the PIB gyre by the shallow bathymetry between.

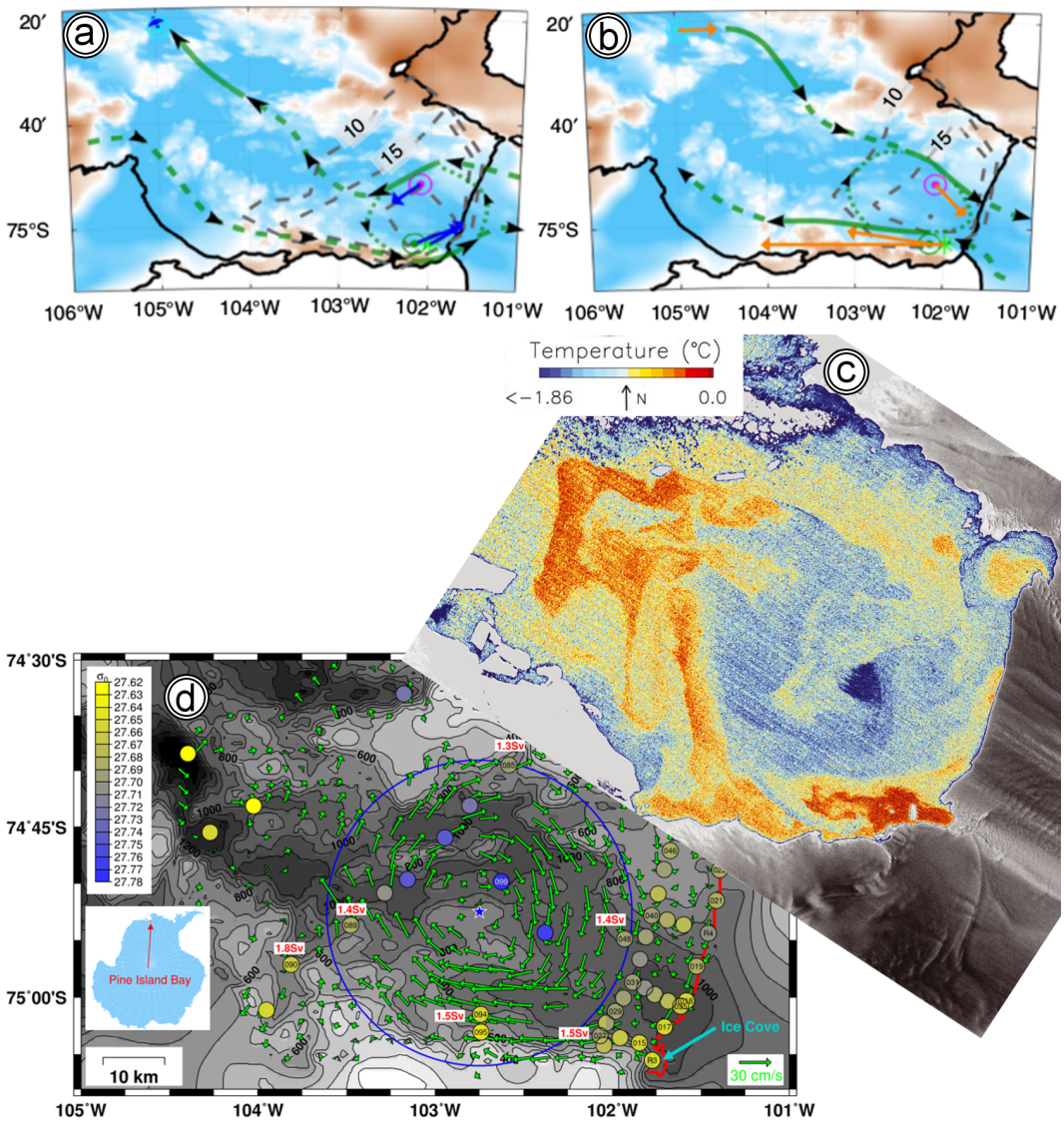

Figure 1.6: PIB gyre as observed by: a) Webber *et al.* (2017) between October 2011 and May 2013 (cold period) using average mooring velocities (moorings marked with pink and green dots and crosses, mooring velocities in blue, schematic flow lines in green). b) as in a), but between May 2013 and February 2014 (mooring velocities in orange). c) Mankoff *et al.* (2012) in November 2008 using Landsat data (rotated so that north points upwards). d) Thurnherr *et al.* (2014) in January 2009 using a ship-mounted acoustic Doppler current profiler, green arrows. Figure adapted from the referenced works.

1.3 Meteorology

The primary meteorological feature over the Amundsen Sea is the Amundsen Sea Low. This pressure low has great variability in both depth and location, and as such is hugely influential on atmospheric circulation in and beyond the Amundsen Sea. The Amundsen Sea Low moves seasonally, from around 110°W in summer, to around 150°W, and a few

degrees southward, in winter (Turner *et al.*, 2017). Interannual variability on these seasonal locations is around 20° in summer and up to 35° in winter (Turner *et al.*, 2017). This variability results from the orography of the continent, teleconnections with the El NioSouthern Oscillation, and sea-surface temperatures (Turner *et al.*, 2017). When the El NioSouthern Oscillation is in the El Nio phase, the Amundsen Sea Low is weaker (Turner, 2004). The depth of the Amundsen Sea Low is influenced by the Southern Annular Mode; the primary mode of climate variability over Antarctica (Thompson and Wallace, 2000). When the Southern Annular Mode is in positive phase, mean sea level pressure is lower in the Amundsen Sea Low.

Various reanalysis products are available, of which Jones *et al.* (2016) conclude that ERA-I has the smallest errors and biases in the near-surface layer, when compared to independent observations from over the Amundsen Sea. For ERA-I there is a cold bias of -1.8C, with biases worse in winter than in summer.

1.4 Inflows and outflows

1.4.1 Shelf-break inflow forcings

The mechanism forcing CDW onto the continental shelf is also an area of debate. Walker *et al.* (2007) suggested that topography is crucial, and that 'any significant depression in the shelf edge [...] would permit a thicker layer of CDW onto the shelf'.

Wind forcing is also considered an important factor. Both observations and models report enhanced inflow at the central trough in winter / spring. Figure 1.7 (bottom left) shows thick CDW presence in winter / spring when wind stress is stronger and more consistently westerly (Walker *et al.*, 2007; Thoma *et al.*, 2008). The model run by Steig *et al.* (2012) also shows increase in westerly wind stress driving inflow of CDW, but instead occuring mostly in autumn and early winter. Jacobs *et al.* (2012) suggest that variation in zonal wind stress may be the primary influence on fluctuations in CDW inflow, given a weak slope front and distant ACC. Thoma *et al.* (2008) also report that seasonal and

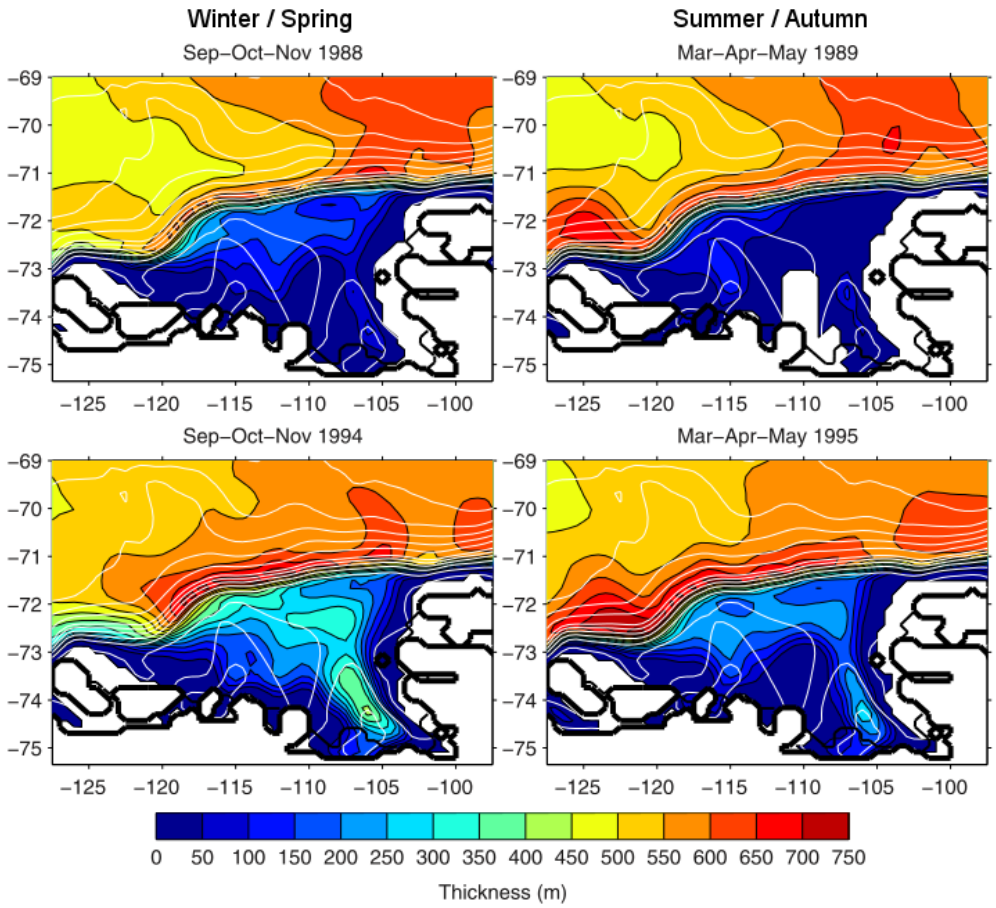

Figure 1.7: Combined thickness of model layers 7 and 8, corresponding to densest, warmest waters, averaged through spring (left) and autumn (right) of two contrasting years. Note very different thicknesses present, and prominence of central and western troughs. Adapted from Thoma *et al.* (2008).

interannual variation in wind stress alters inflow by driving current at the shelf break in different directions, depending on the location of the Amundsen Sea Low, among other factors. Figure 1.7 shows examples of CDW thickness on the continental shelf in two contrasting years. Thoma *et al.* (2008) put forward four possible mechanisms for how these wind driven currents lead to inflow: interaction of eddies with flow over the sloping bathymetry (Adcock and Marshall, 2000), shear induced in the along-slope flow during westerly winds (Johnson and Rockliff, 1986), interaction of variable slope currents with shelf edge topographic irregularites (Klinck, 1996), and Ekman transport of surface waters off-shelf.

More recently, Rodriguez *et al.* (2016) find, using dynamical budgets of a southern ocean model, that cross-shelf transport is primarily geostrophic below the thermocline,

and that local wind-stress curl (distinct from wind stress) may be an important factor, and suggest that this should be compared in future studies to other proposed mechanisms.

Wåhlin *et al.* (2013), who find the deepest shelf waters they sampled at 500 - 600 m to be sourced from LCDW at $\sim$ 1000m depth, suggest two mechanisms for forcing the LCDW up onto the shelf. The first, wind induced upwelling, is as modelled by Thoma *et al.* (2008) and Steig *et al.* (2012). The second is upslope benthic Ekman transport (Wåhlin *et al.*, 2012) induced by deep-reaching eastward currents at the shelf break (Wåhlin *et al.*, 2013). They find that although wind forcing does drive short term variability of the whole sampled water column, it does not drive longer term variability, although they note that the two year dataset is too short to make judgements on seasonal variation.

St-Laurent *et al.* (2013) use an eddy resolving model to identify interactions between shelf break currents and trough geometry as a mechanism for forcing CDW inflow. In a model run considering the interactions between mean flow and topography, an eastward geostrophic shelf break jet flows across a trough entrance and induces cyclonic flow within the trough, a result of which is onshore transport of heat. Another model run allows for topographic waves and results in inflow at the centre of the trough and an absence of cyclonic trough circulation. St-Laurent *et al.* (2013) find three mechanisms for onshore heat transport: melt-driven flow, interaction of mean flow with topography and interaction of a Rossby wave with topography, all leading to heat transport comparable with observations, of the order of 10^{12} GW.

There is no consensus on the key mechanisms forcing CDW inflow. Whilst the seal tag data presented in this thesis are not the most suitable data type for identifying the forcing mechanisms of this inflow (since the seals rarely sample at the shelf break), they are useful in contributing understanding of the temporal and spatial variability over the continental shelf of the parameters (CDW layer thickness, spread, and temperature) used to evaluate these forcing mechanisms.

1.4.2 PIG outflows

Outflows from under the ice shelves are also an important component of the Amundsen Sea water masses. For example, outflow from PIIS flows into PIB in semi-buoyant plumes that reach equilibrium density well below the surface, and are pushed by Coriolis force to accumulate at the south end of the PIG front (Mankoff *et al.*, 2012; Jenkins *et al.*, 2010). Garabato *et al.* (2017) find that outflow from PIIS is predominately through a fast narrow jet at the southern end of the calving front, at speeds exceeding 0.5 m/s. This outflow has elevated turbidity from suspended sediment carried by the glacial meltwater (Jenkins *et al.*, 2010), and may have implications for biological activity at the ice front.

Also at the ice front, upwelling of deep water with remaining heat not used in basal melting may instead melt sea ice and contribute to polynya formation at the calving front (Mankoff *et al.*, 2012), as suggested by the approximately matched locations of historic polynyas and modelled subsurface meltwater outflows (Payne *et al.*, 2007; Mankoff *et al.*, 2012).

1.4.3 Which trough gives the most CDW inflow?

The models ran by Thoma *et al.* (2008) clearly show inflow mainly at the central and partially at the western trough (Figure 1.7). The western trough leads to Dotson and Getz Ice Shelves (Figure 1.1) with a shallower sill, limiting inflow to a thinner, cooler layer (Wåhlin *et al.*, 2010; Walker *et al.*, 2013).

At the central trough, Walker *et al.* (2007) calculate on-shelf heat transport of 2.8 TW, and consider that to be sufficient to explain most of the glacial melting of the Amundsen Sea. However, given that observed outflows from glaciers (see section 1.4.2) carry significant heat content back away from the glaciers, heat supply to the PIG, if not the other glaciers, must be much greater than that required for the glacial melting. Walker *et al.* (2007) also observe a small amount of CDW inflow just east of the central trough, in a thin layer of $\sim$ 70 m. Nakayama *et al.* (2013) deduce that three fifths of the CDW at PIG is from the central trough.

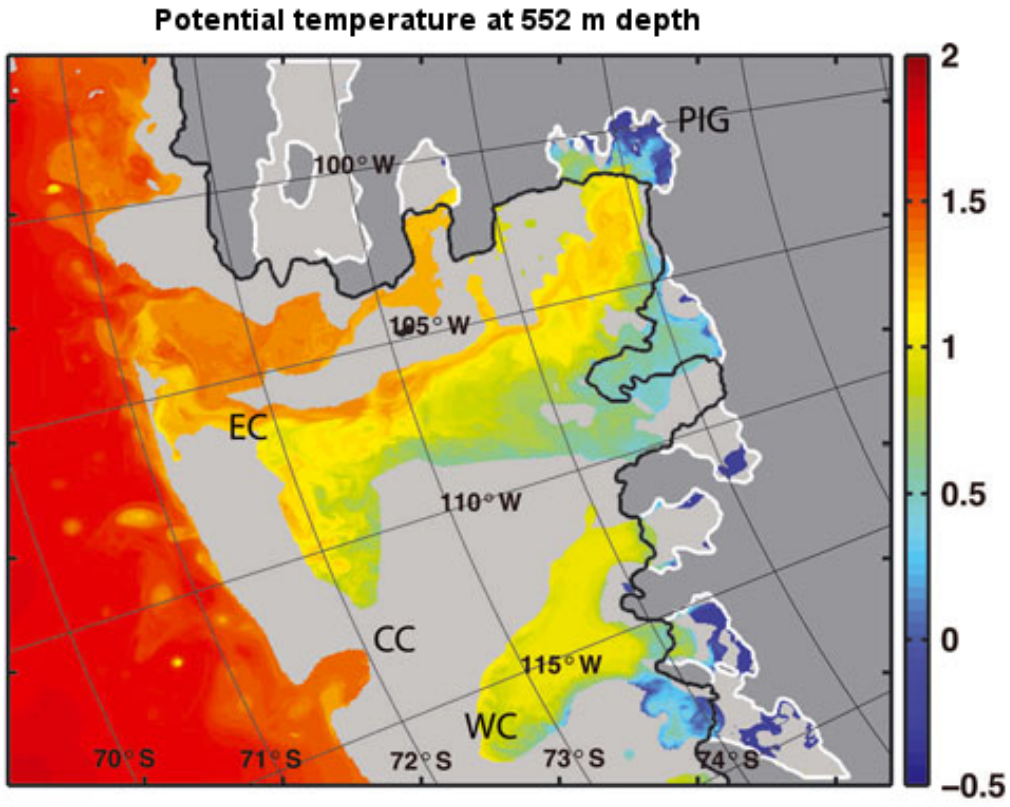

Figure 1.8: Potential temperature (°C) from the model of Schodlok *et al.* (2012), showing CDW path along eastern trough to PIG, with inflow at the central trough limited. x and y axes are model grid spacing in km, EC and CC label the eastern and central troughs. Adapted from Schodlok *et al.* (2012).

The model of Schodlok *et al.* (2012) produces the main intrusions of CDW onto the shelf through the eastern trough (Figure 1.8), and they argue that the small intrusion at the central trough is soon turned back northward by bathymetry and circulation. Jacobs *et al.* (2011) argue that sub-ice circulation is much more important to ice-shelf melting than more distant ocean temperatures.

1.5 Sea ice distribution

In 2014, sea ice concentration is near-total from May to October (mostly 80% or higher, figure 1.9, Cavalieri *et al.* (1996)). A large polynya persists at Thwaites glacier, and a smaller ones at PIG, stretching north along the coastline, and at Getz glacier. From November to April, sea ice cover is much reduced, though much more variable, as sea ice

is formed and then either melted or moved by winds and currents (Figure 1.9).

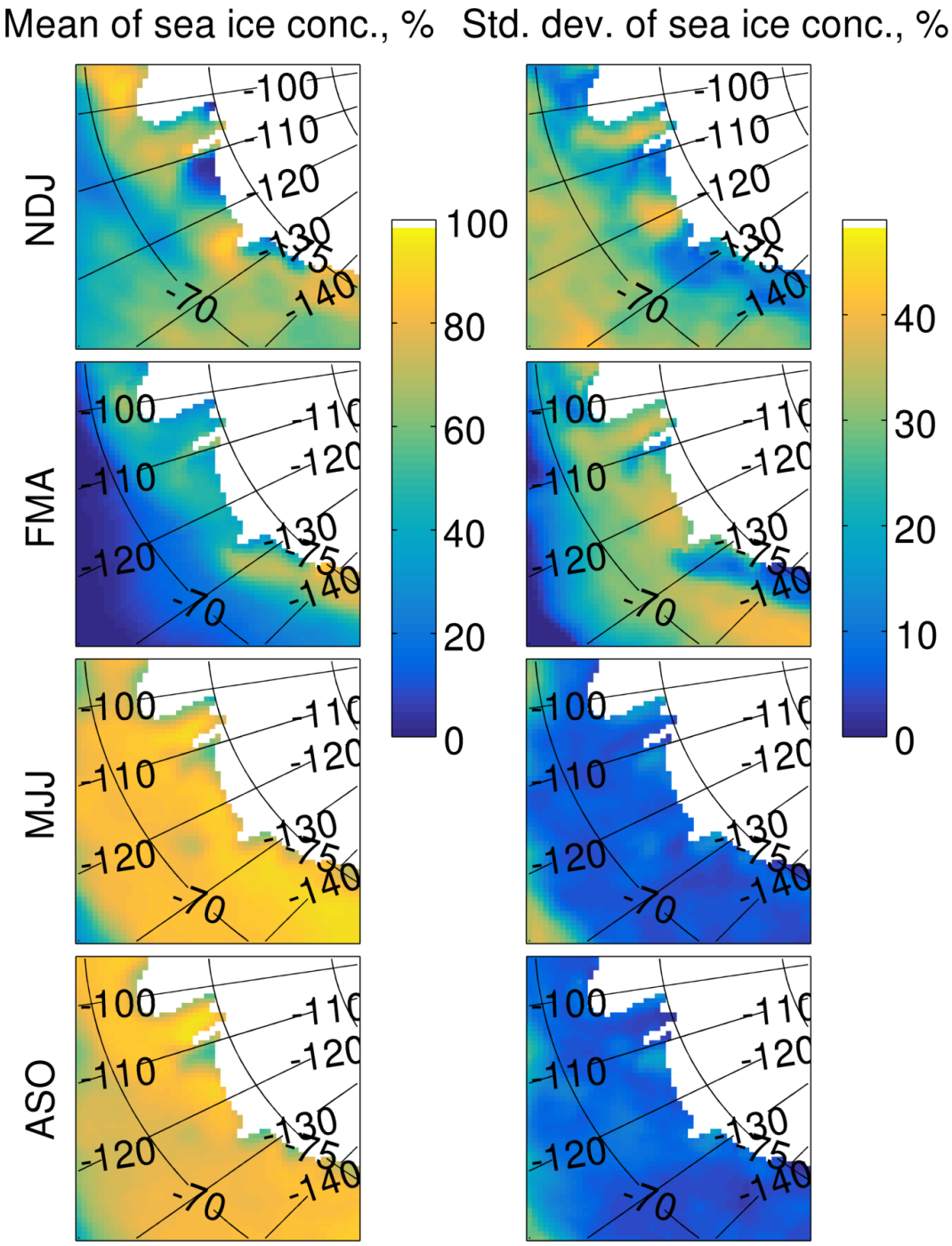

Figure 1.9: Mean (LHS) and standard deviation (RHS) of daily sea ice concentrations from 2014, for the four seasons (November-December-January, February-March-April, May-June-July, August-September-October) used in chapter 3. Data are Nimbus-7 SMMR and DMSP SSM/I-SSMIS Passive Microwave Data (Cavalieri et al., 1996).

1.6 Seasonal variation

Very little is known about the seasonal changes of water masses in the Amundsen sea, as data through the winter season come primarily from a sparse set of moorings. Models are being developed, and are beginning to show similarities to existing observational data.

1.6.1 Seasonal variation in inflow and heat transport

Arneborg *et al.* (2012) present mooring data from February to December 2010 with a transect across the trough in December 2008 and December 2010, for the western trough. They find inflow of warm salty water throughout the year, and overlying outflow of colder water. Barotropic velocity variations on tidal to seasonal time-scales are present but are small in comparison to the consistent southward baroclinic flow (Arneborg *et al.*, 2012). The data do not show strong seasonal variability in heat transport (Arneborg *et al.*, 2012). In the model run by Nakayama *et al.* (2017) seasonal variability at 552 m in the eastern trough is minimal, while at 222 m (above the depth of CDW) trough waters are ~ 0.5 °C warmer and ~ 0.5 saltier in January than July.

This lack of seasonal variability in CDW inflow is in contrast to the models run by Thoma *et al.* (2008) and Steig *et al.* (2012), who found seasonal changes in wind forcing altered inflow; where in late winter westerly winds over the outer shelf and slope force dense waters up onto the continental shelf. The Schodlok *et al.* (2012) model also finds seasonal variation in heat transport, with a peak in autumn.

1.6.2 Seasonal variation in warm layer thickness

Wåhlin *et al.* (2013) found that both bottom temperature and warm-layer thickness peaked in autumn (western trough), and that winds were not of primary importance to bottom temperature or warm-layer thickness, but they note that wintertime eastward winds were much weaker in 2010 and 2011 than the climatology. Kim *et al.* (2017) suggest that a summer peak in warm-layer thickness in the western trough is the result of wind and sea ice dynamics at the shelf break, where summer gaps in the sea ice between the shelf break

and the ice shelves allows wind driven upwelling, and a thicker CDW layer. The models of Thoma *et al.* (2008) and Steig *et al.* (2012), covering the Amundsen Sea Embayment, exhibited warm-layer thickness peaking in spring, as a result of eastward wind forcing.

1.6.3 Seasonal variation in upper ocean

The upper ocean has not previously been observed in winter - moorings can't extend to the surface where icebergs drift, and the winter weather conditions are too harsh for ship work. As such, very little is known about seasonal variation in the upper ocean. However, a seasonal cycle in salinity is expected, with autumn / winter salinification from the brine rejection of sea ice formation, and spring / summer freshening with ice melt. When and where the ocean is free of protective sea ice, the mixed layer depth is expected to deepen with wind driven mixing, and heat loss from the mixed layer to the atmosphere to increase. In summer, solar radiation and sea ice melt increase stratification. Webber *et al.* (2017) observe a strong annual cycle above the thermocline with their 5 year mooring, but the mooring top is deeper than 300 m, and so can only hint at what might be occurring above that depth. There are sparse atmospheric observations in winter too, limited to land-based automatic weather stations in a few locations. Jones *et al.* (2016) find, in the summer of 2014, using these weather stations, ship meteorological data and radiosondes, that reanalysis data over the Amundsen Sea provide a reasonable estimate, but fail to well represent wind variability near complex topography and high wind speeds, both of which will affect model representation of polynyas and upper ocean mixing, key components of the upper ocean seasonal cycle. They also find all four of the reanalysis examined had a cold bias, especially near coastlines (Jones *et al.*, 2016). As such model representations of surface heat fluxes is likely to be adversely affected. There are no atmospheric observations from winter over sea ice or open ocean, and so understanding of atmospheric seasonal cycle is limited.

1.7 Interannual variability

Even less is known about interannual variability of the Amundsen Sea water masses, as suitable data collection in the region began just two decades ago in 1994, not long enough or comprehensive enough to make firm judgements on interannual variability. Model estimates can be made, but cannot be confirmed until there are sufficient observational data. Schodlok *et al.* (2012) find in their model that variable strength of the PIB gyre leads to interannual variability in the basal melting of the Pine Island Ice Sheet (PIIS) of $\sim$ 22 - 32 m/yr between 1979 and 2010 (area-averaged). Historic satellite data can also be utilised. For example Mankoff *et al.* (2012) find evidence in PIB satellite imagery (Moderate Resolution Imaging Spectroradiometer (MODIS), Landsat, and Advanced Very High Resolution Radiometer (AVHRR)) of shifts between periods of open water or a single large polynya, and periods of smaller polynyas and more sea ice cover ($\sim$2000-2007). Webber *et al.* (2017) find, using 5 years of moorings on the continental shelf, considerable seasonal and interannual variability, including a cold period from October 2011 to May 2013 which dominated the timeseries, but through which a seasonal cycle was evident. A long term coordinated campaign of observational data collection must be executed, with consideration taken to achieve sufficient temporal and spatial coverage, for seasonal and interannual variability to be properly investigated.

1.8 PIG sub-ice-shelf cavity

In the 15 years between 1994 and 2009, melt rates of PIG increased $\sim$ 50%, while CDW temperatures in PIB increased by $\sim$ 0.1 to 0.2 °C between 2007/2009 and 1994/2000 (Jacobs *et al.*, 2011). Using Autosub, an Autonomous Underwater Vehicle (AUV), Jenkins *et al.* (2010) map and measure water properties inside the sub-ice cavity of PIG. They find a 300 m high submarine ridge splitting the cavity into an outer and inner portion, with the latter farther south at the grounding line (Figure 1.10). Using flow patterns in satellite imagery, they suggest that the glacier was previously grounded at this ridge in the early 1970s, and has since retreated $\sim$ 30 km into water 300 m deeper than at the ridge crest, where water column thickness is $\sim$ 250 m. As the melting increases the gap over the

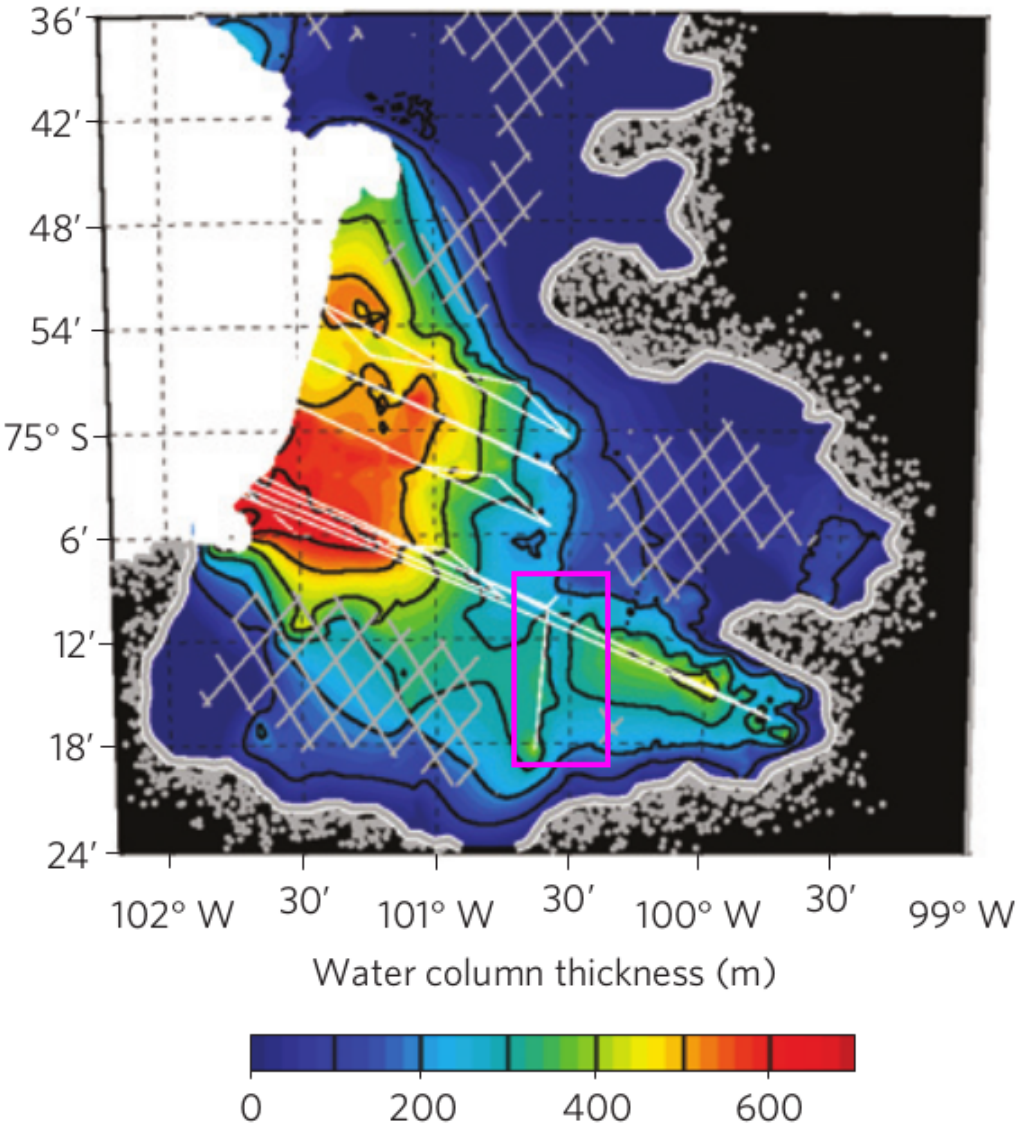

Figure 1.10: Water column thickness (difference between seabed depth and ice draft) of the sub-ice-shelf cavity beneath PIG. Thin white lines show Autosub tracks. Note shallow cavity ridge, marked with pink rectangle, vertical. Outer cavity to left of ridge, inner cavity to right. In data gaps (cross-hatched) interpolation was constrained to ensure the seabed is deeper than the ice draft as measured by radar. Adapted from Jenkins *et al.* (2010).

ridge, more warm water can enter the inner cavity and melt the ice shelf further (Jenkins *et al.*, 2010). This positive feedback loop may explain the ∼50% increase in melting (Jacobs *et al.*, 2011). Schodlok *et al.* (2012) find that while differing cavity bathymetries alter the mean melts calculated with their high resolution model, the temporal changes in those melt rates are similar between the simulations for the two bathymetries, suggesting temporal variability of melt rates is driven by processes external to the cavity. Greater knowledge of the shape, water properties and circulation of the sub ice-shelf cavity is

required to understand the mechanisms that determine melt rate and its sensitivity to external forcing, such as changes in heat transport triggered by changes in wind or sea ice (Jenkins *et al.*, 2010; Jacobs *et al.*, 2011). This in turn is essential for predicting the future meltwater input into the Amundsen Sea, and the changes that may follow.

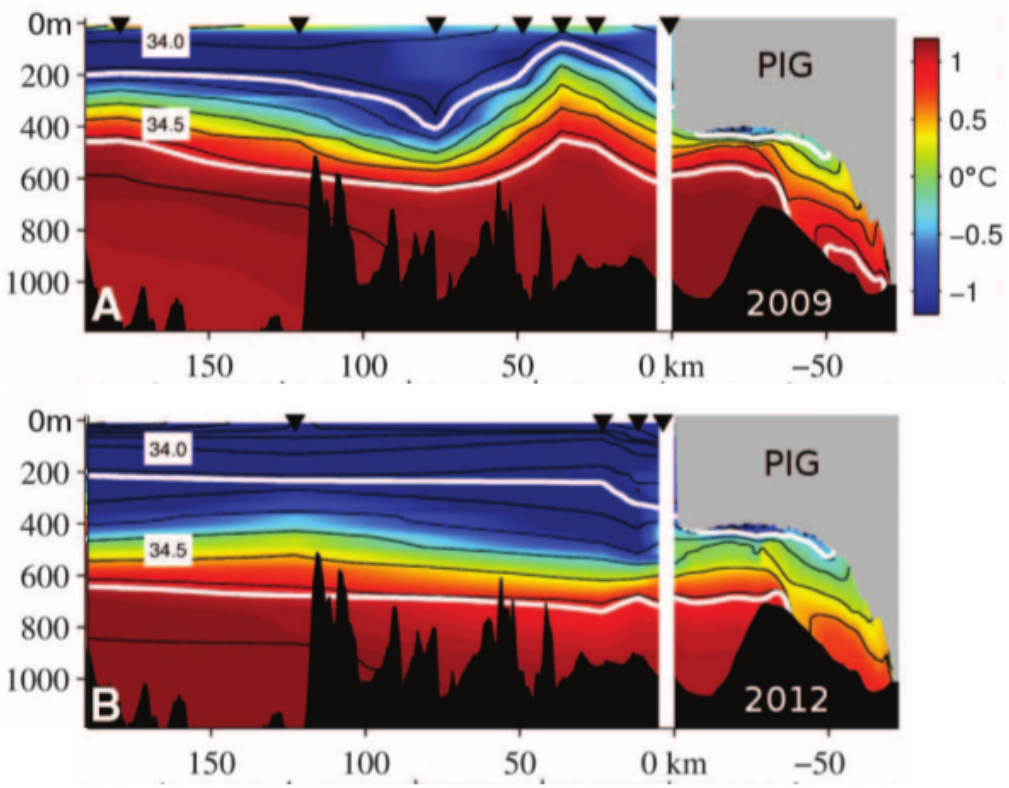

Figure 1.11: Observed and simulated potential temperature (colour) and salinity (white lines) in 2009 (top) and 2012 (bottom), along the eastern trough and into the PIG sub-ice-shelf cavity. Note that temperatures from $\sim$ 400 m depth, and not the seafloor, are those that are present beyond the sub-ice-shelf ridge, in the inner cavity and toward the grounding line. Adapted from Dutrieux *et al.* (2014).

1.9 Melt sensitivity, ice shelf and cavity

Dutrieux *et al.* (2014) use an ice cavity model to show that only the upper part of the CDW can overtop the –sub ice sheet– ridge to reach inner cavity and the grounding line (Figure 1.11), and suggest that this results in an 'enhanced sensitivity of ice-shelf melting to water temperatures at intermediate depth'. They use numerical modelling to provide an example of a lowered thermocline, matching that seen in 2012, reducing temperatures at the grounding line by 0.3 °C and resulting in a reduction in meltwater flux of 31 -

38%. Ice-shelf meltwater concentrations were reduced by 50 % between 2010 and 2012 (Dutrieux *et al.*, 2014). The conditions leading to the deeper 2012 thermocline are suggested to come from unusual regional atmospheric conditions decreasing the CDW inflow at the continental shelf edge (Dutrieux *et al.*, 2014).

There is no consensus on the key driver/s for melt variability.

1.10 So what don't we know about the water masses of the Amundsen Sea?

There are contradictory hypotheses for circulation of MCDW in the Amundsen Sea Shelf, for example Nakayama *et al.* (2013) propose southward inflow along the central trough, while Wåhlin *et al.* (2013) suggest northward flow in the central trough, away from PIG. Variability in this circulation is of course also unknown. Crucially, understanding the variability in the strength, location and even direction of the PIB gyre is essential for understanding heat delivery to the PIIS cavity.

The forcing mechanisms that enable the CDW to cross onto the shelf from open ocean are also unclear. Many mechanisms have been proposed, but there is little agreement on their importance, for example Wåhlin *et al.* (2013) found wind forcing did not have significant impact in inflow in the long term, while both Thoma *et al.* (2008); Steig *et al.* (2012) find wind forcing drives CDW inflow, but disagree on the season in which this is most pronounced.

There is a distinct lack of data in the winter months, despite some spatially sparse moorings. Data through the seasons, with good spatial coverage, and continuing in the long term would enable the study of seasonal and interannual variability. While satellites can provide some coverage, they cannot provide measurements at depth, or when cloud or ice cover obscures the sea surface, and as such can complement but not replace in situ oceanographic and atmospheric observational data.

Further investigation is required into the shape, water properties and circulation of and within the sub-ice shelf cavity of PIG in order to gain understanding of the mechanisms that drive melt rate, control melt rate sensitivity, and outflows from the cavity into the shelf sea. This will prove useful in making predictions of future behaviour of this and perhaps other ice shelves in response to climate change or other forcings.

1.11 Antarctic seals

Southern elephant seals (*Mirounga leonina*) are mesopelagic predators, spending over 80% of their lives at sea (Table 1.1), with most of that time between 300 and 400 m (McIntyre *et al.*, 2010). The average dive is 590 m, with maximum dive depths deeper than 2000 m (Roquet *et al.*, 2014). Dive duration is, on average, 25 minutes, up to a maximum of 120 minutes (Roquet *et al.*, 2014), surfacing for just a few minutes between dives. Females spend a greater percentage of their lives at sea, whilst males spend more time diving below 700 m than females (Table 1.1, McIntyre *et al.* (2010)). Weddel seals (*Leptonychotes weddellii*) dive much shallower, up to around 600 m, and for up to around 40 minutes. They stay near to the fast ice with a range of 50-100 km, and moult on the fast ice.

Table 1.1: Southern elephant seal diving characteristics.

	Females	**Males**	**Reference**
% of lives at sea	86.98	80.89	McIntyre et al., 2010
% of life below 100 m	68.92	65.54	McIntyre et al., 2010
% of life below 700m	1.84	8.98	McIntyre et al., 2010

Southern elephant seals come ashore twice a year to breed, in August to late November, and to moult, between January and March (Hindell *et al.*, 1991). Individual seals can travel thousands of kilometres to their foraging grounds. Foraging strategies vary between sex, breeding subpopulations (Biuw *et al.*, 2007) and individuals, with some seals targeting shelf or frontal systems, and others feeding in areas covered with sea-ice (Bailleul *et al.* 2010; Labrousse *et al.* 2015).

The seal tags and data used in this thesis will be introduced in depth in chapter 2.

1.12 This thesis

As mentioned in section 1.1, the goals of this thesis are to reveal spatial and seasonal variability of water masses in the Amundsen Sea, using seal tags, and to offer critique and suggestions for the improvement of those tags and the analysis of their data.

Chapter 2 provides in depth analysis of the tests of the tags against a standard ship CTD, finding substantial pressure-dependent errors in the tag calibration, and illustrating the necessity of such tests wherever possible. Chapter 2 thoroughly describes the multitude of corrections applied to the tag dataset (some resulting from the aforementioned tests) and describes the quality control measures applied to the dataset, outlining the measures necessary to bring a raw seal tag dataset up to a standard appropriate for addressing the relevant key research questions. Chapter 2 also makes some suggestions for the improvements to the tag algorithm for future tags deployed in the area, in order to best utilise the seal tag technology to answer the pressing research questions of the region, as outlined in here in chapter 1.

Chapter 3 presents a previously published paper (Mallett *et al.*, 2018), which uses the spatial coverage and abundance of the tag dataset corrected and quality controlled in chapter 2 to identify seasonal variation in the Circumpolar Deep Water in the eastern Amundsen Sea during 2014, addressing some of the most pressing research questions of the region. The chapter finds seasonal differences in CDW reversed from those found previously in the western Amundsen Sea, and that the seasonal differences seen in this dataset can be of opposite signs on scales as small as 20 km, but that coherent seasonal differences are observed over areas on the scale of 150 km.

In chapter 4, the dataset's unique upper ocean winter observations are utilised to examine the seasonal variation of the upper ocean, focusing on observations near the termini

of the glaciers of the Amundsen Sea, and providing invaluable descriptions of conditions and seasonality at these crucial glaciers through 2014. A combination of this dataset and concurrent moorings in Pine Island Bay are used to evaluate the extent to which conditions at the top of moorings can be used to estimate conditions above, in the event that only mooring observations are available. Surface conditions are poorly estimated by subsurface moorings, emphasising how crucial seal tag observations are in this and similar regions.

Conclusions are presented in chapter 5, along with recommendations for future work on these topics.

Chapter 2

Delayed Mode Quality Control and tag processing

2.1 This chapter

The following chapter will introduce the novel dataset utilised in this thesis, explain the data gaps it can fill, the value and caveats of this observation technique, and how it is collected and processed. The corrections and quality control measures necessary for this technique and this dataset in particular are presented in detail, including a justification for the necessity of pre-deployment tag tests, until technology improves. Recommendations are made for improvements to the tag compression algorithm necessary to obtain maximum value from those tags, specific to the addressed research questions.

2.2 Introduction to tags and the dataset

Seals have been tagged since the late 1980s (McConnell *et al.*, 1992), originally for purely biological research, and later as the technology developed, data were used for both biological and oceanographic research. The first tags to record full temperature and salinity profiles and relay them in near-real time were reported in the 2000s (Fedak, 2004; Boehme *et al.*, 2009). In Antarctica harsh weather and sea ice cover make oceanographic observation very challenging, almost impossible in winter, and seal tag observations have proved invaluable in filling this data gap (Costa *et al.*, 2008; Padman *et al.*, 2010; Roquet *et al.*, 2013; Kitade *et al.*, 2014; Herraiz-Borreguero *et al.*, 2015; Williams *et al.*, 2016;

Zhang *et al.*, 2016; Mallett *et al.*, 2018). In particular, the surface layer in winter is not measurable in any other way. The seals provide a broad spatial spread of a high number of observations, for little financial outlay relative to alternative methods. Around Antarctica to date there are at least 380,000 seal tag profiles (Roquet *et al.*, 2014, meop.net), around 70% of all profiles south of 60°S (Fedak, 2013).

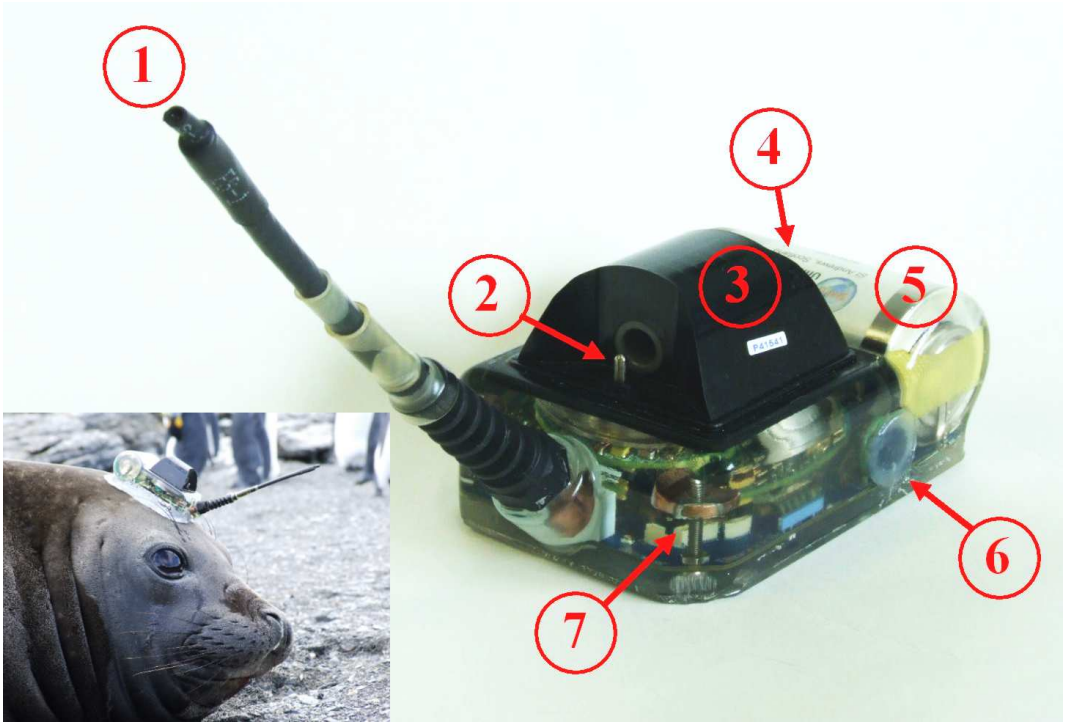

Figure 2.1: Figure from Boehme *et al.* (2009), caption: Picture of a CTD-Satellite Relay Data Logger (CTD-SRDL) with antenna (1), temperature probe (2), inductive cell (3), pressure sensor (not visible) (4), battery (5), communications port (6) and wet-dry sensor (7). Insert: CTD-SRDL deployed on a southern elephant seal.

Conductivity-Temperature Depth - Satellite Relayed Data Loggers (CTD-SRDL or 'tags', Boehme *et al.* (2009), figure 2.1) have been used in Antarctica for observing dense shelf water (Ohshima *et al.*, 2013; Kitade *et al.*, 2014; Williams *et al.*, 2016), upper ocean variability (Costa *et al.*, 2008), mapping bathymetry (Padman *et al.*, 2010), improving the state estimate of the Southern Ocean (Roquet *et al.*, 2013), and for observing CDW and meltwater on the continental shelf (Herraiz-Borreguero *et al.*, 2015; Zhang *et al.*, 2016). These last two water masses are considered crucial in the Amundsen Sea. Herraiz-Borreguero *et al.* (2015) use seal data to help reveal the circulation and distribution of mCDW in Prydz Bay, finding several modes of circulation beneath the Amery Ice Shelf, in one of which mCDW inflow results in formation of a fresher ice shelf water. Zhang

et al. (2016) use more than 20,000 tag profiles over 7 years to find mCDW on the Bellingshausen continental shelf flowing coastward in an eastern boundary current, mixing with meltwater at the coast, and then flowing back out to the shelf break in western boundary currents in troughs. In examining these water masses, seal tags are often not just the best observation method available, but the only suitable observation method available.

The tags are glued to the seals' fur on the back of the head (Figure 2.1, inset) with an epoxy resin, and within a year the seals moult and the tag falls off with the fur (in January-February) (Roquet *et al.*, 2011). The tags measure temperature, conductivity and pressure on the upward segment of a seal's dive, at a resolution of 0.5 s. The tags then use an algorithm to compress dives into 17 or 18 data points each, in order to optimise successful transmission of data via the Argos satellite-based system (Boehme *et al.*, 2009). The compressed dive data is then broken into 4 short 'messages' (256 bytes), one of which contains the temperature measurements, and another the salinity (calculated). These messages are each sent separately to the satellite, and sometimes one or more messages are not successfully received, so some profiles are missing temperature or salinity data.

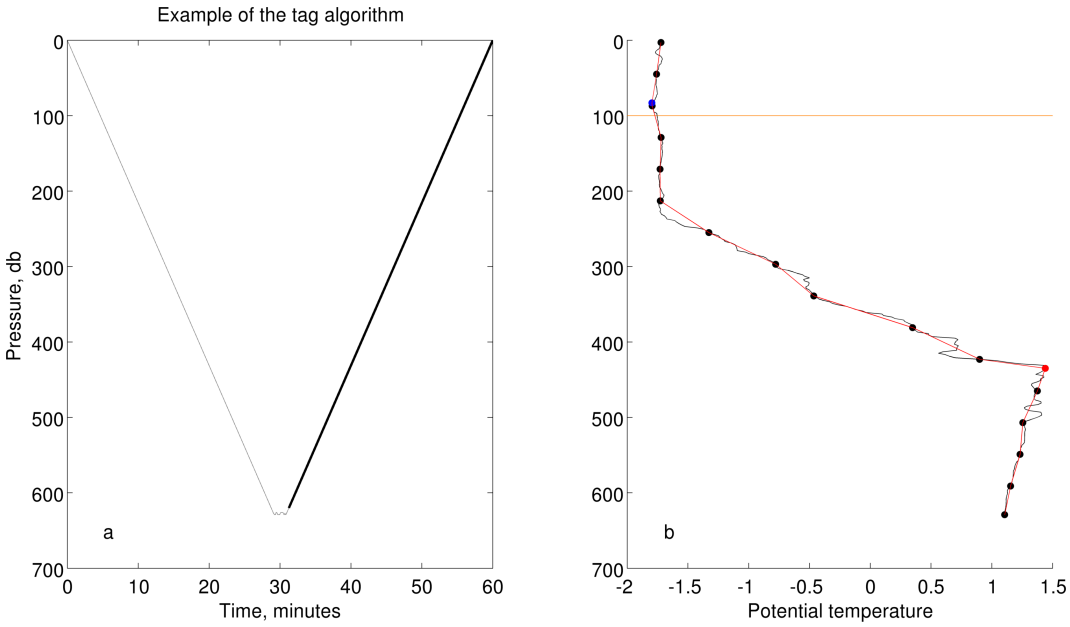

Figure 2.2: a) The (idealised) profile of a seal dive through time (grey), with the upcast segment of the dive used for data collection in thicker black. b) An example temperature profile (black line), with the same profile as represented by the tag algorithm (red). Black dots are points in the algorithm calculated from pressure the maximum, minimum, and 14 equally space pressure levels in between. The blue dot is the point at minimum temperature, and the red dot is the point at maximum temperature, below 100 db (orange horizontal line).

The standard algorithm used by tags reports the shallowest and deepest measurements, 8 fixed depths determined by the depth band of the deepest measurement, and 7 depths chosen by a broken stick algorithm which determines the most important inflection points (between the fixed depth levels) of the temperature, conductivity and salinity profiles, after some filtering and smoothing (Boehme *et al.*, 2009; Fedak *et al.*, 2002; Photopoulou *et al.*, 2015). One of the aims of the dataset presented here was to study the deep, warm CDW, and so the algorithm was adapted to make sure each profile reported this water mass, where encountered. The algorithm used here (Figure 2.2) picks out the temperature maximum deeper than 100 db, as well as the temperature minimum (any depth). The deepest and shallowest measurements are also used, and 14 pressure levels in between, equally spaced. When some of these points are the same - for example, the temperature maximum was at the deepest measurement - then the algorithm produces a profile with fewer depth levels - 17 rather than 18 data points. Only the deepest dive of every 4 hours is sent, to ensure the best possible dataset for the limited battery power (Boehme *et al.*, 2009; Fedak *et al.*, 2002; Fedak, 2004). Suggestions for how the algorithm could be improved for future deployments can be found in section 2.7.

In this thesis the data from 7 Weddell (*Leptonychotes weddelli*) and 7 Southern Elephant (*Mirounga leonina*) seals are presented. The Southern Elephant seals were tagged on 8th February 2014 at the Edwards Islands (73°52'S, 102°59'W), and the Weddell seals between 24th and 26th February 2014 on sea ice between 72°23'S, 108°46'W and 72°56'S, 11°19'W. Half of the tags were still transmitting in September 2014, with the last good quality measurements received on 1st December 2014. It was expected that the Weddell seals would do shallower dives and remain near the sea ice, while the Southern Elephant seals would roam farther and dive deeper. In reality, the foraging behaviour of the two species overlapped considerably, with some elephant seals remaining within the sea ice (M. Fedak, personal communication). However, generally female seals and Weddell seals did shallower dives, and Southern Elephant seals did deeper dives (Figure 2.4).

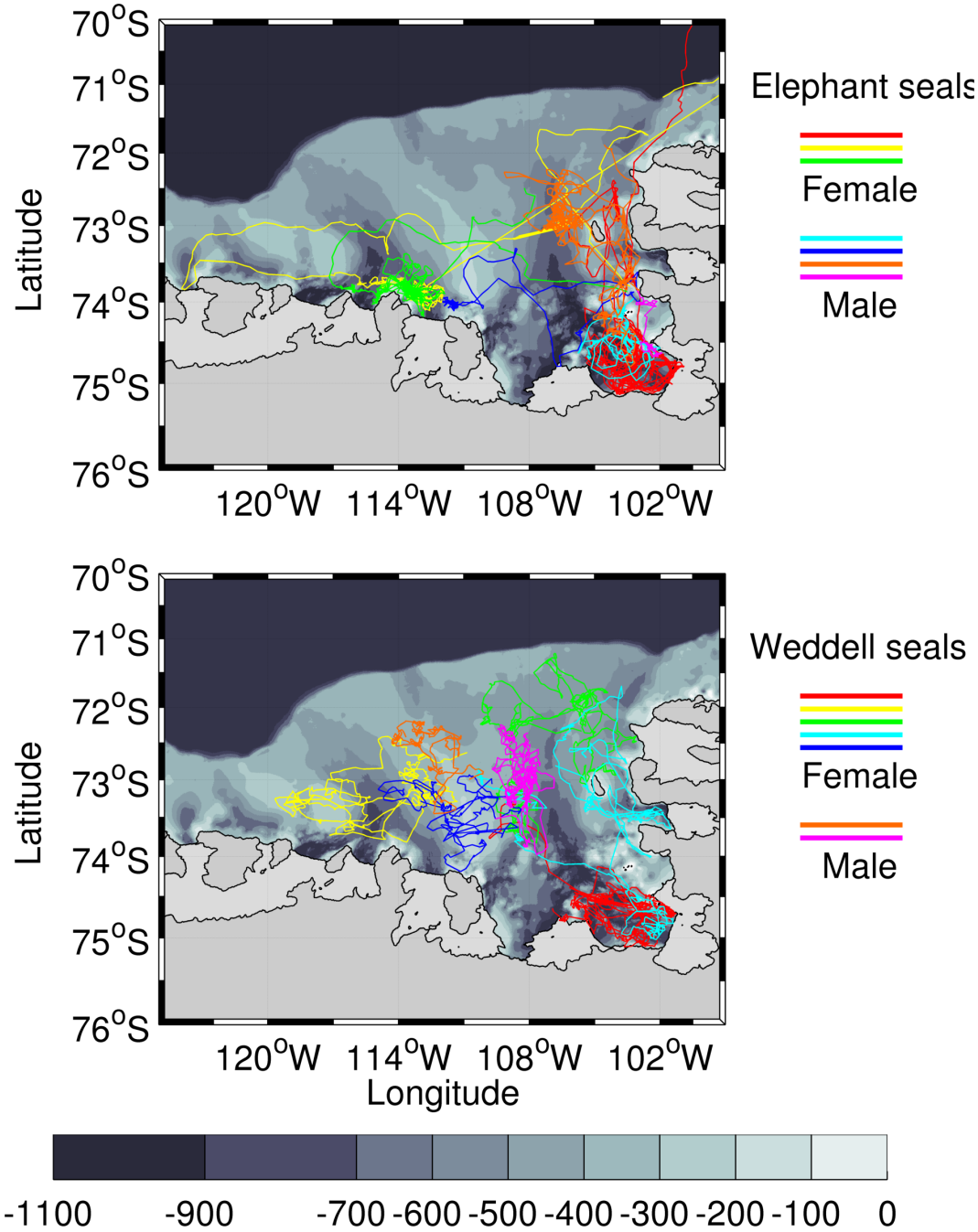

Figure 2.3: Top - tracks of the Southern Elephant seals. Red - tag number 838, yellow - 960, green - 970, cyan - 889, blue - 959, orange - 961, pink - 971. Bottom - tracks of the Weddell seals. Red - 858, yellow - 893, green - 895, cyan - 896, blue - 963, orange - 890, pink - 972. Greyscale is bathymetry, in m.

The data are received in near-real time, and Carse *et al.* (2015) showed that assimilating the temperature data from seal tags in near-real time improved the UK Met Office global ocean forecasting models root-mean-square error statistics by 1 to 6% in the Southern Ocean. Roquet *et al.* (2013) show that seal-tag data improve estimates of Southern Ocean general circulation, specifically estimates of sea-ice distribution. When using the

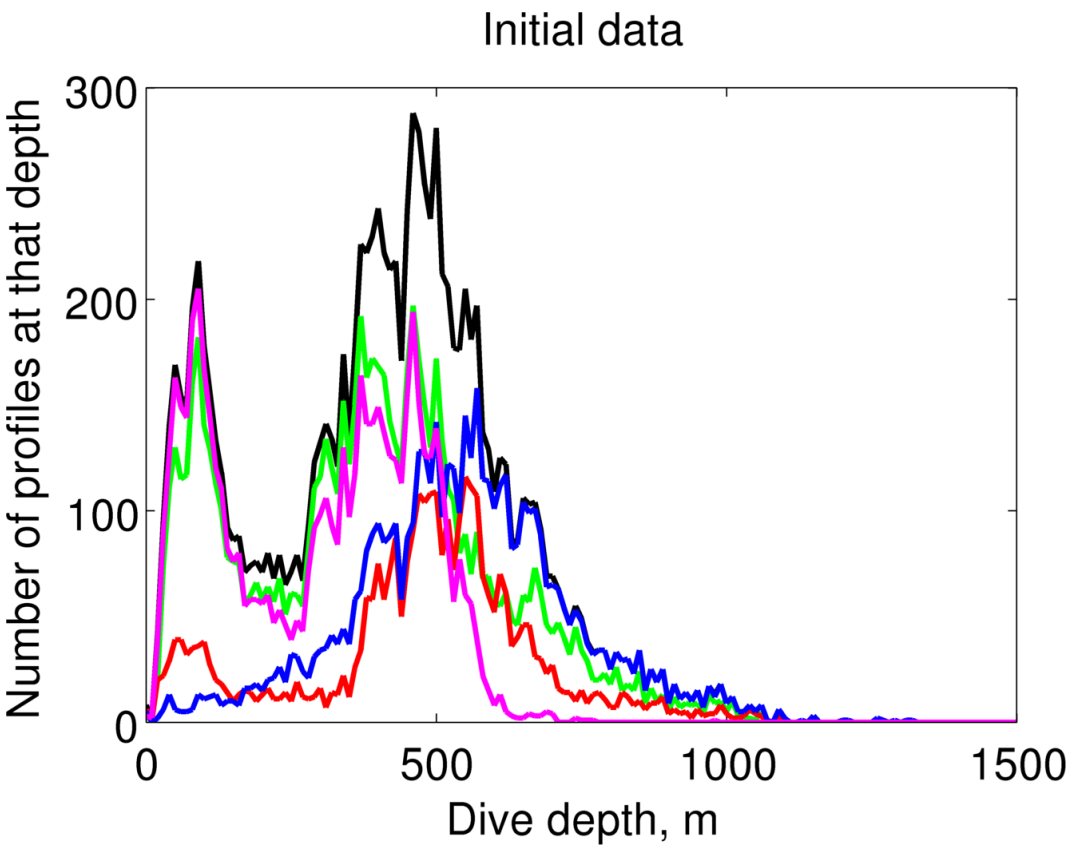

Figure 2.4: A histogram of dive depths, for the intial dataset before qc, for all seals (black), the 8 female seals (green), the 6 male seals (red), the 7 Southern Elephant seals (blue) and the 7 Weddell seals (pink).

data in near-real time for such purposes, it is essential that the quality of the data is as good as possible, and so continuing evaluation and improvement of tag technology, processing and quality control are essential.

Various corrections, processing and quality control techniques were applied to the data in order to maximise their value. Corrections were applied to the profile locations, derived using a Kalman smoother (Lopez *et al.*, 2015), and corrections to temperature and salinity were found from pre-deployment comparisons with ship-based CTD measurements. Profiles then underwent standard Delayed Mode Quality Control processing of the Marine Animals Exploring the Oceans Pole to Pole (MEOP) project (Roquet *et al.*, 2011, 2013, http://www.meop.net/). MEOP-processed data have an accuracy of +/-0.03° C for temperature and +/-0.05 for practical salinity (Roquet *et al.*, 2014). The accuracy of absolute salinity accuracy can be considered comparable. Further quality control was applied to this dataset. These corrections and quality control measures will be discussed

further in the rest of this chapter.

One of the main obstacles with seal tag data is that once the tag is glued to the head of the seal, the conductivity field is changed dramatically and an offset is introduced into the conductivity measurements (Boehme *et al.*, 2009; Roquet *et al.*, 2011). It is not possible to calibrate for this offset, since the tag is almost never retrieved after deployment, and so the 'head-effect' offset must be estimated by other means. If a seal dives near a mooring or a ship-CTD profile, then the head-effect offset can be found by comparison of stable water mass properties (Böhme and Send, 2005; Roquet *et al.*, 2011, 2013). If co-located measurements are not available, then comparison between tags can be used, where profiles from different tags are close in space and time. Comparison with a hydrographic atlas has also been used (Roquet *et al.*, 2009).

For many seal-tags datasets, the standard MEOP DMQC process (explained further in section 2.4) is all that is used. For the dataset presented here, additional pre-deployment tests were done, allowing for further analysis of the performance of the tags as compared with a Seabird CTD.

2.3 Pre-deployment tag tests on a ship CTD rosette

2.3.1 Tag testing procedure

Before deployment on the seals, each tag was attached to the ship's rosette for a CTD profile (Figure 2.5), so that for each tag there is a matching pair of profiles from both the ship CTD and the tag CTD. The ship CTD was equipped with two temperature sensors - SBE3plus with an initial accuracy of 0.001 °C, and two conductivity sensors - SBE 4C with an initial accuracy of $\sim$ 0.0003 S/m (Heywood *et al.*, 2014).

Here we present in detail the processing of a 'good' tag - 890, a male Weddell Seal tag which required less correction, and a 'bad' tag - 970, a female Elephant Seal tag which

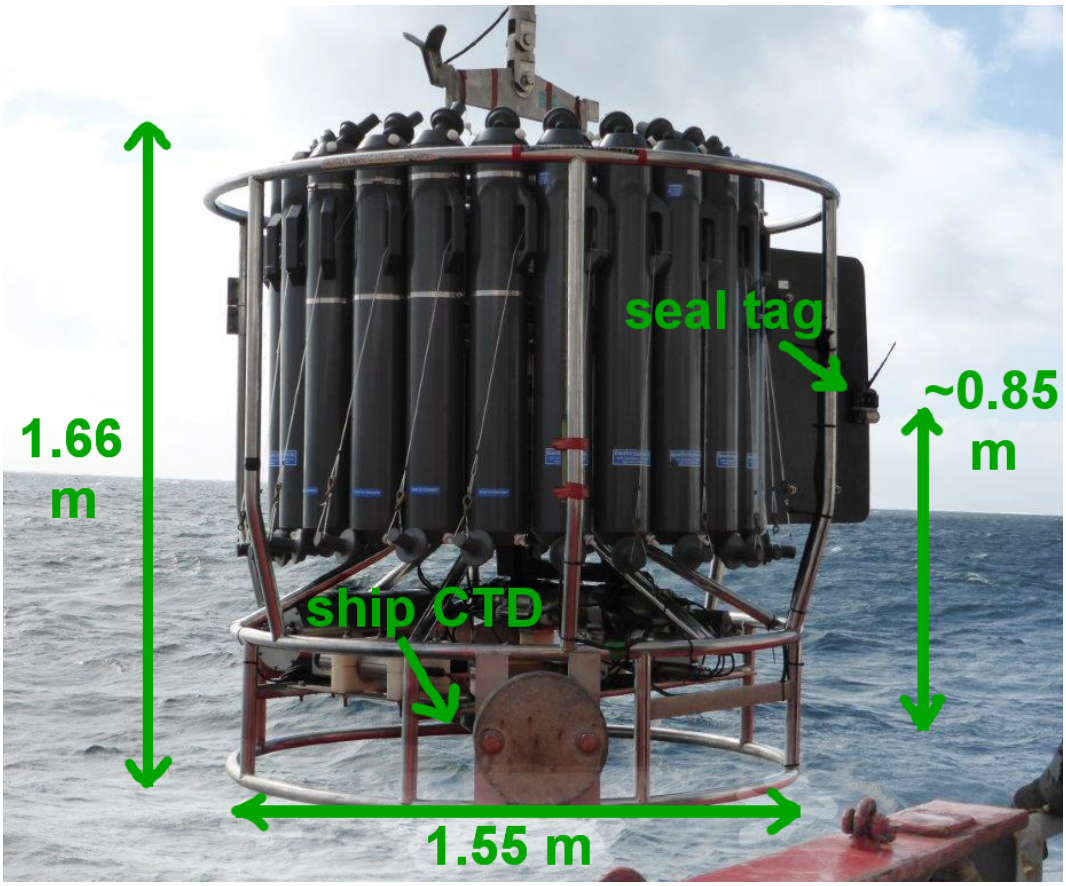

Figure 2.5: Annotated photo of the rosette with the ship CTD and seal tag marked, and approximate distances labelled. Photo courtesy of Mike Fedak.

required more correction. The corrections to the rest of the tags are provided in summary form. Two of the tags (962 and 892) which were tested against the ship CTD were not then deployed on seals, as a result of insufficient work time (Heywood *et al.*, 2014). Nevertheless, the results of these two tag tests against the ship CTD are presented here in summary form, as they still present a valuable opportunity to evaluate the tag sensors and their variability between tags. The missed opportunity of these two tags is regrettable, as seen in figure 2.3, many of the seals sample areas that others do not cover, and two seals can make a huge difference to coverage and number of profiles in a dataset of this size. It is recommended that careful consideration is made in future deployments regarding the value of tag data and the time taken to tag a seal, as compared with other observation methods (Heywood *et al.*, 2014).

2.3.2 Pressure offset

In the tag tests a pressure offset is present between seal tag and ship CTD, as a result of:

- an arbitrary constant added to the tag pressure sensor, which is normally removed by the tag compression algorithm, but which is not removed when the tags are in the mode used for the pre-deployment tests;
- the different height of the two sensors on the rosette (Figure 2.5);
- sensor error, or miscalibration.

It is necessary to first find corrections to the pressure sensor, before corrections to the temperature and conductivity sensors can be found. The pressure data from both the ship-CTD and the tag are first aligned in time (Figure 2.6). The pressure error is then calculated from the times when the ship rosette was stationary, as Niskin bottles were sampling, or at the bottom of the cast. Pressure errors calculated from times where the rosette was vertically moving would be subject to two different pressure sensor lags, as visible in the uncorrected error shown in figures 2.6a and 2.6b.

Aligning in time was attempted by a cross correlation, but because the data were at different temporal resolutions, and because the tag data sometimes starts part way into the dive, and the sampling rate sometimes takes a little while to get up to speed, the more efficient method was to align the two datasets by eye. In figure 2.6 the two example tags are displayed, with pressure differences plotted before (top) and after (bottom) the two profiles are aligned in time. It is clear that for some tags, pressure differences between tag and CTD vary with the depth of the rosette frame (figure 2.6c, pressure differences (blue wiggly line) vary with pressure (blue / red straight lines)). This is interesting in itself, but for the purposes of assessing the other tag sensors, a linear regression of pressure difference (between tag and ship CTD) with pressure is used to correct the seal tag pressure profile, for each tag where such a relationship is present. The tag for which pressure error varies most with pressure is 961 (Figure 2.7), with a pressure offset that varies by approximately 8 db between 1 and 1000 db. This is within the manufacturer's given pressure sensor accuracy of 1% of the full depth profile (10 db in 1000) (Roquet *et al.*, 2011). This level of error is not critical in the analysis of the seal tag data, given

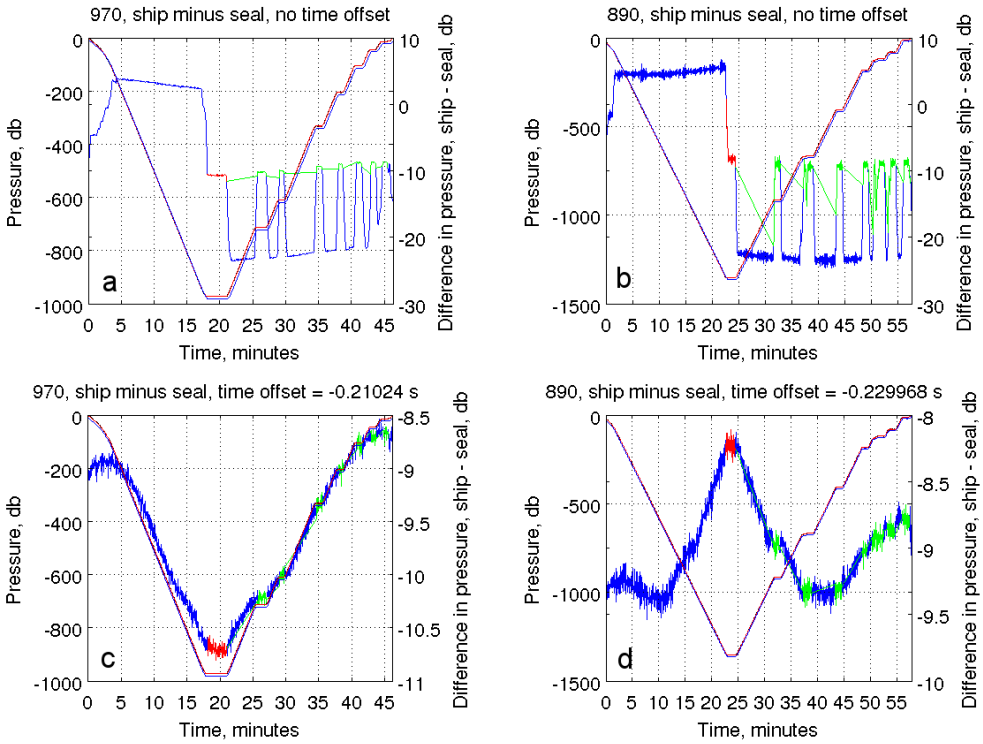

Figure 2.6: a) for tag 970, pressure plotted (left axis) for seal tag (blue), for ship CTD (black, concealed behind) and for ship CTD interpolated to match seal time (red), through time. Also plotted (right axis) is the difference in pressure at each time (blue), highlighted are the bottom of the cast (red) and the niskin bottle stops (green). c) tag 970, as in a), but with time offset applied. b,d) as a,c), but for tag 890.

the coarse vertical resolution of seal tag data over which interpolation and averaging must already take place in order to extract information. The pressure corrections are used in the subsequent calculation of temperature and salinity corrections. For tag 890, pressure offset varies with pressure, but not linearly, with the greatest pressure offset at mid depths (approximately 550 db) and the least at the surface (approximately 1 db less). The cause of this is unknown. For such tags, a single pressure correction is found (constant with pressure), from the mean pressure difference over all stopped locations. Tags for which linear pressure corrections are applied are marked with an X in the final column of table 2.1 (the rest have corrections constant with pressure).

The pressure sensor is a pressure transducer, where physical pressure deforms a flexible diaphram containing strain gauges which change electrical resistance with the deformation, producing an electrical signal in response to pressure change. It is beyond the scope of this thesis to investigate the cause of these pressure sensor errors which vary with

Table 2.1: Pressure corrections.

Species	Sex	Tag	Time offset, s	Mean pressure offset from bottom	Mean pressure offset from all stops	Gradient pressure offset, surface	Gradient pressure offset, 1000 db	Use gradient?
Elephant	F	838	-4.84	-5.125	-5.314	-5.323	-5.293	
Elephant	F	960	-17.46	-7.065	-7.111	-7.148	-7.050	
Elephant	F	970	-12.61	-10.696	-9.777	-8.615	-10.785	X
Elephant	M	889	-23.58	-3.701	-4.925	-5.892	-4.100	X
Elephant	M	959	-2.61	-7.851	-7.783	-7.634	-8.127	
Elephant	M	961	609.01	1.941	-0.737	-5.840	0.419	X
Elephant	M	971	-7.95	-8.619	-8.130	-7.757	-9.207	X
Weddell	F	858	-13.18	-8.799	-8.149	-7.712	-8.977	X
Weddell	F	893	-13.87	-9.062	-8.697	-8.314	-8.891	
Weddell	F	895	-12.23	-8.060	-8.292	-8.401	-8.150	
Weddell	F	896	-38.47	-8.519	-8.357	-8.152	-8.860	
Weddell	F	963	-18.01	-4.517	-5.117	-5.518	-4.281	X
Weddell	M	890	-13.80	-8.230	-8.912	-9.078	-8.738	
Weddell	M	972	-16.69	-8.964	-8.309	-7.514	-8.911	X
–	–	962	-16.32	-9.093	-9.045	-8.893	-9.283	
–	–	892	-7.72	-1.946	-3.885	-5.350	-2.572	X

pressure, although it is possible that temperature plays a role.

2.3.3 Temperature, Conductivity and Salinity corrections

Using the corrected pressure, the temperature, conductivity and salinity profiles of tag and ship CTDs are compared, for both upcast and downcast of the rosette. For these tests, the seal tags were in a test mode where both up and down casts were recorded, and so both can be compared with the ship CTDs. Many of the tag sensors display an error, compared with the ship CTD, that varies linearly with pressure (Figures 2.8g and 2.9c).

The tag errors calculated are more variable in the upper 600 m, where there are also more spikes in errors (i.e., Figure 2.8c,f,j). This boundary at $\sim$ 600 m corresponds with the top of the near-uniform CDW layer. In some cases there are depth ranges where the upcast and downcast diverge (ie figure 2.9c,j), likely due to an imperfect pressure offset between tag and CTD resulting in opposite lags seen between the upcast and downcast. In order to get the best temperature and salinity corrections possible, these unclear and

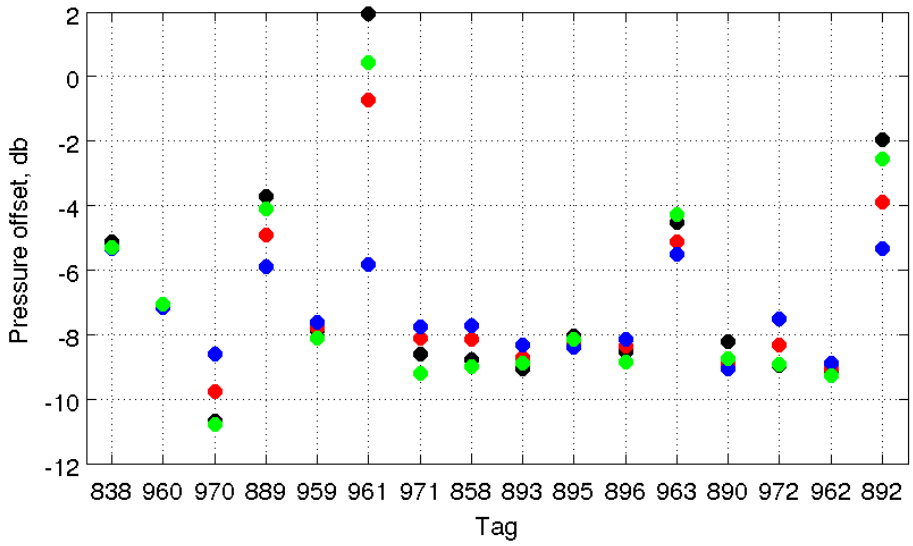

Figure 2.7: For each tag, mean pressure offset from the bottom of the cast (black), mean pressure offset from the bottom and stationary times when Niskin bottles were sampling (red). Using linear regression of pressure difference against pressure, for each tag, at all these stationary locations, calculated pressure offset at 1 db (blue) and at 1000 db (green).

more variable depth ranges are excluded from the calculation of the linear corrections, and the deeper, stabler depths dominate the calculations. Corrections are calculated from the upcast, since this is when the tag was correctly aligned with the direction of water flow (as it was fixed onto the CTD rosette, figure 2.5).

In tag 970 the salinity error is strongly dependent on pressure - it is approximately 0 at the surface, and approximately 0.2 at 1000 db, which is well beyond the MEOP database accuracy of +/- 0.05. The mean salinity RMS between the tags was 0.083 without these corrections, and 0.016 after corrections. 4 of the 16 tags tested had salinity sensors with an error more than 0.05 different at the surface than at 1000 db (Table 2.2, penultimate column, in bold). The mean temperature RMS between the tags was 0.032 without these corrections, and 0.015 after corrections. 6 of the 16 tags have temperature errors that are greater than the MEOP database accuracy of +/- 0.03 °C at some pressure, and 7 of them have errors that are greater than 0.03 °C different at the surface than at 1000 db (Table 2.2, 5th column, in bold). In reality, few tag measurements are as deep as 1000 db (Figure 2.4), so most resulting errors seen in the final database would be much smaller, but nonetheless these results suggest that the manufacturers' calibration process is unsatisfactory, and that reported sensor accuracies are not met. Discussions are ongoing between

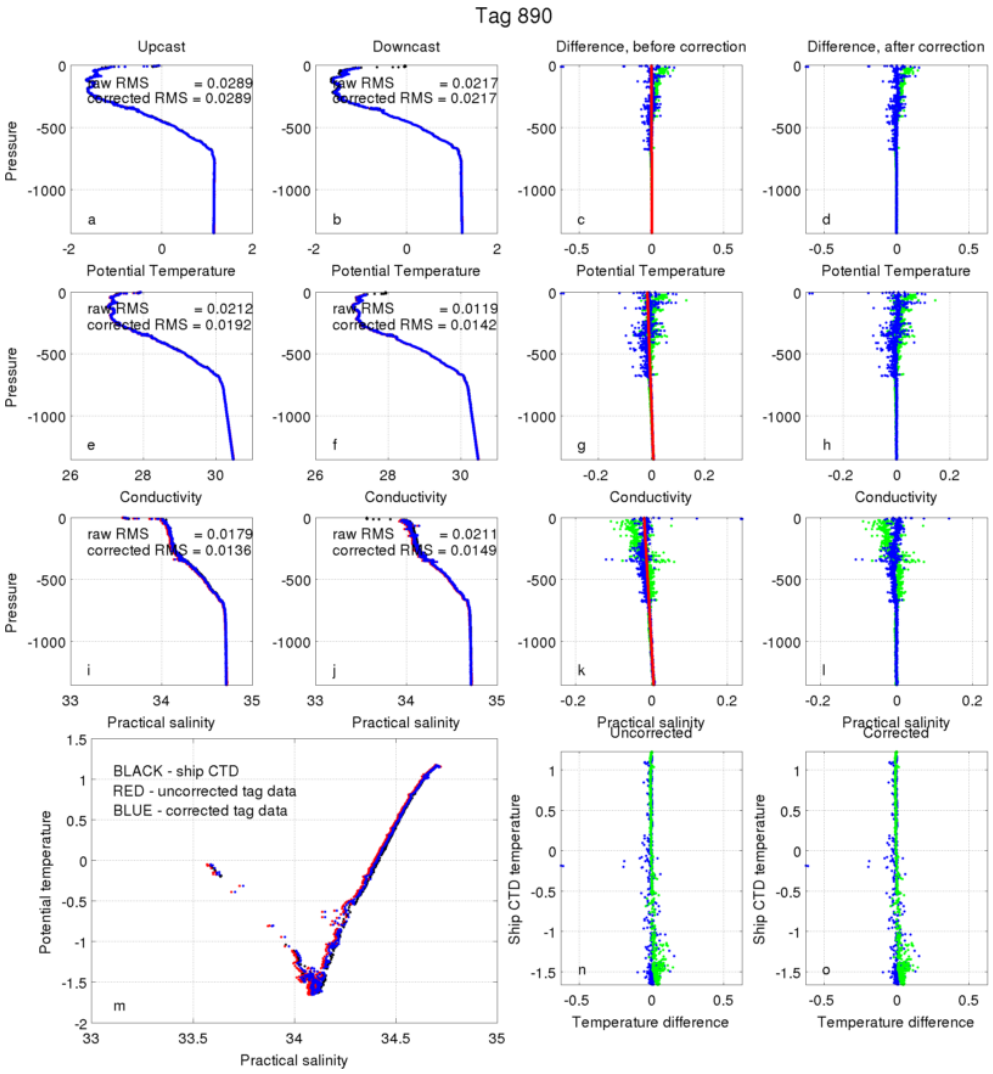

Figure 2.8: For tag 890, panel a - temperature of the upcast of the ship CTD (black, beneath), the uncorrected tag profile (red) and the corrected tag profile (blue). Labelled are the root mean squared error of the corrected and uncorrected tag profiles. Panel b - as in a, but for the downcast. Panel c - the difference between the uncorrected tag temperature and the ship CTD temperature, against pressure, for the upcast (blue) and the downcast (green). Overlaid (red) is the linear correction applied to the tag profile, found from the upcast. Panel d - as in c, but for the corrected tag profile. Panels e,f,g,h - as in a,b,c,d, but for conductivity. Panels i,j,k,l, as in a,b,c,d, but for salinity. Panel m - the ship CTD (black), uncorrected tag (red) and corrected tag (blue) profiles in temperature-salinity space. Panel n - the temperature difference between the uncorrected tag and ship CTD profiles, plotted against the ship CTD temperature, for the upcast (blue) and downcast (green). Panel o - as in n, but for the corrected tag profile (correction as found from a linear relationship with pressure, panel c, *not* a correction from a relationship between temperature error and temperature).

scientists at the Sea Mammal Research Unit and Valeport Ltd. (Totnes, United Kingdom), where the sensors are made. Until improvements to the sensors can be made, it is evident that these pre-deployment tag tests are essential for avoiding substantial errors in seal tag data, and should be considered a recommended part of deployment, wherever possible.

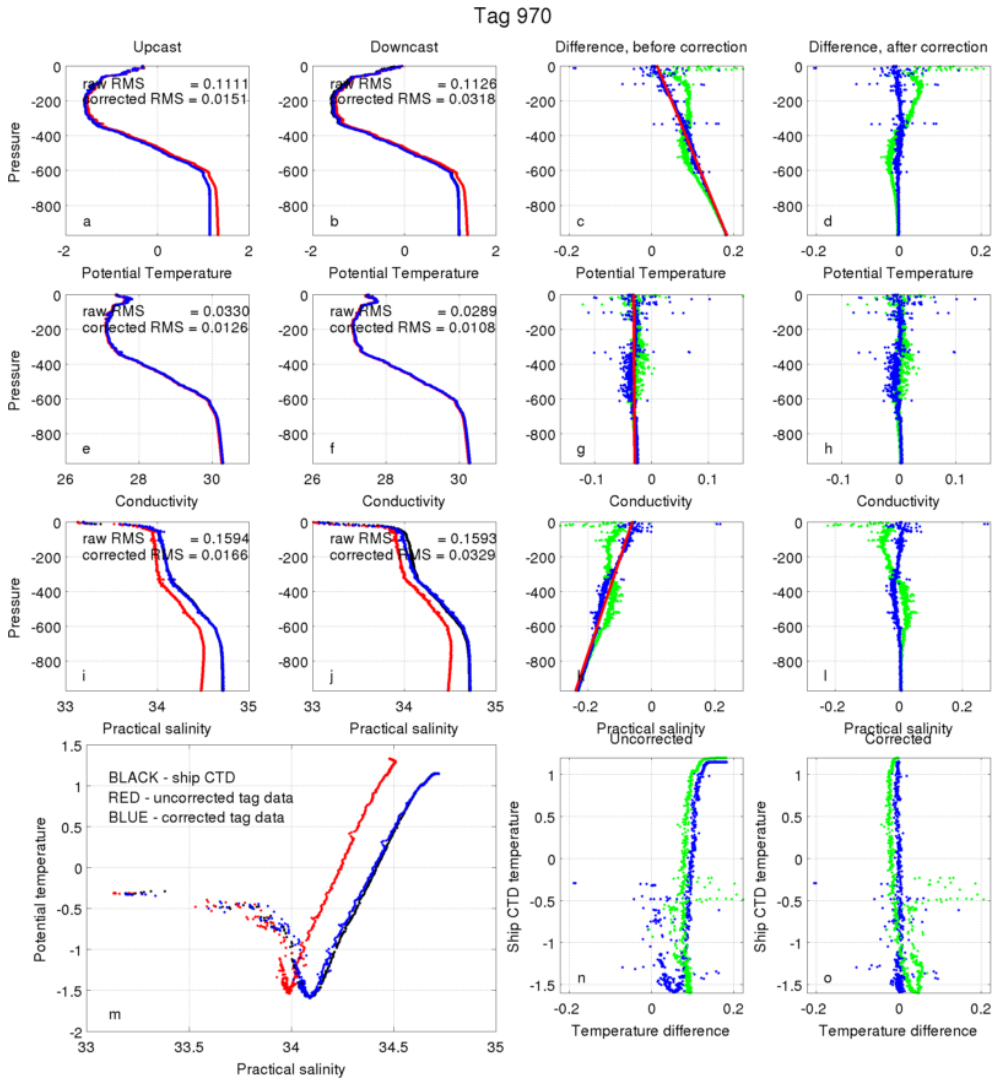

Figure 2.9: As in figure 2.8, but for tag 970.

The temperature sensor is a fast response platinum resistance temperature detector (PRT), where resistance through a fine platinum wire, which is dependent on temperature, is calibrated to calculate the temperature (Boehme *et al.*, 2010). The sensor range is from -5 to 35 °C, accuracy from 0.005°C (Roquet *et al.*, 2011). The above analysis does not find the sensors to perform to this specified accuracy, especially not at depth. It is not within the scope of this thesis to determine the cause of these sensor calibration errors, but it is possible that deformation of the sensor with pressure affects the resistance. The conductivity sensor is an inductive conductivity sensor. An electric current is applied by a coil, which induces a magnetic field in the vicinity of the sensor which is dependent on the conductive properties of whatever materials are close enough. This magnetic field then induces a current in a second coil, and the difference between these currents can be

Table 2.2: Temperature, conductivity and salinity corrections

Species	Sex	Tag	Temperature correction, intersect at 0 db	Temperature correction, gradient/db, *10^5	Conductivity correction, intersect at 0 db	Conductivity correction, gradient/db, *10^5	Salinity correction, intersect at 0 db	Salinity correction, gradient/db, *10^5	Actual salinity offset applied
Elephant	F	838	-0.0214	1.355	-0.0041	0.154	0.0189	-1.399	0.1
Elephant	F	960	0.0079	**-6.241**	0.0510	2.103	0.0644	**7.982**	0.08
Elephant	F	970	-0.0136	**-17.594**	0.0314	-0.181	0.0608	**18.388**	-0.1
Elephant	M	889	-0.0446	**6.615**	0.0072	-2.575	0.0591	**-10.643**	0.1
Elephant	M	959	-0.0091	0.522	-0.0113	0.161	-0.0055	-0.138	0.07
Elephant	M	961	0.0195	**-5.102**	-0.0018	-2.065	-0.0236	2.978	0.1
Elephant	M	971	-0.0209	2.517	0.1090	2.178	0.1784	-3.112	0.08
Weddell	F	858	-0.0004	**-5.155**	0.1210	-1.261	0.1592	3.497	0.1
Weddell	F	893	-0.0136	0.710	0.0805	-1.776	0.1164	-2.953	0.07
Weddell	F	895	-0.0088	1.251	0.0009	-0.384	0.0109	-1.918	0.1
Weddell	F	896	-0.0086	-1.711	0.0283	0.099	0.0504	1.282	0.1
Weddell	F	963	-0.0207	2.318	0.1134	2.126	0.1845	-2.536	0.1
Weddell	M	890	0.0003	-0.242	0.0154	-1.673	0.0192	-1.859	0.1
Weddell	M	972	0.0131	**-17.770**	0.0039	-1.285	-0.0083	**17.760**	0.0
–	–	962	-0.0290	**3.526**	0.0595	0.926	0.1179	-4.513	–
–	–	892	0.0042	0.723	-0.0078	-1.431	-0.0158	-2.475	–

calibrated to calculate the conductivity of the water. It is not clear how this sensor could be affected by pressure. The manufacturors report the accuracy of the conductivity sensor to be 0.01 mS/cm, for a range between 0 and 80 mS/cm. Salinity is calculated from temperature and conductivity measurements, and temperature errors dominate the errors calculated for salinity, not conductivity errors (figure 2.9a,e,i).

In the final seal tag database these corrections are applied, except for the salinity offset, which as mentioned previously is affected by deployment on the seal, and must be

recalculated afterwards. The salinity offsets actually applied are derived from the standard MEOP processing (section 2.4), and are listed in the final column of table 2.2.

Roquet *et al.* (2011) performed similar tests on 12 tags in 2006, in the Mediterranean Sea. For the worst tag, they found a linear effect with pressure on the temperature sensor of 0.053 °C over 1000 db ('dives' were to 400 m), with a mean between the tags of 0.023 °C. The largest found from the tags presented here is 0.178, with a mean between the tags of 0.046. The biggest salinity correction with pressure found by Roquet *et al.* (2011) was 0.050 over 1000 db, with a mean between the tags of 0.021. The largest found from the tags presented here is 0.184. Roquet *et al.* (2011) conducted multiple test dives for each tag, and found these linear errors with pressure to be consistent between dives (standard error less than 0.005). The set of tags presented here performs considerably worse than those presented by Roquet *et al.* (2011). Two tags (970 and 972) have much larger errors with pressure, and with these removed the mean between tags for gradient of temperature error with pressure is reduced to 0.027, much closer to the equivalent mean found by Roquet *et al.* (2011, 0.023). However, both sample sizes (12 and 16) are small, and it is likely that these two worse tags are not unusual.

Error in the temperature sensor that varies with temperature (Figures 2.8n,o and 2.9n,o), is present in some tags for the uncorrected data, and since temperature varies similarly to pressure in this location - both increasing with depth - it is possible to confuse which is responsible. For most tags presented here temperature error varies more linearly with pressure than with temperature, if there is a variable error present (ie. Figure 2.9c,n). For all tags, once corrections for temperature error varying with pressure have been made, there is no longer a substantial linear relationship between temperature error and temperature (Figure 2.9o). As such, it is concluded that any temperature errors with temperature are secondary to those with pressure, and are unsubstantial.

2.4 MEOP DMQC

The MEOP consortium has proved invaluable in providing a quality controlled database of tag data from marine mammals, and providing easy access to these data (Treasure *et al.*, 2017). The standard MEOP post-processing procedure includes (Roquet *et al.*, 2011):

- where pre-deployment tag tests against a ship CTD are available, calibrate pressure effects;
- calibrate the salinity offset ('head effect') using delayed-mode methods;
  - comparing tag salinity measurements to historical Argo or CTD data, where available, using stable water mass properties;
  - comparing salinity measurements between tags, finding a least squares minimum of the differences between instruments;
- edit and filter out erroneous temperature and salinity profiles;

Since the processing by MEOP of the dataset presented here, two additional procedures have been added to this list. The first corrects for errors introduced by the thermal mass of the tags themselves (Mensah *et al.*, 2018). The second removes density inversion by adjusting the salinity profile (Barker and McDougall, 2017).

After this delayed-mode processing, the dataset is considered to have a precision of approximately 0.01 °C and 0.01, and an accuracy better than 0.03 °C and 0.05 (Roquet *et al.*, 2011). The results of the pre-deployment tag tests presented in section 2.3.3 suggest that datasets without pre-deployment testing are liable to have some tags with greater errors which are variable with depth.

The delayed-mode processing work is done by Fabien Roquet of MEOP, not the author, and the results are presented here in summary form, in order to present full information. In table 2.3 are the number of temperature and salinty profiles for each tag, before and after MEOP quality control. Evident is the variability between tags - some fall off the seal much quicker than others (971 - 26 days) and produce fewer data (101 profiles with both temperature and salinity, and passing quality control), and some lose

so many profiles to quality control that much of the seals' hard work is unusable (960, losing 36% of temperature profiles and 39% of salinity profiles to quality control). It is also evident that salinity profiles are more successfully communicated by the tag to the satellite (10966 salinity profiles received, for 9616 temperature profiles). It is unclear why this might be. The temperature profiles are sent in the 2nd message to the satellite, and the salinity in the 3rd message, so while it could be expected that fewer salinity profiles would be received (when seals dived before transmission was completed), it is unexpected that fewer temperature profiles would be received.

Some seals are more prolific (889, table 2.3), collecting more good profiles per day (5.45) than others, a result of tag duration, performance and seal industriousness. Elephant seals generally collected more good profiles per day (4.15, 4.56 without tag 960) than Weddell seals (3.70). Female seals collected more profiles per seal (on average, 902 - Elephant, 768 - Weddell) than the males (Elephant - 464, Weddell - 608), but the tags stayed on the female seals for longer. Per day, on average, female seals collected 3.64 (Elephant & Weddell) profiles, while the males collected 5.0 (Elephant) / 4.5 (Weddell). Without knowing if there is a cause for the tags remaining on females longer, it is not possible to judge which sex is more productive to tag. It is not just volume of data that is important, but spatial distribution. Weddell Seals tend to spread their observations more, while Elephant Seals more often repeatedly dived in one area (Figure 2.3), although there is crossover between species in this behaviour. A balance between a good spatial spread of data, and areas with repeat observations (enabling comparison between seasons), is ideal. As such, tagging both species is recommended for future deployments.

Table 2.3: Number of profiles per seal, before and after quality control

Species	Sex	Tag	no. days data	no. T profiles, before MEOP qc	no. T profiles removed by MEOP qc	no. T profiles, after MEOP qc	no. S profiles, before MEOP qc	no. S profiles removed by MEOP qc	no. S profiles, after MEOP qc	no. of profiles with both T and S, after MEOP qc	mean no. of profiles with both T and S, after MEOP qc, per day
Elephant	F	838	244	927	0	927	1201	1	1200	860	3.52
Elephant	F	960	291	794	284	510	884	341	543	489	1.68
Elephant	F	970	209	986	2	984	1154	24	1130	947	4.53
Elephant	M	889	60	332	1	331	344	2	342	327	5.45
Elephant	M	959	73	390	5	385	424	6	418	379	5.19
Elephant	M	961	210	1030	0	1030	1128	6	1122	1007	4.80
Elephant	M	971	26	103	0	103	113	0	113	101	3.88
Weddell	F	858	195	802	7	795	846	23	823	772	3.96
Weddell	F	893	195	697	0	697	826	10	816	643	3.30
Weddell	F	895	203	855	0	855	961	5	956	823	4.05
Weddell	F	896	221	818	2	816	966	6	960	764	3.46
Weddell	F	963	244	666	1	665	839	2	837	599	2.45
Weddell	M	890	87	375	1	374	403	3	400	370	4.25
Weddell	M	972	183	841	0	841	877	13	864	815	4.45
Totals	–	–	2441	9616	303	9313	10966	442	10524	8896	3.64

2.5 Location reprocessing

The locations of profiles are found using the Argos satellite system. When a tag communicates with a satellite, the Doppler shift in the carrier frequency of the message is used to estimate distance. Profile locations are then estimated from these communication locations, using the time difference between message communication and time of dive.

The first method used by Argos to do this was a nonlinear least squares estimation. The estimation required 2 messages per satellite pass to estimate a location of the tag. 4 messages per pass were required to estimate error for this location. The more messages per pass, the better the location (Lopez *et al.*, 2014). Errors ranged from tens of kilometres for 2 or 3 messages received, down to 250 m and better, where more high quality messages were received per pass (Lopez *et al.*, 2014). For datasets such as that presented here, the number of messages is often fewer than ideal, as the seals can dive before all messages are successfully communicated, poor weather conditions can impede message communication, and there are fewer satellites available at the poles than at other locations. As such, these locations are considered low accuracy (Roquet *et al.*, 2011).

An alternative, location processing introduced in 2011 offers improvements to the quality of the locations (Lopez *et al.*, 2014, 2015). This processing system uses an Interacting Multiple Model (IMM) filter (a Kalman filter), where likelihood based filtering of realistic prior and present locations and a realistic movement model are used to estimate locations and their errors, offering greatly improved location estimates in real time (Lopez *et al.*, 2014). This algorithm is able to estimate location and location error for satellite passes where just one message was received, unlike the least-squares method used previously (Lopez *et al.*, 2014). Thus, in datasets where message communication is less successful, the new algorithm provided many more locations. In data from elephant seals, this can double the number of locations provided (Lopez *et al.*, 2014), reducing the mean error from approximately 14 to 5 km where 2 or 3 messages were received (Lopez *et al.*, 2014).

More recently, a third location processing system was made available, a smoothed Kalman filter. Here a forward-time Kalman filter is used with the addition of a backward filter, using both prior, present and subsequent locations to improve the locations of the whole dataset (Lopez *et al.*, 2015). This method cannot be applied in real time, since it utilises subsequent (future) locations, but when applied after the complete collection of the dataset, offers improvements of 20% to the error of locations estimates from Elephant

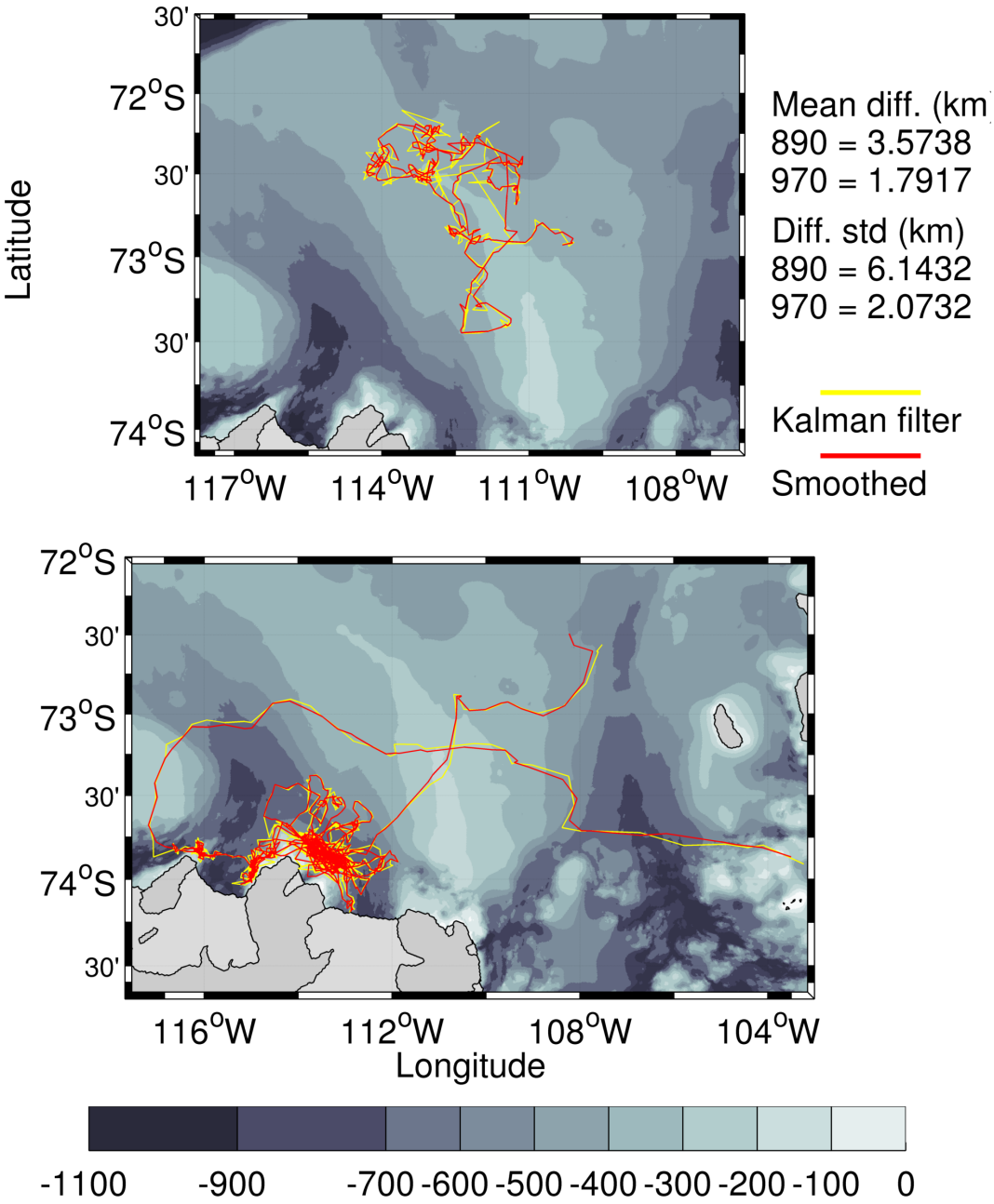

Figure 2.10: Top - locations using Kalman filter (yellow) and using smoothed Kalman filter (red) for tag 890. Bottom, as above, but for tag 970.

seal tags when 4 or more messages are received per satellite pass, and a reduction of 25% in the standard deviation of those errors (Lopez *et al.*, 2015). Where 1 message is received, mean error is cut by more than half for data from elephant seals (Lopez *et al.*, 2015). This service was provided by Collecte Localisation Satellites (CLS), and applied to the dataset presented here.

The locations provided by the best available processing; the smoothed Kalman filter,

Table 2.4: Location corrections

Species	Sex	Tag	Median difference in location (km)	Mean difference in location (km)	Standard deviation in location difference (km)
Elephant	F	838	2.03	3.34	4.06
Elephant	F	960	1.34	2.46	3.99
Elephant	F	970	1.13	1.79	2.07
Elephant	M	889	1.67	2.84	3.04
Elephant	M	959	1.81	2.98	3.74
Elephant	M	961	1.21	2.28	3.06
Elephant	M	971	1.06	1.83	3.00
Weddell	F	858	1.14	1.82	1.99
Weddell	F	893	1.59	3.55	5.35
Weddell	F	895	1.36	2.55	3.63
Weddell	F	896	1.57	3.90	7.30
Weddell	F	963	1.28	4.29	10.00
Weddell	M	890	1.58	3.58	6.15
Weddell	M	972	1.47	2.91	4.77

are compared with the locations as found by the real-time Kalman filter for tags 890 and 970 in figure 2.10. The mean distance between the two locations, and standard deviations of these are listed for each tag in table 2.4. For most profiles, and most tags, distances between locations found by the two methods are less than 5 km (Table 2.4), but for some tags (896, 963) there are multiple locations in the seal track where there are large divergences between the tracks provided by the two locations, up to 90 km. Generally the tags on Weddell seals have more of these, perhaps a result of the conditions where the seals are foraging, or their surfacing time. Even when considering only the smaller distance corrections, the Rossby radius in the region is < 5 km, so water masses can be different at these scales. The analysis presented in later chapters grids profiles into cells on the order

of 10 x 10 km. Some of these cells might have less than 5 profiles in, so one misplaced profile can have an adverse effect on conclusions. As such, it is recommended that these location improvements are taken advantage of where possible.

2.6 Further quality control work

Further to the MEOP quality control, additional measures were applied. Criteria for flagging a profile include:

- the profile contains unfeasible values for temperature, salinity or calculated potential density;
- the profile is unstable, beyond a threshold;
- the profile contains supercooled water, to a degree which is unfeasible.

The criteria / thresholds for what is deemed unfeasible are guided by historical data in the area. Walker *et al.* (2013) found, in 2003, potential temperatures onshelf between -1.8 and 1.75 °C and not supercooled, and practical salinities up to 34.76 psu and fresher than 33 psu (figure 1.2). Wåhlin *et al.* (2013) found potential temperatures up to 1.4 °C, and practical salinities up to 34.72 (figure 1.3). Conservative temperature and potential temperature are similar enough to be considered equivalent for this purpose (the maximum difference between the two in the seal tag dataset is 0.0075°C). Practical salinity is ~ 0.2 less than than absolute salinity (in the seal tag dataset, absolute salinity is greater than practical salinity by between 0.15 and 0.17, with a mean of 0.17). It is clear from the different boundaries to observed temperature and salinity in different years in the literature, that at different times (and in different places) the properties of water masses vary. Thus the thresholds for unfeasible properties in the seal tag dataset are also guided by comparison with the seal tag dataset as a whole. This is particularly important considering much of the historical data is from summer, and much of the seal tag data is from winter, and so are not directly comparable. The 2014 moorings are also used to inform these decisions, since they provide observations from the same summer and winter seasons as the seal tag data, but with the caveat that these observations are confined to PIB and the shelf break, and are not representative of the whole shelf, and do not extend to the surface.

Seals can sample very close to sea ice and icebergs, so low salinities are expected from meltwater, but several profiles include such low salinites that they are as likely to be erroneous readings of the conductivity sensor as observations of meltwater (blue, figure

2.11). A threshold of 32.7 absolute salinity is used, which is fresher than historically reported measurements by a margin of more than the tag salinity sensor accuracy (0.05), to avoid flagging unnecessarily. 11 such profiles are flagged as fresher than this threshold.

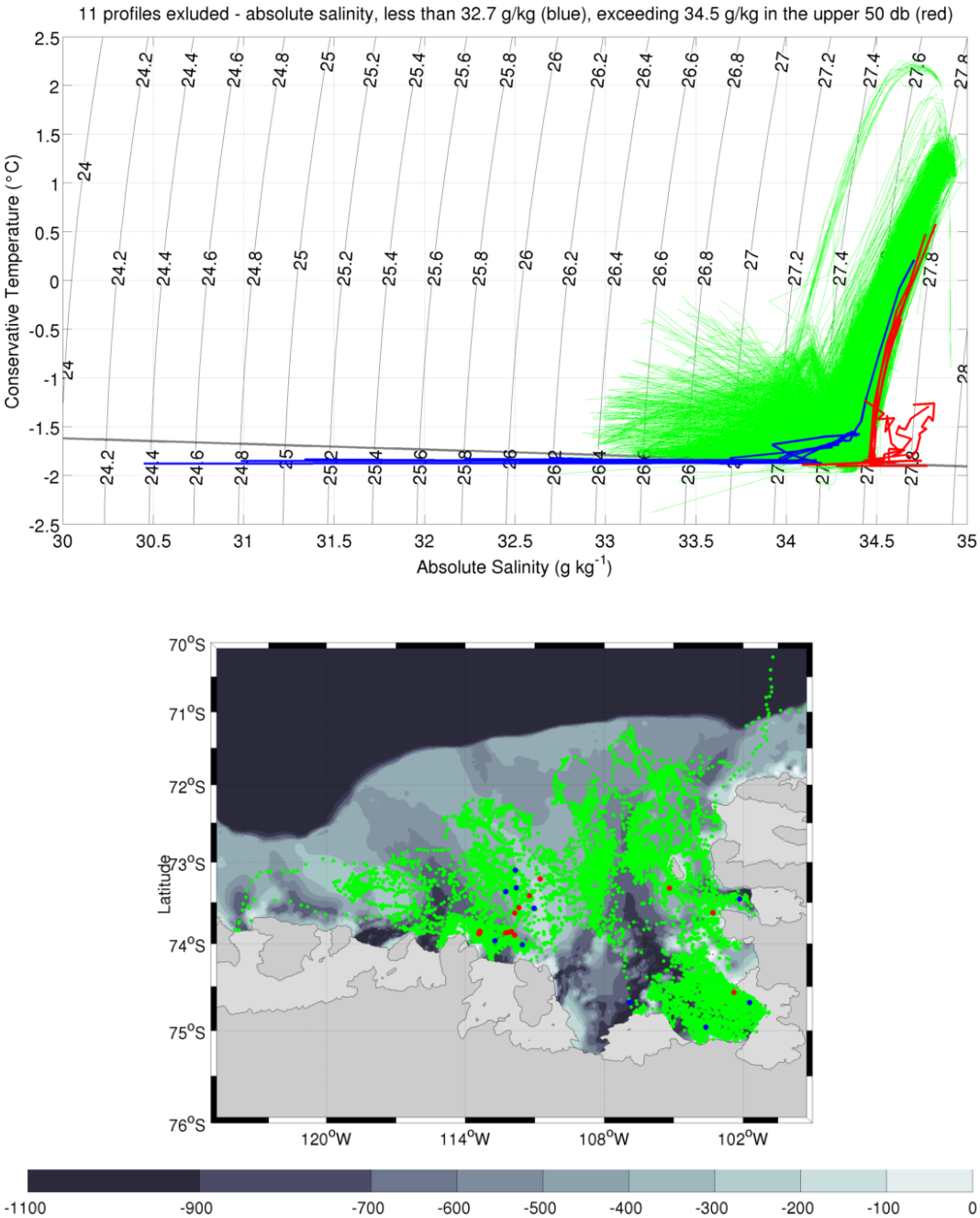

Figure 2.11: Top - Absolute salinity and conservative temperature for all profiles (green) and for profiles excluded as absolute salinity is less than 32.7 g/kg at some depth (blue), and for profiles excluded as absolute salinity exceeds 34.5 g/kg in the upper 50 db (red). The thick black line is the freezing line. Bottom - locations of these profiles.

While high salinity is expected near the surface - the result of brine rejection as sea ice forms - there are some profiles with salinities so high they are unrealistic, and these profiles also exhibit obvious anomalous behaviour in TS space (red, figure 2.11). A threshold of 34.5 is used, less than the salinities observed in literature, since here only the surface 50 db is considered (deeper observations are saltier). 15 such profiles are flagged.

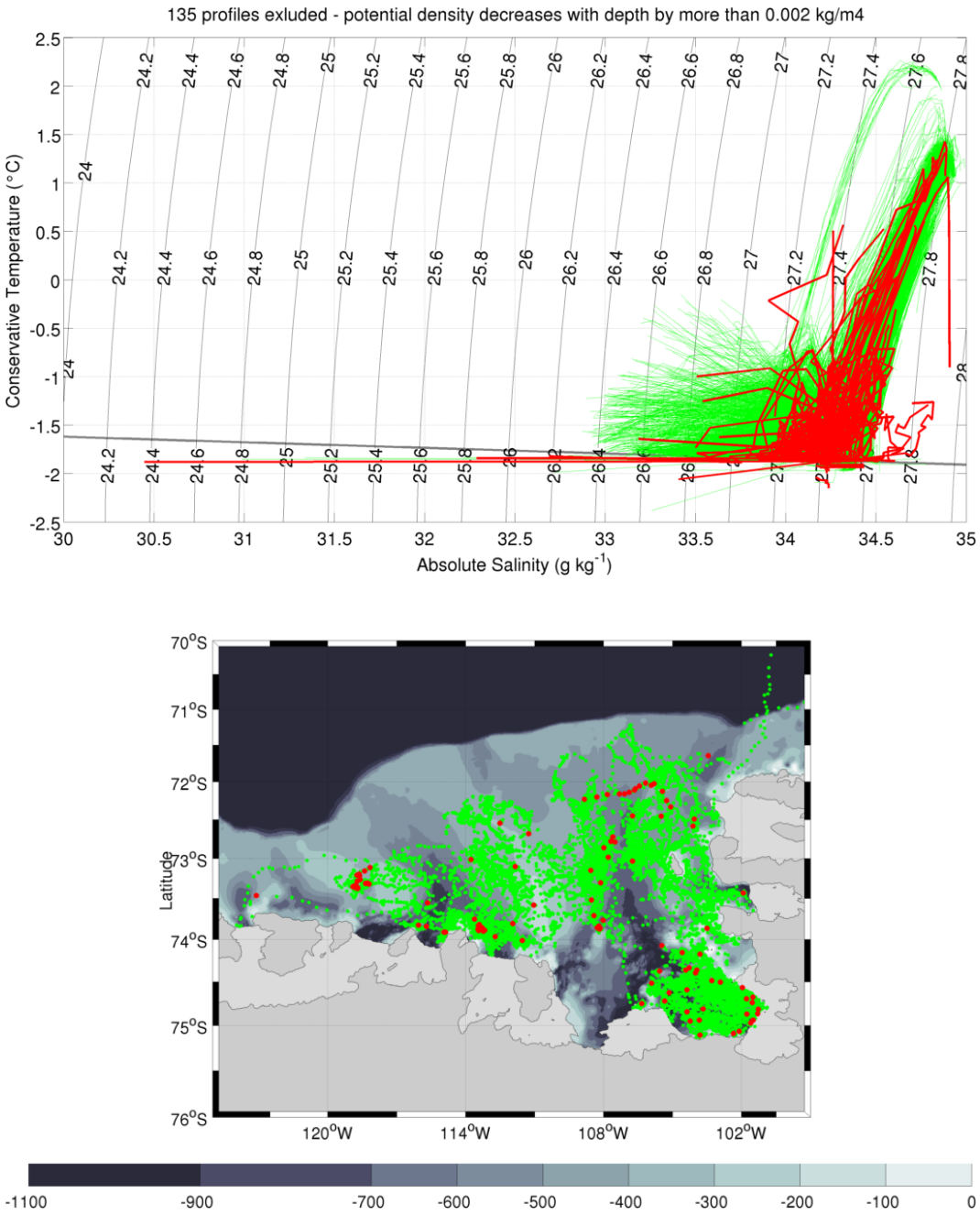

Figure 2.12: Top - Absolute salinity and conservative temperature for all profiles (green) and for profiles excluded as unstable, where potential density decreases with depth by more than 0.002 kg/m3 per db (red). Bottom - locations of these profiles.

Excluded are only the most unstable profiles, as 58% of the seal profiles have some degree of instability. 135 such profiles are flagged (Figure 2.12).

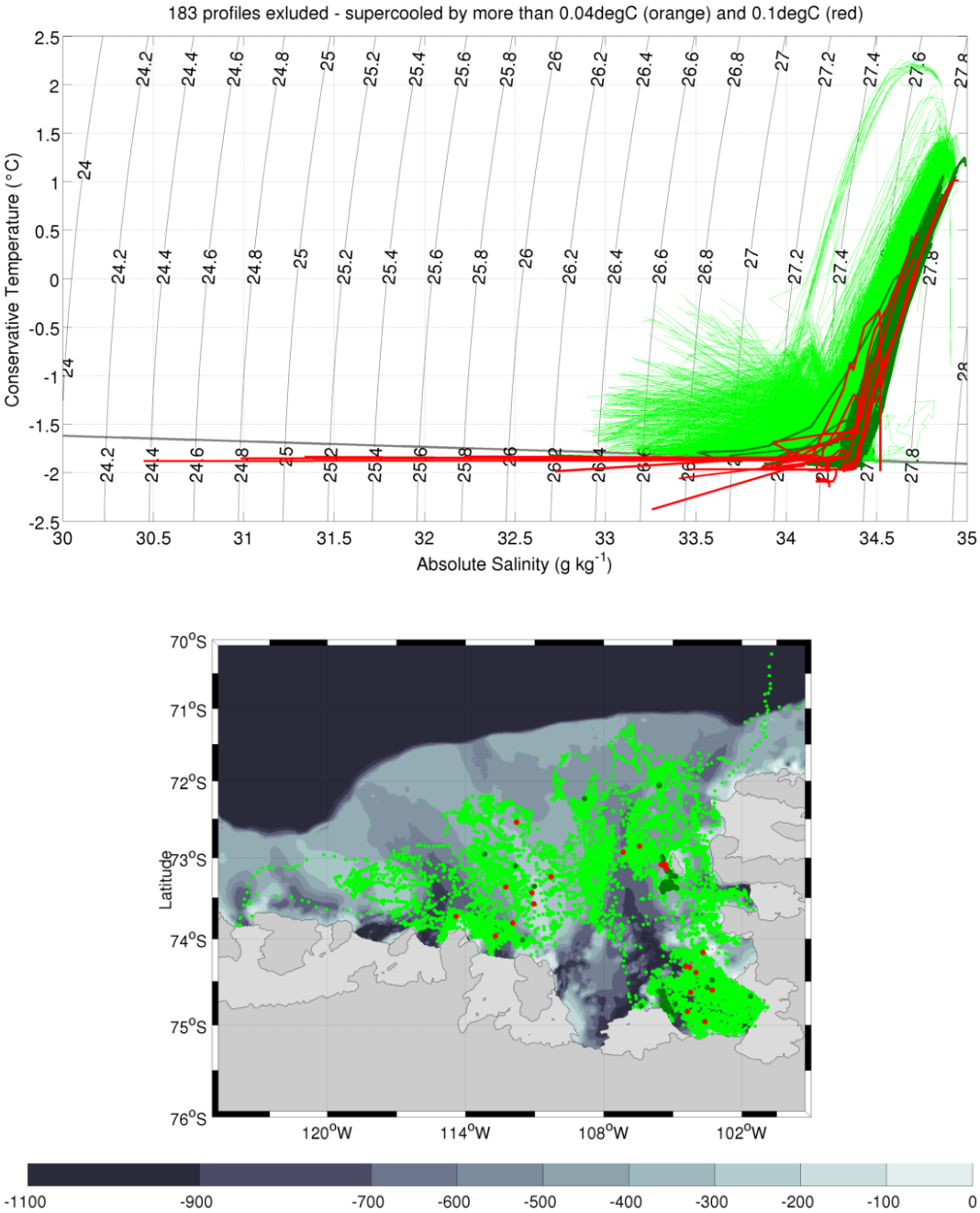

Figure 2.13: Top - Absolute salinity and conservative temperature for all profiles (green) and for profiles supercooled by more than 0.04 °C (dark green), and for profiles supercooled by more than 0.1 °C (red). Bottom - locations of these profiles.

There are many profiles which include some observation which is supercooled. Some proportion of profiles are expected to falsely observe supercooled waters, as a result of the accuracy of the sensor (0.03 °C). Observed here are a large number of profiles (183+)

which observe supercooled water beyond the margin of error (dark green, figure 2.13, and these observations are mostly clustered around Thwaites glacier and around Burke Island. Although these profiles are mostly observed by two tags (896 - 112 profiles, 858 - 54 profiles, table 2.5), these are the tags responsible for sampling these two areas, so the observations cannot easily be put down to tag errors. As such, these profiles are not considered to be erroneous. However, 23 profiles observe water supercooled to such a degree (greater than 0.1 °C) that these observations are considered erroneous and are excluded (red, figure 2.13).

Table 2.5: Additional quality control

Species	Sex	Tag	Number of profiles unstable	Number of profiles too fresh	Number of profiles too salty at surface	Number of profiles a with supercooling (0.04)	Number of profiles too supercooled (0.1)	Number of profiles flagged
Elephant	F	838	10	0	0	0	0	10
Elephant	F	960	25	1	4	1	1	26
Elephant	F	970	8	0	8	1	1	17
Elephant	M	889	2	0	0	1	1	3
Elephant	M	959	2	1	0	1	0	2
Elephant	M	961	3	0	1	1	1	5
Elephant	M	971	0	0	1	0	0	1
Weddell	F	858	15	4	0	54	7	22
Weddell	F	893	20	2	0	2	1	22
Weddell	F	895	17	0	0	3	0	17
Weddell	F	896	4	1	1	112	6	12
Weddell	F	963	3	1	0	5	4	6
Weddell	M	890	3	1	0	2	1	4
Weddell	M	972	23	0	0	0	0	23
Totals	–	–	135	11	15	183	23	170

These additional quality control measures are designed to exclude only the most obviously erroneous observations, and strive to exclude as little as possible, in order to reduce the likelihood of excluding unusual but true observations. A total of 170 profiles are flagged (table 2.5), from 11,307 profiles received (1.5%).

2.7 Proposed improvements to the tag algorithm

The ocean mixed layer is a variable depth surface layer with near uniform properties down through its depth, and a gradient of properties at the base of the layer (Dong *et al.*, 2008). It is through the mixed layer that the atmosphere and ocean interact, with fluxes of heat, momentum and freshwater passing through, and the thickness of this layer determines the volume of water interacting with the atmosphere at any single location (Dong *et al.*, 2008). As such, accurate estimation of mixed layer depth (MLD) is essential. The seal tag profile reduction algorithm used to collect this dataset does not consider mixed layer depth, and this information is hard to extract accurately afterwards. It would be useful for the tag algorithm to find and include the MLD in the reduced profile.

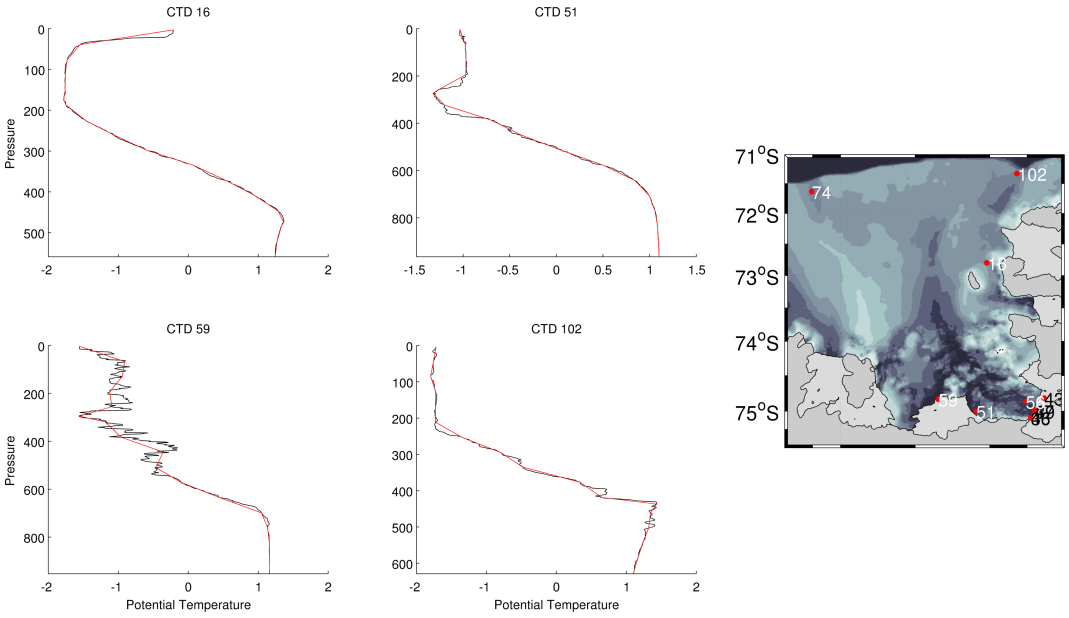

Figure 2.14: CTD profile from ship CTD (black), and the same profiles processed by the tag algorithm (red). Top left - CTD 16, near Burke Island. Top middle - CTD 51, near the east of Thwaites. Bottom left - CTD 59, near the north of Thwaites. Bottom middle - CTD 102, at the shelf break in the Eastern Trough. Right - map of CTD locations for this figure, and for those in figure 2.15.

Presented in figures 2.14 and 2.15 are various ship CTD profiles (black) in a spread of locations, and as they would be seen processed by the seal tag algorithm (red). The algorithm is explained fully in section 2.2. The coarse resolution of the reduced profile often means that a shallow mixed layer is obscured by the tag algorithm (Figure 2.14, CTD 16), or that a deeper mixed layer is broadened and its depth misrepresented (Figure 2.14, CTD 51). The tag algorithm also obscures much of the fine structure seen in the upper 500 m (Figures 2.14, CTD 59, and 2.15, CTDS 39,47,56), and although this is unavoidable when representing a profile with just 18 points, it can complicate calculation of the MLD (Figure 2.15, CTD 39). The tag algorithm generally represents the deep water very well.

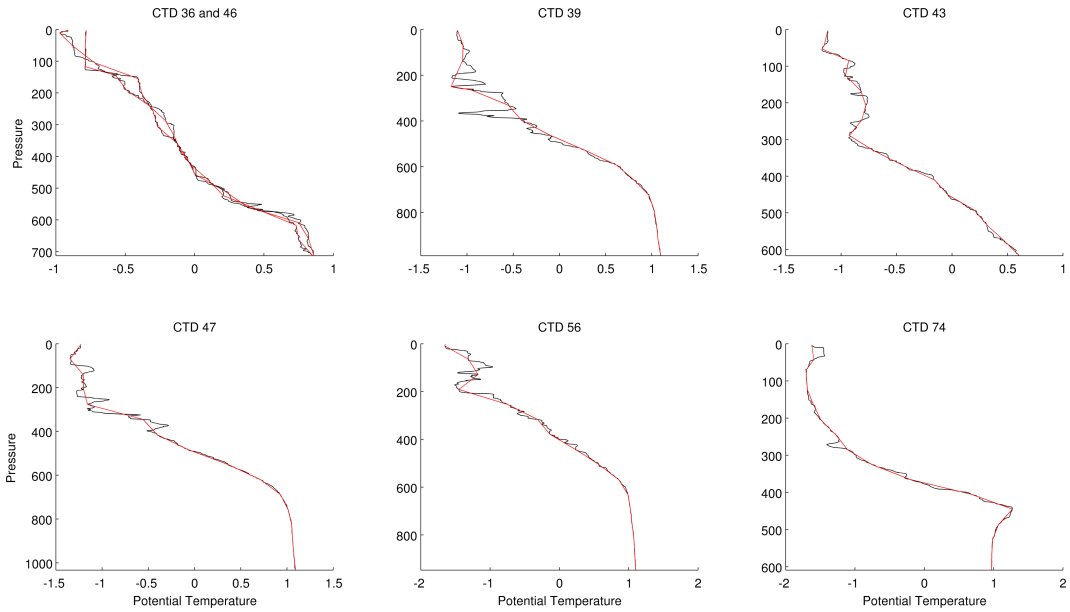

Figure 2.15: CTD profile from ship CTD (black), and the same profiles processed by tag algorithm (red). Top left - CTDs 36 and 46, at the southern corner of PIG. Top middle - CTD 39, near the middle of PIG. Top right - CTD 43, near the middle of PIG. Bottom left - CTD 47, the location of mooring ISTAR 9. Bottom middle - CTD 56, the location of ISTAR 8. Bottom right - CTD 74, at the shelf break in the central trough.

Several methods have been put forward through the years for calculating MLD, and thresholds for difference in temperature or density from near-surface values are a common choice, although appropriate thresholds vary with location. Near-surface reference points, rather than true surface values, are often used in order to avoid the diurnal heating cycle observed in the surface few metres (de Boyer Montégut *et al.*, 2004). For temperature difference thresholds, de Boyer Montégut *et al.* (2004) use a global value of 0.2° C, from a near-surface reference level of 10 m. Dong *et al.* (2008) report that commonly used

thresholds range from 0.01° C to 1.0° C .For density difference thresholds, Dong *et al.* (2008) report values ranging from 0.005 kg/m^3 to 0.125 kg/m^3). Other methods use a threshold in property change with depth. Dong *et al.* (2008) report temperature gradient thresholds of 0.025° C/m and, and density gradient thresholds of 0.0005 kg/m^4 to 0.05 kg/m^4. Lorbacher *et al.* (2006) use the shallowest extreme curvature in the temperature profile to find the MLD. More recently, algorithms have been put forward to choose the likeliest of multiple MLDs calculated using different methods (Holte and Talley, 2009), and Holte and Talley (2009) find that temperature criteria often overestimate MLDs, particularly in the Southern Ocean winter, where temperature and density gradients beneath the thermocline are reduced.

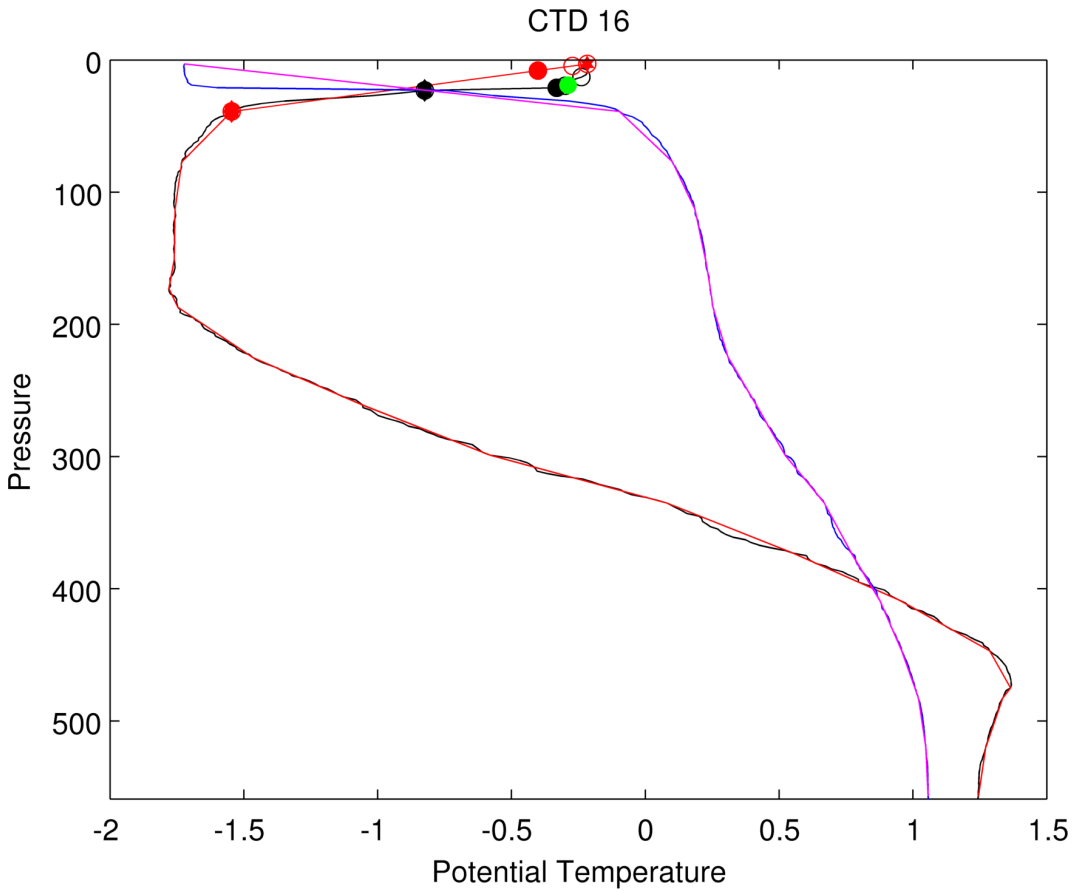

Figure 2.16: Temperature (black) and potential density (blue) of the ship CTD profile, and as processed by the tag algorithm (red and pink). The true MLD is marked in green. The black square marks the temperature difference threshold MLD, the black diamond marks the density difference threshold MLD, and the black star marks the temperature gradient threshold MLD. Where available, the Holte and Talley (2009) algorithm MLD is plotted, along with the various MLDs calculated as part of the algorithm (black circle, empty). Of these, the temperature difference threshold method is marked with a filled black circle. The equivalent MLDs for the reduced profile are marked in red.

The inclusion of the MLD in the tag compression algorithm would provide a substantial number of MLD observations, and would aid in interpretation of the seasonal cycle in shallow water when using seal tag observations. Here 105 ship-based CTD profiles collected in the Amundsen Sea in 2014 as part of the iStar project (Heywood *et al.*, 2014) are used to examine methods for calculating MLDs, in order to pick one appropriate for the water masses of the Amundsen Sea, that performs appropriately when used with seal tag data. It should be noted that these ship CTD profiles are from summer, while much of the seal tag observations are from winter, and that this may affect the accuracy of the chosen method when applied to seal data. A true MLD is found visually for each profile, and then MLDs are calculated using various methods. The CTD profile is then put through a seal-tag reduction algorithm, and the same MLD calculation methods applied. Figure 2.16 shows this for CTD 16. Different MLD methods work better for different profiles in different places and different seasons, as seen by the spread in figure 2.17. It is also clear how, for some profiles, it is impossible to calculate an accurate MLD from the reduced seal tag profiles (red and pink, figure 2.16).

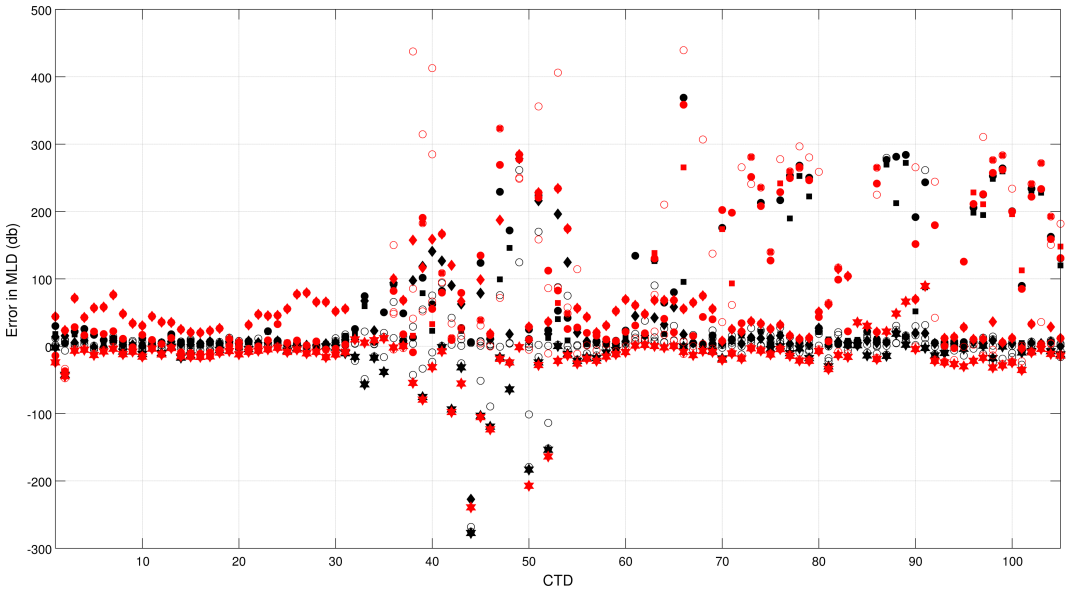

Figure 2.17: Error in MLD calculation, for each method, for each CTD. Calculated MLDs minus true MLDs. In black are the MLD errors of the original CTD profiles, and in red the MLD errors of the CTD profiles as output by the seal tag algorithm. The symbols are as described in figure 2.16.

The difference between these calculated MLDs and the true MLDs for each CTD is plotted in figure 2.17, emphasising that variability in accuracy of different MLD methods

for different profiles. CTDs 1 to 31 are in along the eastern trough, from shelf break towards Pine Island Bay. CTDs 32 to 54 are in Pine Island Bay, along PIG and the eastern edge of Thwaites. CTDs 55 to 69 are north of Thwaites. CTDs 70 to 105 are mostly at the shelf break in the central and eastern troughs. Each of these sets have a different spread in MLD accuracy, and in which of the MLD methods produce the most erroneous results.

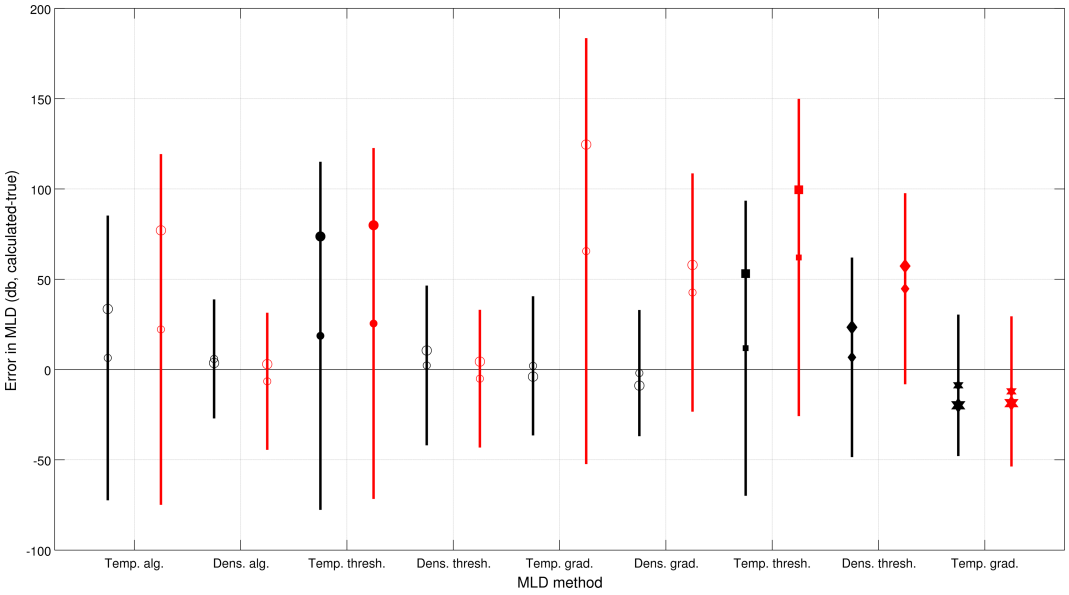

Figure 2.18: Mean (larger marker), median (smaller marker), and standard deviation (lines, from medians) of the error in MLD calculation, for each method. Calculated MLDs minus true MLDs. In black are the MLD errors of the original CTD profiles, and next to them in red the MLD errors of the CTD profiles as output by the seal tag algorithm. The first 6 methods are from the Holte and Talley (2009) algorithm, the MLD of their temperature algorithm, the MLD of their density algorithm, the temperature and density difference threshold MLDs, and the temperature and density gradient threshold MLDs. The last three methods are the additional MLD methods described previously. Symbols relate to different methods, as in figure 2.17.

The density algorithm of Holte and Talley (2009) has the least standard deviation, with a mean and median error not far from the true MLD (figure 2.18). This is not too much worse for the reduced profile (red) than the full profile (black). The Holte and Talley (2009) density threshold method performs similarly. The additional temperature gradient method has a similar standard deviation, but the calculated MLDs are consistently shallower than the true MLDs, perhaps improvable by adjusting the threshold. The temperature threshold and gradient threshold methods perform particularly badly, likely a result of the seasonally variable difference in temperature between the mixed layer and the water beneath. The results suggest that the Holte and Talley (2009) density algorithm is the best method to use, and that the MLDs calculated from the reduced seal tag profiles

are less accurate and less precise, for most of the methods tested. The density algorithm will sometimes use the density gradient threshold method, for which the reduced seal tag profile produces much less accurate and less precise MLDs, and so the reduced seal tag profiles cannot be used to produce MLDs of similar quality to the original CTD profiles, even with the best MLD method. It is suggested that this or a similar method is used by the tag to include the MLD in the reduced profile. This could replace one of the 14 equally spaced pressure levels, so as not to increase the volume of data sent by the tags. Alternatively, the broken-stick algorithm used in other tags (which is designed to report the most important inflection points) could be used, but with the forced inclusion of the deep temperature maximum, to retain the good representation of the all important CDW seen in the tags here. Provided those inflection points were derived from both the temperature and density profiles, the MLD would be well represented.

Adjusting the seal tag compression algorithm to fit the study area, expected water masses and questions of interest is the obvious way maximise the value of a seal tag deployment. The dataset presented in this thesis included the subsurface temperature maximum in the compression algorithm, in order to target the deep, warm CDW. This choice proved effective, and it is analysis of this water mass which follows in chapter 3.

2.8 Summary

Comprehensive corrections have been applied, accounting for head effect, location inaccuracies, pressure offsets, temperature and salinity corrections and pressure dependent sensor errors. It is these pressure dependent sensor errors that are the most surprising and the most worrying, and which will need to be addressed in seal tag deployments. With the aid of pre-deployment tag tests against a ship-board CTD, these errors can be found and adjusted for, and so the essential work here makes this dataset available for the analysis to follow in chapters 3 and 4.

After multiple quality control filters, the final seal tag dataset is 93% of its original size (Table 2.6). Some tags performed much worse than others - most kept 98 to 99 %

of their profiles through this process, while tag 960 retained just 59% of its profiles (Table 2.6). This is to be expected - some tags will perform badly, through malfunction or through obstruction of the sensors.

Table 2.6: Profile number before and after entire corrections and QC process

Species / Group	Sex	Tag	Number of profiles, intially	Number of profiles, after all QC and corrections	% Of initial profiles that passed QC
All			11307	10510	93
All female			7975	7258	91
All male			3332	3252	98
All Elephant			5381	4803	89
All Weddell			5926	5707	96
Elephant	F	838	1268	1252	99
Elephant	F	960	905	536	55
Elephant	F	970	1171	999	85
Elephant	M	889	347	343	99
Elephant	M	959	429	422	98
Elephant	M	961	1146	1138	99
Elephant	M	971	115	113	98
Weddell	F	858	854	761	89
Weddell	F	893	870	843	97
Weddell	F	895	988	967	98
Weddell	F	896	1015	1001	99
Weddell	F	963	904	889	98
Weddell	M	890	405	401	99
Weddell	M	972	890	835	94

Improvements to the tag algorithm have been proposed - by targeting the MLD upper

ocean processes will be much more easily analysed in future deployments. These improvements are, of course, specific to the study area and research questions. In chapter 4, upper ocean variability is investigated in depth, emphasising the value of this proposed change in the tag algorithm.

Chapter 3

Variation in the distribution and properties of circumpolar deep water in the eastern Amundsen Sea, on seasonal timescales, using seal-borne tags

In Chapter 2 thorough corrections, quality control and processing were completed on the seal tag data, such that confidence can be had in the quality of the dataset. This essential step enables further analysis of the dataset, allowing us to ask and answer key scientific questions by examining differences in water masses in space and time. In Chapter 3, the variation in the distribution and properties of CDW in particular is examined, in an effort to answer some of the knowledge gaps highlighted in Chapter 1.

This chapter utilises the seal-tag data to demonstrate the seasonal variations seen in CDW in the Amundsen Sea in 2014. Identifying and quantifying any seasonal variability in CDW is essential, since most data currently available to models predicting sea level rise is from summer, and potentially different conditions in winter are not incorporated. Thus, any resultant changes to predicted sea level rise are unknown. In this chapter we find seasonal differences in CDW layer thickness and CDW properties on density surfaces

which are not the same as seasonal differences observed elsewhere on the Amundsen Sea continental shelf. We find coherent changes occur on the scale of approximately 150km.

The following chapter was published as a paper in Geophysical Research Letters as 'Variation in the distribution and properties of circumpolar deep water in the eastern Amundsen Sea, on seasonal timescales, using seal-borne tags' with co-authors Karen J. Heywood, David P. Stevens, Lars Boehme, Mike Fedak, and Fabien Roquet (Mallett *et al.*, 2018). All writing and work was undertaken by Helen K. W. Mallett, with comments and input from collaborators. It is included here as published, and the supplementary figures are included with some explanatory text in appendix B. Additional previously unpublished analysis is provided in appendix C, which was omitted from the paper in the interests of brevity, but is included here to aid further understanding of CDW in the Amundsen Sea as a whole, and to make full use of the available data. Text in [square brackets] was not in the original paper.

Mallett, H. K. W., Boehme, L., Fedak, M., Heywood, K. J., Stevens, D. P., & Roquet, F. (2018), Variation in the distribution and properties of circumpolar deep water in the eastern Amundsen Sea, on seasonal timescales, using seal-borne tags, *Geophysical Research Letters*, 45. https://doi.org/10.1029/2018GL077430

3.1 Abstract

In the Amundsen Sea, warm saline Circumpolar Deep Water (CDW) crosses the continental shelf toward the vulnerable West Antarctic ice shelves, contributing to their basal melting. Due to lack of observations, little is known about the spatial and temporal variability of CDW, particularly seasonally. A new dataset of 6704 seal-tag temperature and salinity profiles in the easternmost trough between February and December 2014 reveals a CDW layer on average 49 db thicker in late winter (August to October) than in late summer (February to April), the reverse seasonality of that seen at moorings in the western trough. This layer contains more heat in winter, but on the 27.76 kg/m^3 density surface

CDW is 0.32°C warmer in summer than winter, across the northeastern Amundsen sea, which may indicate wintertime shoaling offshelf changes CDW properties onshelf. In Pine Island Bay these seasonal changes on density surfaces are reduced, likely by gyre circulation.

3.2 Introduction

Loss of the unstable West Antarctic ice sheet could produce sea level rise of 3.2 m (Bamber *et al.*, 2009) if it melts completely, of which approximately 40% by volume would drain via the Pine Island Glacier and Thwaites Glacier (Payne *et al.*, 2004). The Pine Island Glacier is thinning (Paolo *et al.*, 2015) and accelerating (Mouginot *et al.*, 2014; Rignot *et al.*, 2014). Warm, saline Circumpolar Deep Water (CDW) is implicated in this acceleration, flowing southward across the Amundsen Sea continental shelf from the open ocean and mixing with the shelf sea water masses. This modified CDW (henceforth CDW) is characterized by a subsurface temperature maximum, typically greater than 0°C, with absolute salinities greater than 34.7 g/kg. It flows beneath the thermocline at 350 to 650 m (Jacobs *et al.*, 2011; Dutrieux *et al.*, 2014), penetrating the Pine Island ice shelf cavity (Jenkins *et al.*, 1997), melting and thinning the ice shelf from below. This thinning reduces the buttressing provided by the ice shelf, allowing Pine Island Glacier to accelerate and thin (Thomas, 1979). Identifying the spatial and temporal variability of CDW, and the mechanisms that drive this variability, is essential for validating the models that project the long term melt rates of Pine Island Glacier and the resultant sea level rise. Key questions include: how thick and how warm is the CDW layer near the continental shelf, how are the thickness and temperature of the CDW layer modified as it flows south to the Pine Island ice shelf cavity, and do the temperature and thickness vary seasonally.

CDW flows onto the Amundsen Sea continental shelf via three bathymetric troughs (Figure 3.1) (Nitsche *et al.*, 2007), the eastern and central of which lead to Pine Island ice shelf. For CDW to reach the ice shelf grounding line, it must overtop a ridge at 700 m depth within the cavity beneath the shelf (Jenkins *et al.*, 2010). The temperature of the CDW between the cavity ceiling and the ridge (between 500 and 700 m) is particularly

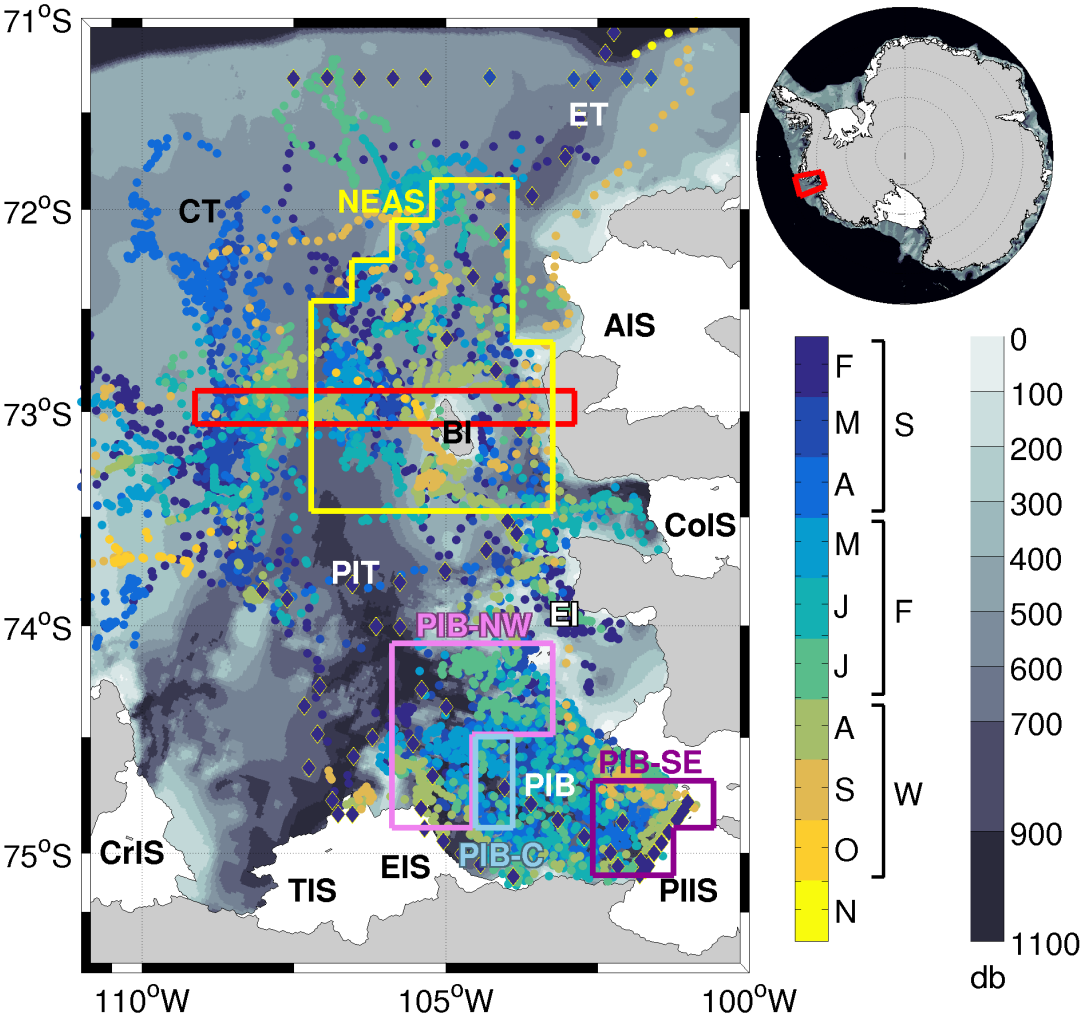

Figure 3.1: The eastern Amundsen Sea, with CTD profiles collected by seals (dots) and ship (diamonds), colored by date. Winter profile locations overlie some summer and fall locations. CTD locations overlie seal locations. The seasons used in analysis are marked alongside the date colorbar. Features marked: Crosson Ice Shelf (CrIS), Thwaites Ice Shelf (TIS), Eastern Ice Shelf (EIS), Pine Island Ice Shelf (PIIS), Cosgrove Ice Shelf (CoIS), Abbot Ice Shelf (AIS), Burke Island (BI), Eastern Trough (ET), Central Trough (CT), Pine Island Trough (PIT), Pine Island Bay (PIB) and the Edwards Islands (EI). The red rectangle contains the observations used for Figure 3.2. Marked in yellow, pink, blue and purple are the four regions used in Figure 3.4, north eastern Amundsen Sea (NEAS), Pine Island Bay north west (PIB-NW), Pine Island Bay central (PIB-C) and Pine Island Bay south east (PIB-SE). Inset is Antarctica, with the eastern Amundsen Sea marked in red. Bathymetry is IBCSO (Arndt *et al.*, 2013), coastline and grounding line are Bedmap2 in white and gray (Fretwell *et al.*, 2013).

relevant for understanding basal melting of the ice shelf, as it provides the heat for this melting.

Oceanographic observations in the Amundsen Sea are limited. Ice-cover and harsh weather restrict ship access, limit mooring deployment and mooring retrieval, and prevent good spatial and temporal data coverage across the shelf. The vast majority of historical

measurements in the Amundsen Sea are from summer, the only winter observations from a sparse distribution of moorings (Heywood *et al.*, 2016). There are no near-surface winter observations, since drifting icebergs can catch and drag any mooring that is positioned too close to the surface. Thus, understanding of the seasonal variability on the shelf is severely restricted. Some models suggest a winter - spring (June - November) maximum in CDW onflow in the central trough as a result of seasonal changes in the wind field (Thoma *et al.*, 2008), with CDW thickness peaking in late winter - spring (Thoma *et al.*, 2008; Steig *et al.*, 2012). Schodlok *et al.* (2012) modeled southward heat transport and CDW thickness peaking in fall (March-May) in the eastern trough, and St-Laurent *et al.* (2015) modeled a late winter (August-October) minimum in heat content below 250 m at PIG. Nakayama et al. (2017) find no large seasonal variability at 552 m at the eastern trough shelf break, though they find January warmer and saltier than June at 222 m. Year-round hydrographic observations are therefore needed to resolve this debate.

Previous work suggests that seasonal change in CDW thickness is different in different troughs. Wåhlin *et al.* (2013) found that both bottom temperature and CDW thickness peaked in fall (March-May) in the western trough, using mooring data collected between February 2010 and March 2012. In Pine Island Bay (PIB) a minimum in CDW thickness is seen in summer by Webber *et al.* (2017) using 5 years of mooring data, the reverse seasonality of that seen in the western trough. How representative the observations at these mooring locations are of the rest of their respective troughs remains to be assessed.

Here we investigate seasonal change in the location, properties and thickness of the CDW layer in the eastern trough using, to-date, the only dataset capable of providing the necessary broad spatial coverage through the seasons.

3.3 Methods

A total of 14 Conductivity-Temperature Depth - Satellite Relayed Data Loggers (CTD-SRDL, (Boehme *et al.*, 2009)) were deployed between 8th and 26th February 2014. 7 Southern Elephant seals (*Mirounga leonina*) were captured and tagged at the Edwards

Islands (Figure 3.1[, red box], 73°52'S 102°59'W) and 7 Weddell seals (*Leptonychotes weddellii*) on sea ice between 72°23'S, 108°46'W and 72°56'S, 110°19'W. Half of the tags were still transmitting in September, with the last good quality measurements received on 1st December.

The tags reduce each conductivity-temperature-depth (CTD) profile into 17 or 18 depth levels using a broken-stick method, in order to maximize data transfer via the Argos satellite-based system (Boehme *et al.*, 2009; Photopoulou *et al.*, 2015). This method samples the temperature maximum deeper than 100 db (ie CDW), and the temperature minimum. Only the deepest cast of every 4 hours is transmitted, ensuring the best possible temporal and spatial resolution for the limited battery power available and the data throughput limitations of the Argos system (Boehme *et al.*, 2009; Fedak *et al.*, 2002; Fedak, 2004).

Corrections were applied to the profile locations, derived using a Kalman smoother (Lopez *et al.*, 2015), and corrections to temperature and salinity were found from pre-deployment comparisons with ship-based CTD measurements. Profiles then underwent standard Delayed Mode Quality Control processing of the Marine Animals Exploring the Oceans Pole to Pole (MEOP) project ((Roquet *et al.*, 2011, 2013), http://www.meop.net/). The presented dataset has a nominal accuracy of +/-0.03° C for temperature and +/-0.05 for practical salinity (Roquet *et al.*, 2014) (absolute salinity accuracy can be considered comparable). It is estimated that the true accuracy of the salinity measurements is closer to +/-0.03, but as the conductivity sensor is known to introduce an extra offset when the CTD-SRDL is attached to the animal, we can use this accuracy estimate only as an indication. We use the TEOS-10 standard (McDougall and Barker, 2011). There were 11,307 profiles successfully received by Argos, of which 10,838 passed quality control. 6,704 of these have both temperature and salinity measurements, are in the eastern Amundsen Sea and are used in the following analysis.

In the following analysis we group the profiles into regions to enable comparison between the seasons, and grid into cells 23 km latitudinally by 22 km longitudinally. We

focus on the eastern shelf, where the warmest CDW was observed, and particularly near Burke Island and in PIB, where there are sufficient numbers of profiles throughout the observation period to make statistically robust seasonal comparisons (Figure 3.1). We also extract sections from the dataset, using an elongated rectangular area to approximate a linear section with a meridional range of 18 km (Figure 3.1).

We include 105 ship-based CTD profiles (diamonds, Figure 3.1), collected between 1st February and 5th March 2014 as part of the iSTAR JR294/295 cruise (Heywood *et al.*, 2016). Seasonal analysis would not be possible with the ship-CTD measurements alone, as they are all from summer. These ship-based CTD profiles have a much higher vertical resolution [and accuracy]. Both seal and ship-based observations are vertically gridded[/up-sampled] onto a pressure grid of resolution 1 db and a density grid of resolution 0.00167 kg/m^3. Subsequent analysis does not differentiate between data sources. By number of profiles, the seal tag profiles provide 98.8% of the final dataset.

In order to separate observations of seasonality that result from changes in flow, from those that result from changes to the CDW properties, we examine seasonal differences on isopycnal surfaces. For this we choose the 27.76 kg/m^3 isopycnal (unit for density omitted hereafter), a surface approximately 100 db shallower than the core of the CDW, shallow enough for many seal profiles to sample it, but close enough to the core to behave similarly (Figure 3.2b and 3.2d). The 0°C isotherm can be considered the upper boundary of the CDW layer.

For four regions of interest (Figure 3.1) we calculate median profiles of conservative temperature against potential density anomaly, averaged on density, where at least 10 profiles are available, and using only observations in cells where data are available in all relevant seasons. Profiles are first averaged into cells, and then between the cells within a region, to eliminate regional bias. Only profiles that are sufficiently deep to reach water warmer than 0°C are included. Median profiles are also calculated for potential density anomaly, conservative temperature and absolute salinity against pressure, averaged on pressure.

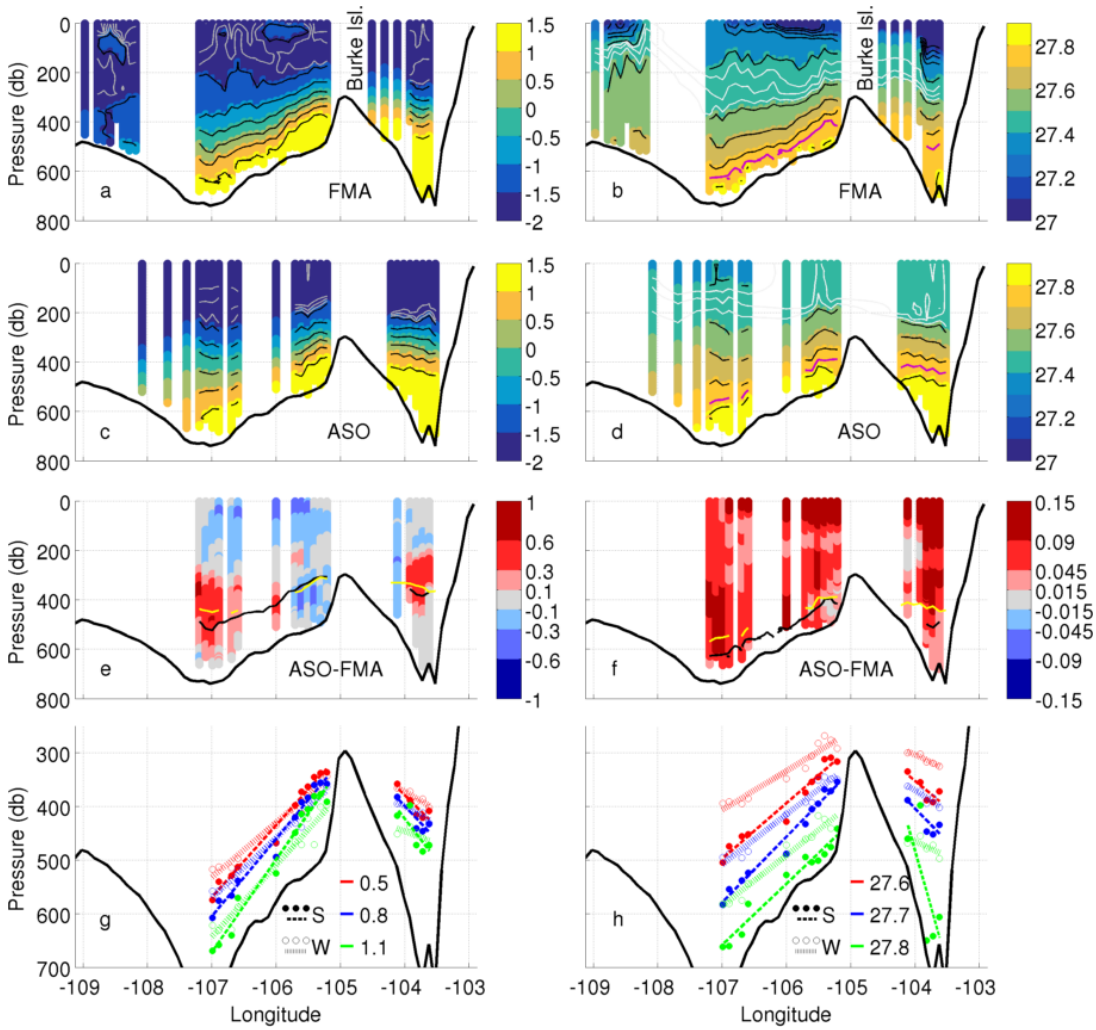

Figure 3.2: Conservative temperature of the section marked (Figure 3.1, red rectangle) for summer (a) and winter (c), averaged into 0.1° longitude bands. Black contours are 1.5 to -1.5°C isotherms in increments of 0.5°C. Gray[/white] contours are -1.5, -1.6, -1.7 and -1.8°C isotherms. The thick black line is the deepest bathymetry within each 0.1° longitude band of the section (IBCSO, (Arndt *et al.*, 2013)). (e) difference in temperature, winter - summer, where observations are available in both seasons. Red means water is warmer in winter than summer. Black and yellow lines are 0°C isotherms in summer and winter respectively. (g) the slope of the 0.5, 0.8 and 1°C isotherms in summer and winter. Dots are the seal observations, lines are linear regression, one each side of Burke Island. (b,d) as in (a,c) but for potential density anomaly. Black contours are 27 to 27.9 isopycnals in increments of 0.1, and white contours are the 27.425, 27.450, and 27.475 isopycnals. The purple contour is the 27.76 isopycnal. (f) as in (e) but for potential density anomaly. Black and yellow lines are 27.76 isopycnals in summer and winter respectively. (h) as in (g) but for the 27.6, 27.7 and 27.8 isopycnals

These regions of interest are chosen where properties and seasonality are broadly consistent. The northeastern Amundsen Sea region (Figure 3.1) covers a large area where observations from all seasons are present and oceanographic conditions are similar. PIB is separated into three regions with different seasonal changes in the depth of the 27.76 isopycnal. There are insufficient observations in the rest of the Amundsen Sea for robust

seasonal analysis.

Using cells near Burke Island and profiles offshelf at the eastern trough (Figure 3.3g), we compare the properties of source CDW with those onshelf by calculating mean conservative temperature and absolute salinity profiles for different seasons, averaged on density, to determine if changes in the depth of the isopycnals offshelf are responsible for some of the observed seasonal changes in CDW properties.

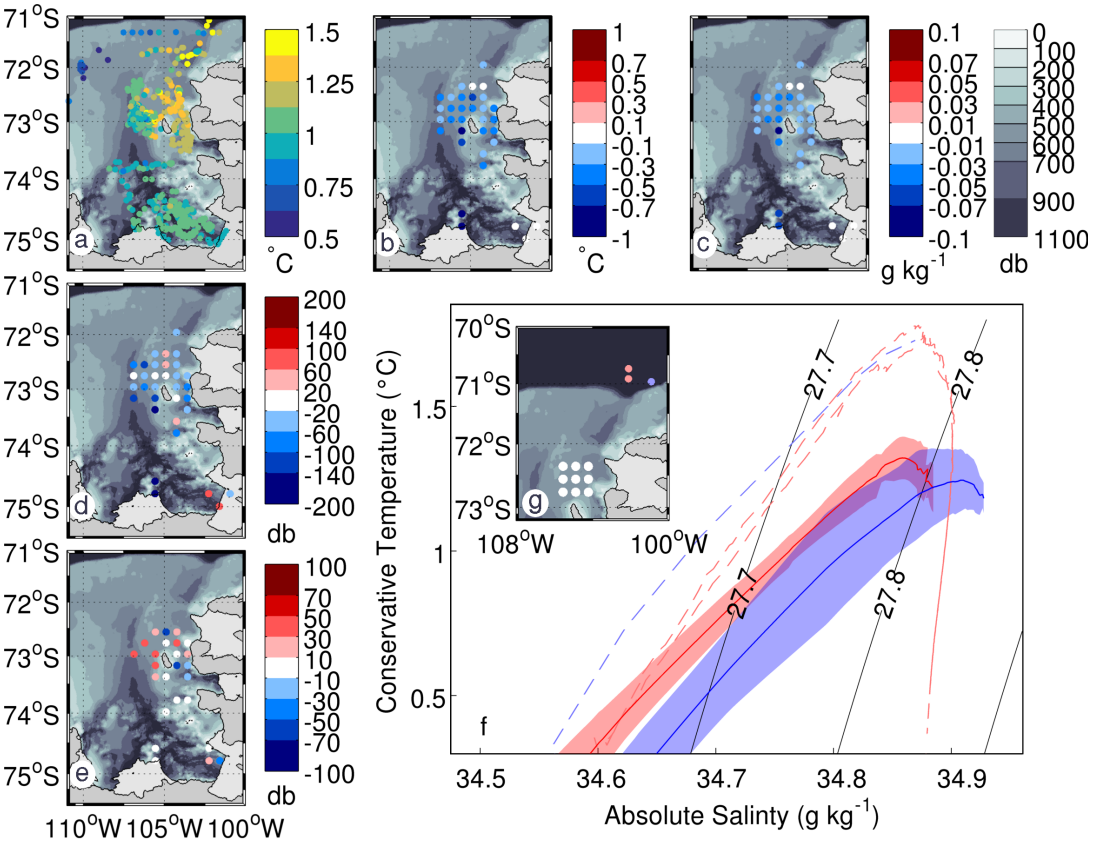

Figure 3.3: Conservative temperature on the 27.76 isopycnal in summer (a). (b) difference in conservative temperature, winter minus summer, on the 27.76 isopycnal, where red means winter is warmer than summer. Observations are gridded in longitude and latitude on isopycnal surfaces, enabling comparison between seasons. (c) as (b), but for absolute salinity in g/kg. (d) as (b), but showing difference in pressure of 27.76 isopycnal, where red means the isopycnal is deeper in winter. (e) difference in thickness of the CDW layer beneath the 0°C isotherm, winter minus summer, where red means the CDW layer in winter is thicker than summer. (f) conservative temperature and absolute salinity of a group of cells onshelf in winter (blue) and summer (red), shading indicating standard deviation. Dashed lines are profiles offshelf near the eastern trough in winter (blue) and summer (red). Black lines are isopycnals. (g) locations of these cells (white) and offshelf profiles (pale red and pale blue).

For this seasonal analysis we compare late summer (February, March and April (FMA), henceforth 'summer'), with late fall (May, June and July (MJJ), henceforth 'fall'),

and with late winter (August, September and October (ASO), henceforth 'winter'). Since there are few seal observations from November to January, these three seasons best represent the extrema of winter and summer from the available data. The addition of one or two fall months to the end of summer or to the beginning of winter, when comparing summer and winter, makes little difference to the conclusions drawn. There are many more observations in summer than winter, since more tags fail as the year progresses, so we compare the seasons only in locations where observations from both seasons are available.

3.4 Results

A zonal section north of Burke Island (Figure 3.1) reveals that the upper 150 m experiences the expected seasonal cycle of ice-melt freshening in summer, and surface cooling, mixed layer deepening and surface salinification from sea ice formation in winter (Figure 3.2, and for salinity, Figure B.1). The effect of salinification is detectable from the associated potential density anomaly (Figures 3.2b, 3.2d and 3.2f). Below 300 db, isotherms are shallower in winter than in summer, the CDW layer is warmer in winter than in summer on pressure surfaces (Figure 3.2e), and more saline (Figure B.1). An exception, just west of Burke Island where the deep isotherms, isohalines and isopycnals are locally deeper in winter than in summer (blue, Figures 3.2e and 3.2f), could be due to a small scale (approximately 10 km) westward shift in the isopycnals, resulting from a winter westward shift or decrease in the speed of the southward current here. Throughout the section, isopycnals (and isohalines) are shallower in winter, thus a thicker CDW layer is present, and this CDW layer is denser in winter than in summer on pressure surfaces. Between 107°W and 105.2°W, west of Burke Island, the deep isopycnals and isotherms are steeper in summer, suggesting faster flow (Figures 3.2g and 3.2h).

In the northeastern Amundsen Sea, between 71°S and 74°S and east of 111°W, the CDW layer underneath the 0°C isotherm is on average 5.6 db thicker in winter than in summer. This is variable over distances as small as 20 km, though coherent thickness change is observed over distances up to 100 km (Figure 3.3e). The mean temperature of this CDW layer, where both winter and summer data are available, is not measurably

different.

On the 27.76 isopycnal the warmest water on the continental shelf was in the eastern trough in February, at 1.64°C (Figure 3.3a). The CDW flows south both via Pine Island Trough and east of Burke Island (Figure 3.3a). It is not possible to judge whether or how much CDW arrives at PIB via the central trough, since the observations are sparse at the confluence of the two troughs. The warmest CDW in PIB, on the same isopycnal, is in May at 1.09°C, a reduction of 0.55°C from the shelf break temperature.

The 27.76 isopycnal is shallower in winter than summer through much of the northeastern Amundsen Sea (Figure 3.3d), by an average of 49 db, thus the CDW layer is thicker in winter. The 27.76 isopycnal, deeper than the 0°C isotherm, deepens farther south. The depth of the 0°C isotherm is also greater farther south, but to a much lesser degree, and is more variable on spatial scales of the order 20 km. As such the 27.76 isopycnal is considered a more reliable judge of CDW layer thickness change than the 0°C isotherm. The 27.76 isopycnal is warmest and most saline in summer and coolest and freshest in winter (Figures 3.3b and 3.3c). Summer is an average of 0.32 °C warmer than winter, using an area-weighted average where observations for both seasons are available (Figure 3.3b). Adjustments to the choice of isopycnal surface do not change the conclusions.

In the northeastern Amundsen Sea, isopycnals deeper than 200 db are shallower in winter than summer by approximately 100 db (Figure 3.4i). The pressures of isopycnals between 100 and 500 db are very similar in fall to those in summer. Below 500 db, in the CDW water mass, the pressures of isopycnals in fall are between those in summer and winter, suggesting that here the CDW layer thickness increases gradually from summer to winter. Temperatures are between 0.2 and 0.5°C colder in winter than in summer on isopycnals in the northeastern Amundsen Sea (Figure 3.4e). For cells north of Burke Island (Figure 3.3g), the mean winter profile in temperature - salinity space has a cooler and deeper endpoint from within the offshelf source CDW water than the mean summer profile (Figure 3.3f).

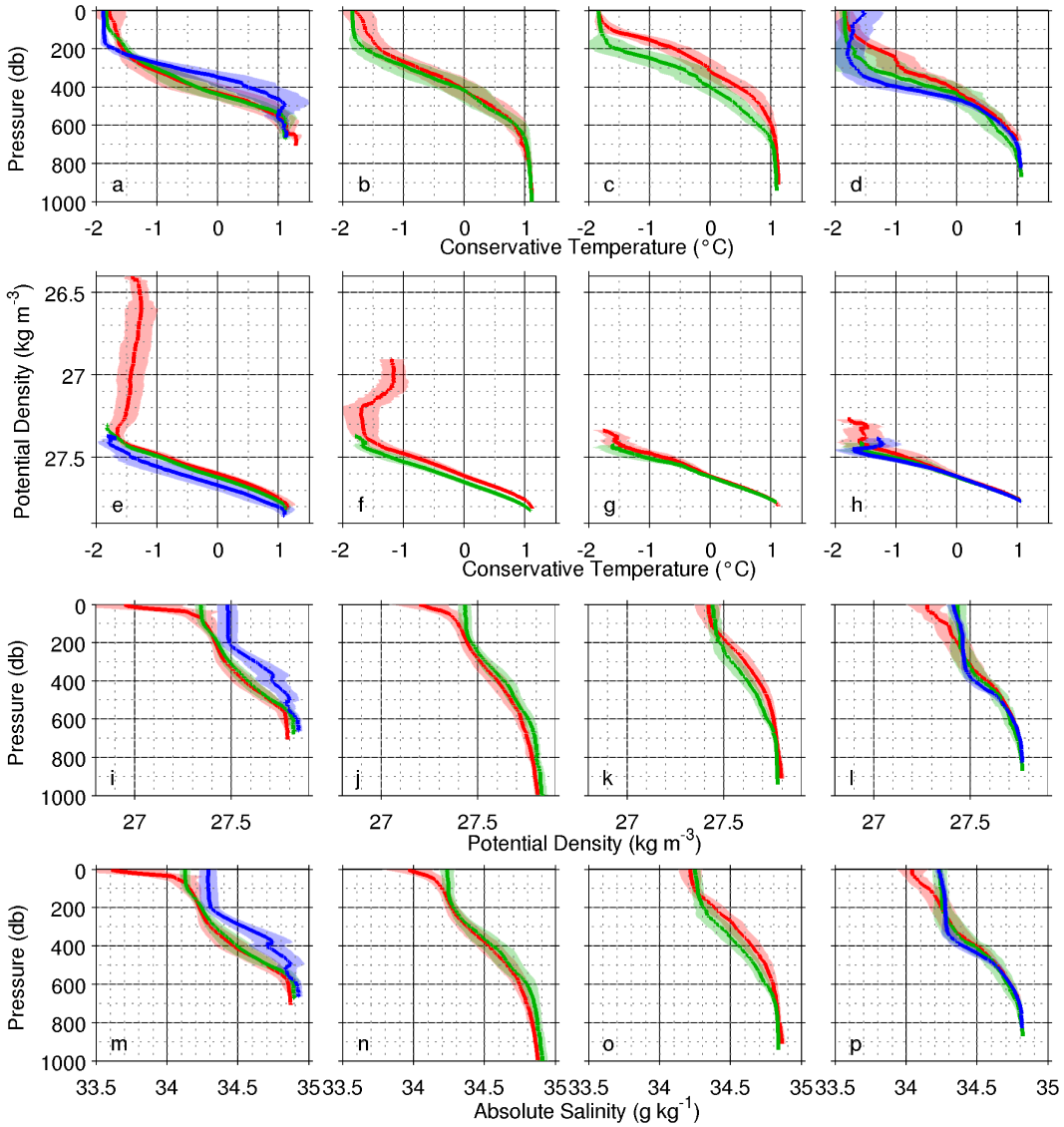

Figure 3.4: Median profiles and standard deviations (pastel shading) for summer (red), fall (green) and winter (blue) for regions marked in Figure 3.3e. Means are very similar to the medians and so are omitted. (a) profiles of conservative temperature against pressure. Profiles are from the northeastern Amundsen Sea, including only cells where data for both summer and winter are available. (e) profiles of conservative temperature against potential density anomaly, for the same region. (i) profiles of potential density against pressure. (m) profiles of absolute salinity against pressure. (b,f,j,n) as in (a,e,i,m), but for PIB-NW, for only cells where profiles from both summer and fall are available. There are less than 10 profiles in winter, so the winter average profiles are not plotted. (c,g,k,o) as in (b,f,j,n), but for PIB-C. (d,h,l,p) as in (a,e,i,m), but for PIB-SE.

In PIB North West (PIB-NW, pink, Figure 3.1) isopycnals deeper than 500 db are approximately 200 db shallower and up to 0.3°C cooler in fall than summer (Figures 3.4j and 3.4f). In PIB Central (PIB-C, blue, Figure 3.1), adjacent to PIB-NW, isopycnals deeper than 500 db are up to 200 db deeper in fall than in summer (Figure 3.4k), the reverse of the seasonality seen in PIB-NW at the same depths. In PIB South East (PIB-SE, purple,

Figure 3.1), the mixed layer deepens from near-surface in summer to approximately 350 db in winter. Below 500 db, seasonal differences in temperature, salinity and density are minimal.

3.5 Discussion

Across much of the northeastern Amundsen Sea, we find a thicker CDW layer in winter, which contains more heat and more salt, but which is cooler and fresher in winter on the 27.76 isopycnal. Seasonal changes across PIB are not coherent, and are highly variable at spatial scales as small as 20km. A divergence in the depth of the 0°C isotherm and the deeper 27.76 isopycnal as CDW flows south (not shown) suggests that more mixing takes place as CDW flows south, such that CDW in PIB no longer displays the same clear seasonal differences that are observed in the northeastern Amundsen Sea. It is likely that the rotating PIB gyre contributes greatly to this mixing, recirculating and combining CDW that entered the continental shelf at different times.

Thoma *et al.* (2008) and Steig *et al.* (2012) modeled a CDW layer approximately 20 m thicker in winter than summer, between 1980 and 1999 using a coupled ocean - sea ice model with daily mean forcing from the NCEP/NCAR reanalysis. The observed seasonal cycle in CDW layer thickness (thicker in winter) is the reverse of that previously observed in the western trough (Ha *et al.*, 2014; Kim *et al.*, 2017; Wåhlin *et al.*, 2013). This opposite seasonality could be a result of seasonal shift in the main route of CDW inflow between the troughs, raising CDW thickness in the western trough in summer and the eastern trough in winter. Simultaneous mooring arrays spanning all troughs would be necessary to investigate this.

Using an optimized simulation Nakayama *et al.* (2017) find no large seasonal variability in CDW properties at 552 m at the eastern trough shelf break. Although there are insufficient seal tag profiles for seasonal comparison at the shelf break, nearby profiles in the northeastern Amundsen Sea show pronounced seasonal differences (Figure 3.3f), unlike the model. The model of St-Laurent *et al.* (2015) produced a late winter

(August-October) minimum in heat content below 250 m at PIG, which agrees with our observations, although we observe minimum seasonality in the deep core CDW (Figure 3.4d).

The cooler, saltier CDW endpoint in winter in the northeastern Amundsen Sea (Figure 3.3f) is likely the result of a shoaling of winter isopycnals offshelf, such that a denser, cooler and saltier CDW is able to flow onto the continental shelf. This offshelf shoaling would also produce a thicker CDW layer. A denser CDW source water can be of the order of 0.5°C cooler (Wåhlin *et al.*, 2013). If this were to mix with surface waters it might reach the same density as CDW from a less dense, warmer source. Winds can raise the thermocline at the shelf break through Ekman pumping (Dutrieux *et al.*, 2014). Though there are no concurrent moorings offshelf at the eastern trough to corroborate this winter shoaling, an onshelf mooring (unpublished) near to the shelf break does observe a raised thermocline between May and October 2014.

Webber *et al.* (2017) find an interannual variability of temperature of the order of 1°C at 500 db and 0.3°C at 700 db in the area close to PIB. In comparison to this, our seasonal change of 0.32°C in CDW temperatures on the 27.76 isopycnal (at approximately 600 db) over the northeastern Amundsen sea is considerable, although few comparisons are available in PIB. This suggests that the summer-biased historical dataset may misrepresent interannual change and variability of CDW in the Amundsen Sea. Previously, seasonal changes seen at single moorings might have been due to current cores shifting location seasonally across the moorings. Here we demonstrate that coherent changes occur over areas on the scale of approximately 150 km.

The water mass changes observed by the seal tags are inevitably a superposition of seasonal and interannual changes (Webber *et al.*, 2017). With only one year of seal tag data it is not possible to separate these. However the seasonality that we document is consistent with that observed at the moorings in Pine Island Bay (Webber *et al.*, 2017) and with the seasonal cycle in CDW layer thickness in the model results of Steig *et al.* (2012).

A cyclonic gyre in PIB (Thurnherr *et al.*, 2014) is observed in the seal data by Heywood *et al.* (2016). The opposite seasonal changes in CDW thickness between the neighboring PIB-C and PIB-NW regions could be explained by a slowing of this gyre in fall. Such a slowing would reduce the doming of the isopycnals and produce the observed pattern, if PIB-C were at the center of the gyre, and PIB-NW were at the edge of the gyre. An alternative explanation is a lateral movement in the location of the gyre between summer and fall, raising isopynals on one side of the gyre and depressing them on the other. Changes associated with this gyre are likely to be largely responsible for the reduced seasonal differences observed on density surfaces nearer Pine Island Glacier, compared with the northeastern Amundsen Sea, as the gyre recirculates and mixes together CDW that entered onto the continental shelf at different times.

3.6 Conclusions

The warmest CDW of the Amundsen Sea is found in the eastern trough. Throughout most of the eastern Amundsen Sea there is a thicker layer of CDW in winter than in summer, which contains more heat and salt in winter, but which is cooler and fresher in winter on isopycnals. This is particularly prominent in the northeastern Amundsen Sea. This combination of seasonal differences could be the result of shoaling of isopycals offshelf at the eastern trough, allowing a thicker layer of CDW onto the continental shelf, and allowing denser, cooler and saltier CDW access to the shelf, changing the endpoint of the onshelf CDW between winter and summer. This seasonality is much reduced in PIB, likely the result of the recirculating water in the PIB gyre. The observed seasonality in CDW thickness in the northeastern Amundsen Sea is reversed from that seen previously in the western trough (Wåhlin *et al.*, 2013).

The observations presented here enable the first comprehensive analysis of seasonal change in CDW across the eastern Amundsen Sea. This study provides a foundation for future research to separate seasonal variability from interannual variability in this crucial region for understanding and predicting future sea level rise.

3.7 Acknowledgments

We thank the crew and scientists of the RSS James Clark Ross on the iSTAR JR294/295 cruise, the Ocean2ice project team, and Simon Moss (SMRU) for help with seal tagging. The work was funded by the UK Natural Environment Research Council (NERC) iSTAR Programme through grants NE/J005703/1 (Karen Heywood and David Stevens), NE/JOO5649/1 (Mike Fedak), and by the NERC EnvEast Doctoral Training Partnership through grant NE/L002582/1 (Helen Mallett). Lars Boehme was supported by the MASTS pooling initiative (The Marine Alliance for Science and Technology for Scotland) and their support is gratefully acknowledged. MASTS is funded by the Scottish Funding Council (grant reference HR09011) and contributing institutions. The IBCSO bathymetry data are available from https://www.scar.org/science/ibcso/resources/ . The seal tag data are available from http://www.meop.net/ and the British Oceanographic Data Centre, and the ship-based CTD data from the British Oceanographic Data Centre.

3.8 Chapter conclusion

This section was not included in the original paper.

The supplementary figures from the paper are available in Appendix B. Additional sections are available in Appendix C.

In this chapter we use the term CDW, rather than specifying UCDW, LCDW, or mCDW. This choice is made for two reasons: for brevity and simplicity it is the delivery of heat that is the primary question here and because the distinction between LCDW and UCDW source water would distract from the smaller shifts in source water discussed in the paper. We detail carefully the temperature and salinity of the water masses described here to allow easy comparison with other literature, despite this nomenclature choice.

In this chapter we have shown some important seasonal differences in CDW, providing a building block for future study and an important qualifier for models initialised only with summer data, and have answered some of the questions presented in chapter 1 using the corrected, filtered dataset developed in chapter 2. In chapter 4, we continue to utilise this dataset to address further questions raised in chapter 1, this time focussing on the upper ocean.

Chapter 4

Seasonal variability in the upper ocean of the Amundsen sea, using the first comprehensive winter observations available

4.1 Comparison with concurrent mooring data

As discussed in chapter 1, the upper ocean in much of Antarctica is under-observed in winter, largely as a result of the difficult working conditions. In the Amundsen Sea, the seal tag dataset provides the first winter observations of the upper ocean. The seal data provide a valuable opportunity to examine the extent to which observations from the top of moorings can be used to estimate unmeasured conditions in the ocean above. If partial depth moorings were able to indicate conditions in the unobserved water above, then the relative lack of winter upper ocean observations might be considered manageable. However, the seal tag data suggest that partial depth moorings are not well able to indicate upper ocean conditions, then the need for a future focus on obtaining these observations directly is highlighted. A comparison between moorings and seal profiles over depths where both are available also offers a chance to further scrutinise the quality of the seal data, building on the work in chapter 2.

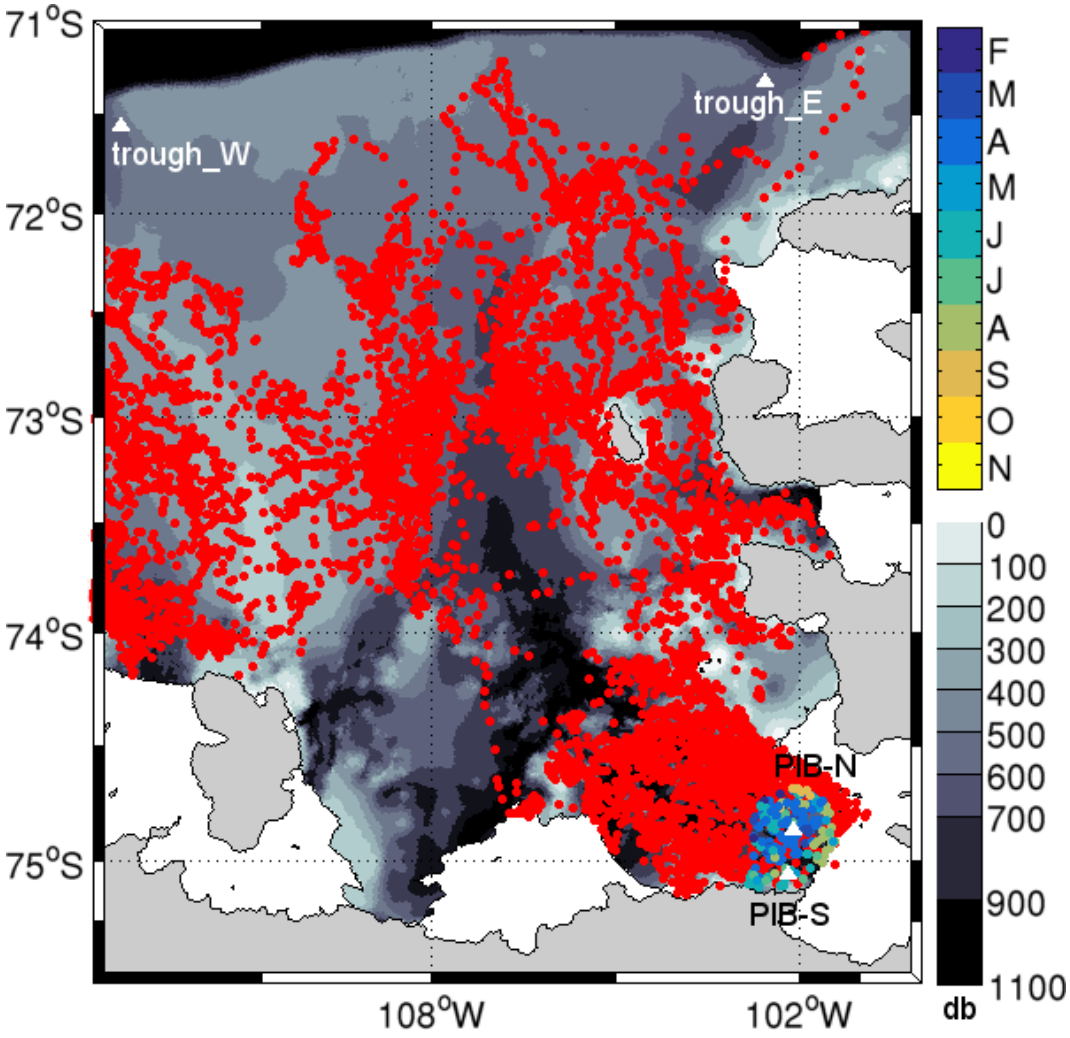

Figure 4.1: Locations of the four moorings (white triangles) and seal profiles (red, and coloured by date where profile is $<$ 20 km from a mooring).

Four moorings were retrieved in February 2016 from the Amundsen Sea, having collected data throughout 2014 (Figure 4.1). Two of these, PIB-N (ISTAR8) and PIB-S (ISTAR9), are close to enough seal profiles to allow comparison between the seal and mooring data. We include in this analysis seal profiles within 20 km of one of these moorings, where the seabed is within 200 m of the seabed at the mooring. It is reasonable here to assume weak currents, so with minimal contribution from relative vorticity, the conservation of potential vorticity constrains flow along lines of constant depth (constant f/H). The proximity and bathymetry restrictions allow a sufficient number of profiles to offer useful comparison with the moorings, while excluding those less likely to be of a similar water mass as that observed by the mooring.

Figure 4.2: Schematic of instrument depths on PIB-S and PIB-N, alongside depths of reported observations from an example seal profile within 5 km of each mooring. Measured is C - conductivity, T - temperature, and P - pressure. Aqualoggers are marked with a square, while MicroCats and seal tags with a circle. Brown lines are seabed depths at moorings.

PIB-S was equipped with Aquatec Aqualoggers measuring temperature and pressure at depths of approximately 263, 399, 468, 537 and 704 m, and unpumped Seabird Electronics SBE37SM MicroCats measuring conductivity, temperature and pressure at approximately 314 and 609 m (Figure 4.2). PIB-N had Aqualoggers at approximately 448, 498, 549, 599, 812 and 896 m, MicroCats at approximately 649 and 936 m (Figure 4.2) (Heywood *et al.*, 2014). The seal profiles are of a higher or equal vertical resolution (depending on dive depth), and reach the surface, although do not always reach the seabed. The moorings have some higher quality instrumentation, have good temporal resolution and endurance, but cannot sample the upper 300 - 500 m, where drifting icebergs can catch moorings and damage instruments or tow the moorings away. The Aqualoggers have an accuracy of ~ 0.05°C for temperature, and the Microcats 0.002°C for temperature and 0.0003 S/m for conductivity. As stated in chapter 2, the seal data have an accuracy of ~ 0.03°C for temperature and ~ 0.05 for salinity (Roquet *et al.*, 2014).

The mooring data at PIB-N show a temporally variable water column, with the 1°C

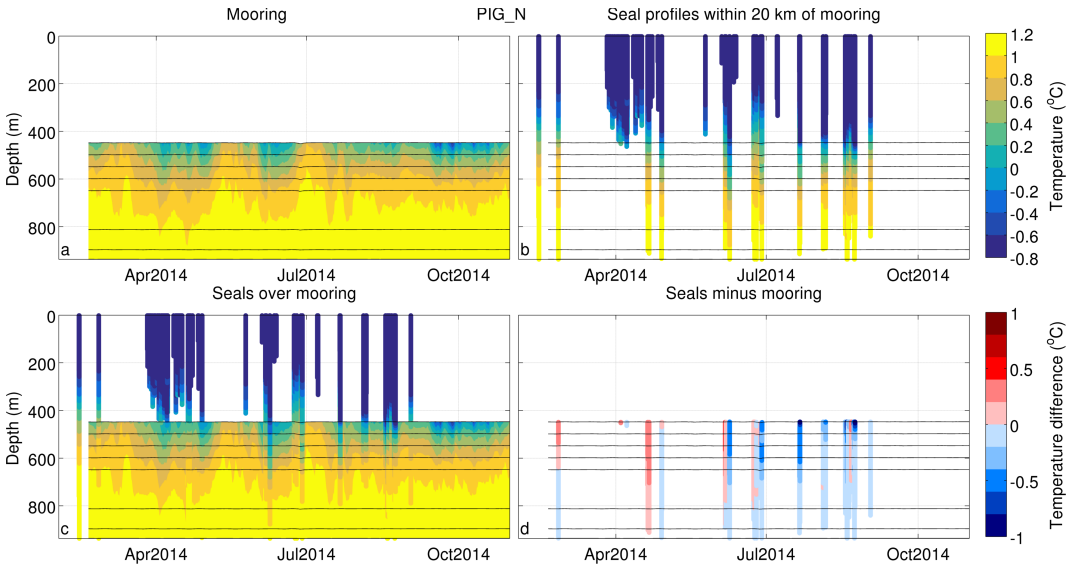

Figure 4.3: Temperature as a function of depth and time for a) the PIB-N mooring, b) the seal data within 20 km of the PIB-N mooring, c) this seal data overlaid on the mooring data, and d) the difference, seal minus mooring, between the two datasets. Blue indicates the seal profile is cooler than the mooring.

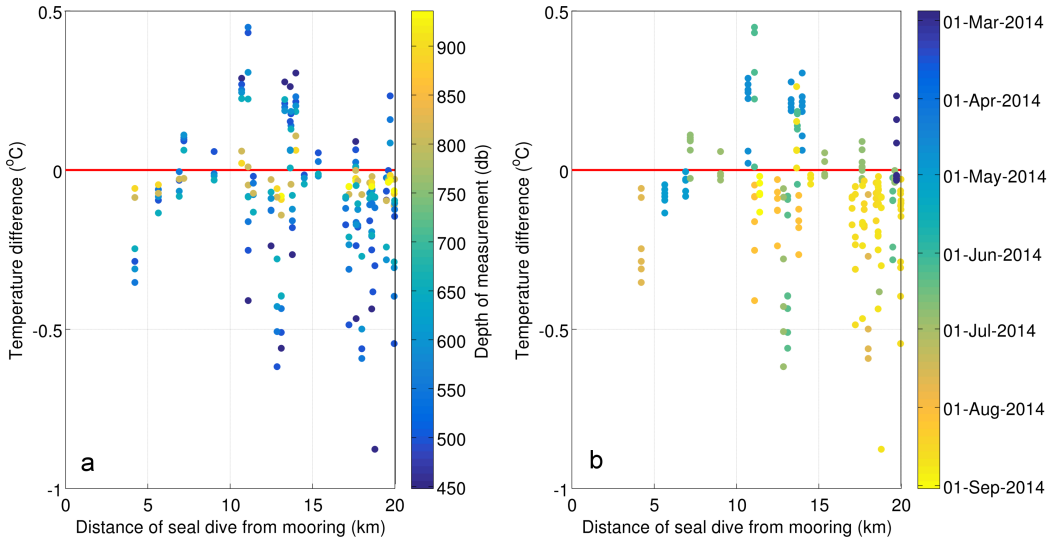

Figure 4.4: Distance of seal profile from PIB-N mooring with difference in temperature between the data sources (seal minus mooring), coloured by a) depth of measurement and b) date of measurement.

isotherm varying between approximately 550 and 870 db through the 9 months (Figure 4.3a). The seal observations have broadly the same properties, with a maximum difference of 1.0°C at 448 db, and a difference of 0.4°C or less below 650 db (Figure 4.3d). These differences between seal tag and mooring temperatures are greater than the sensor accuracies of $\sim$ 0.05°C (Aqualoggers), $\sim$ 0.002°C (MicroCats) and $\sim$ 0.03°C, even combined. However, differences here are expected, as the Rossby radius in PIB is less than 5 km, and so watermasses will vary within the 20 km range at which seal tag profiles

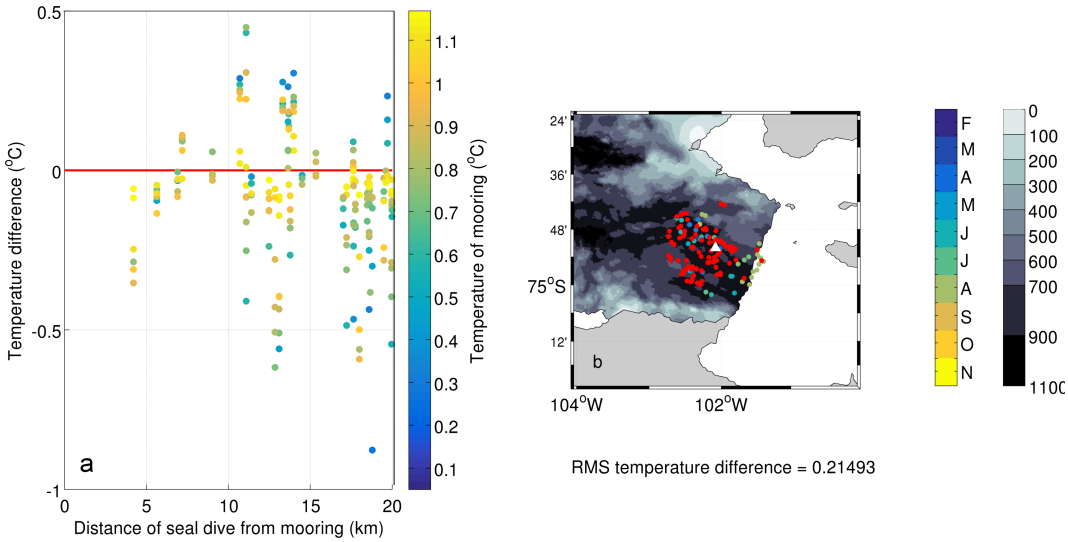

Figure 4.5: Distance of seal profile from PIB-N mooring with difference in temperature between the data sources (seal minus mooring), coloured by a) temperature of measurement. b) locations of PIB-N mooring and seal profiles within 20 km, coloured by date of measurement. Marked in red are profiles where seals did not swim as deep as the top of the mooring.

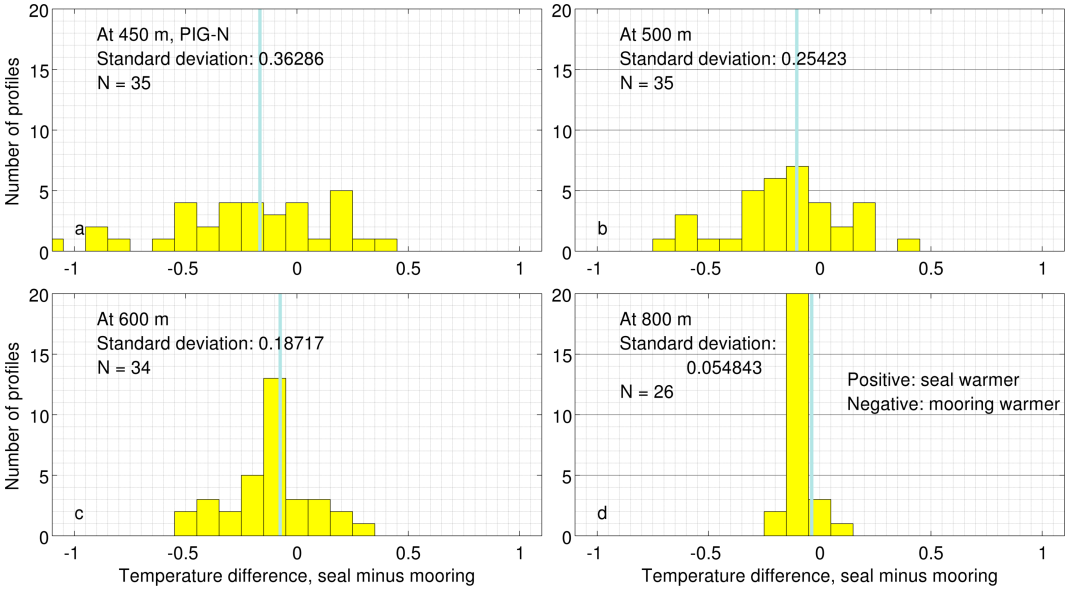

Figure 4.6: Histogram of temperature difference between the data sources (seal tag minus mooring) for the PIB-N mooring and seal profiles within 20 km, at a) 450 m, b) 500 m, c) 600 m and d) 800 m depth. The mean of the temperature difference at each depth is marked by the blue line. The top of the mooring is at 448 m.

are considered co-located with the moorings. There are no sufficiently deep seal profiles close enough to the moorings to be within the Rossby radius, and so this 'co-located' 20 km range is chosen as a compromise between proximity to the mooring and including a sufficient number of seal profiles for a useful comparison.

The seal data are cooler than the mooring data more often than they are warmer (Figure 4.6), with most of these in August and September (Figure 4.4b). This is most likely due to profiles in August and September being located at the PIG terminus and to the north, in shallower water (Figure 4.5b). The temperature differences between seal and mooring are largest in cooler, shallower water (Figures 4.4a and 4.5a), and much more variable in shallower water, with a standard deviation in temperature difference of 0.36°C at 450 m at the top of the mooring, compared to 0.05°C at 800 m depth (Figure 4.6). It is likely that the upper ocean is more variable on small spatial scales than the deep ocean, due to the localised effects of ice cover and atmospheric conditions, so this result is not unexpected.

PIB-S is the shallower of the two moorings (Figure 4.2), with the top of the mooring at 263 m depth. The mooring was towed slightly deeper by an iceberg in late July (Figure 4.7a), with the top of the mooring just below 300 m after this event. It is worth noting that some of the seal profiles used in these comparisons are within 20 km of both moorings, as the moorings are just 21.4 km apart (initial locations). As such, some seal profiles are used in comparisons with both moorings. This is not considered problematic, as sufficient corrections and quality control work were completed in chapter 2 to limit the danger of giving too much weight to a small number of profiles. Had these corrections and quality control work not been done, this comparison between moorings and seal profiles would be much less valuable, as the confidence in single or in small numbers of seal profiles would be greatly reduced.

In April, at PIB-S, some shallow seal profiles are warmer by the mooring by an average of 0.5°C (Figure 4.7d). There are also several seal profiles which are cooler than the mooring by up to 1.4°C at approximately 400 db in mid August. The variability of the temperature differences is much greater at PIB-S (Figure 4.10), with a root mean square temperature difference of 0.53°C (at PIB-N it was 0.21°C), and a standard deviation in temperature difference of 0.71°C at 350 m depth (Figure 4.10a). At PIB-S, the differences between mooring and seal are more evenly spread around zero, with near-zero mean temperature differences at most depths (Figure 4.10). Like at PIB-N, the seal data are more

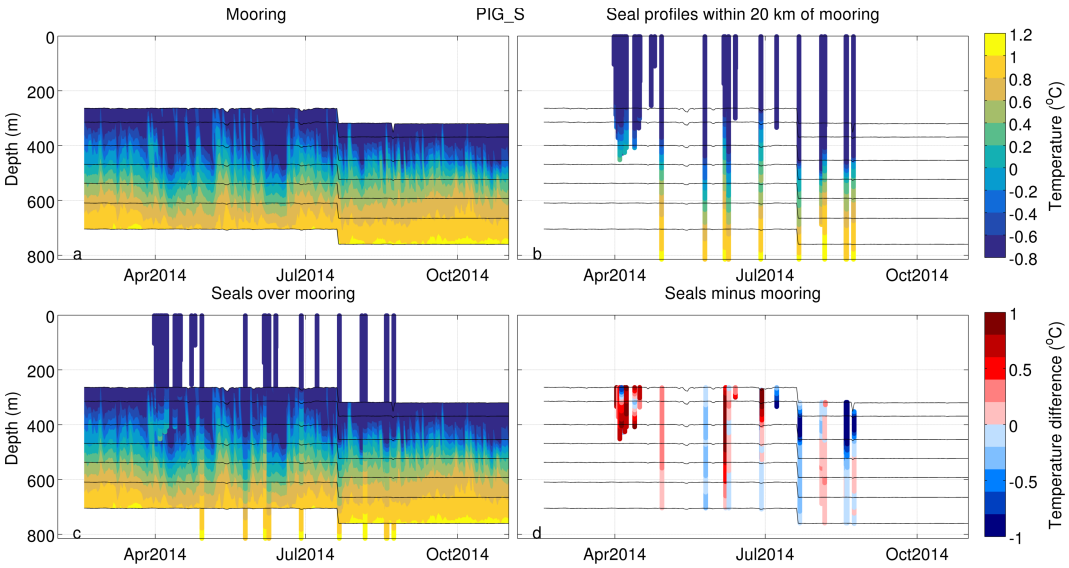

Figure 4.7: Temperature and depth for a) the PIB-S mooring, b) the seal data within 20 km of the PIB-S mooring, c) this seal data overlaid on the mooring data, and d) the difference, seal minus mooring, between the two datasets. Blue indicates the seal profile is cooler than the mooring.

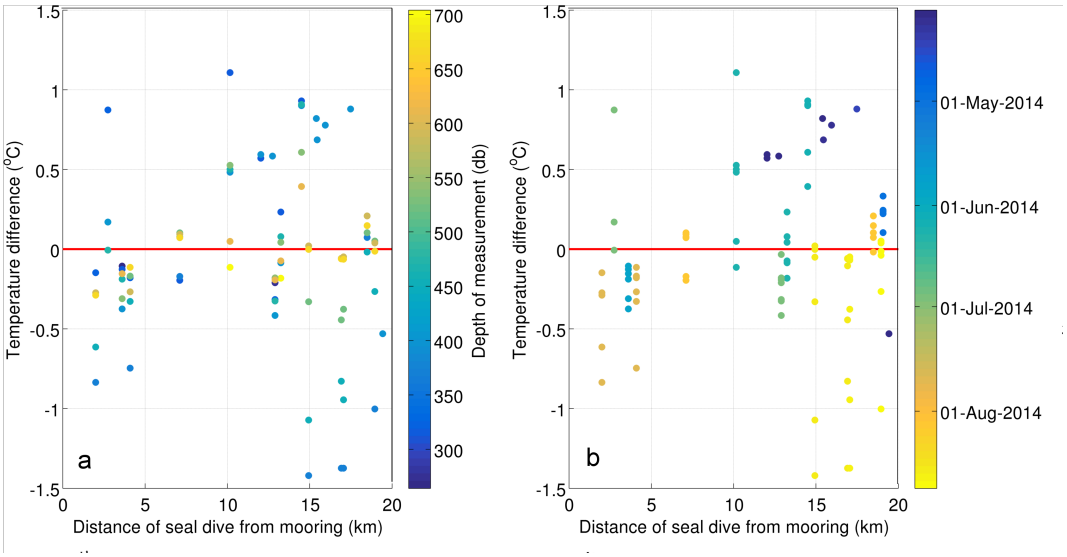

Figure 4.8: Distance of seal profile from PIB-S mooring with difference in temperature between the data sources (seal minus mooring), coloured by a) depth of measurement and b) date of measurement.

often cooler than the mooring in winter, and warmer in summer (Figure 4.8b). Likewise, this is likely the result of a change in seal profile locations within the 20 km radius over time (Figure 4.9b), although these temperature differences are only marginally smaller in those profiles closer to the mooring. Similar to PIB-N these differences are smallest in the deeper, warmer water (Figures 4.8a, 4.5a and 4.10).

These results highlight how localised the observations at a mooring are likely to be,

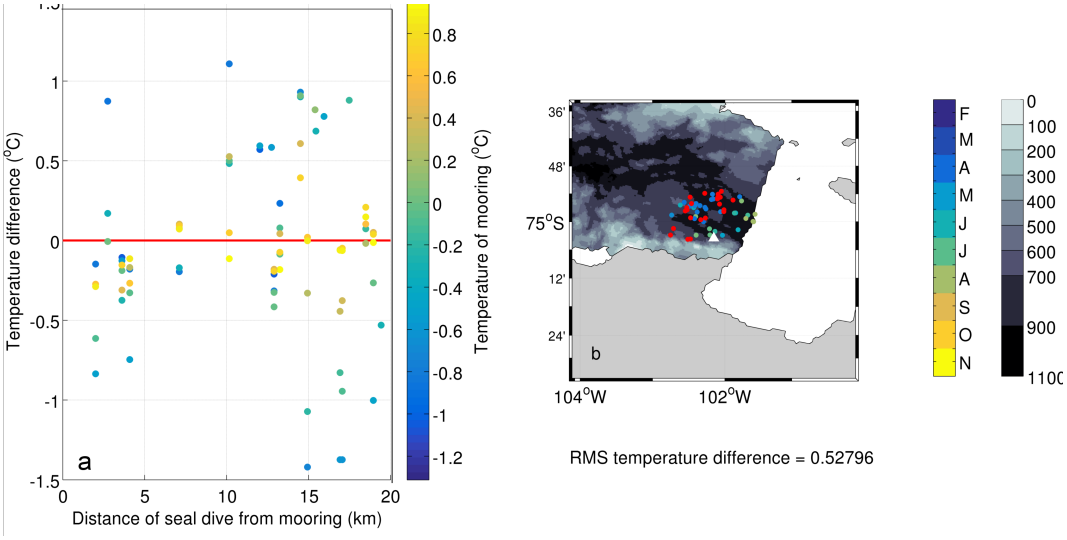

Figure 4.9: Distance of seal profile from PIB-S mooring with difference in temperature between the data sources (seal minus mooring), coloured by a) temperature of measurement. b) locations of PIB-S mooring and seal profiles within 20 km, coloured by date of measurement. Marked in red are profiles where seals did not swim as deep as the top of the mooring.

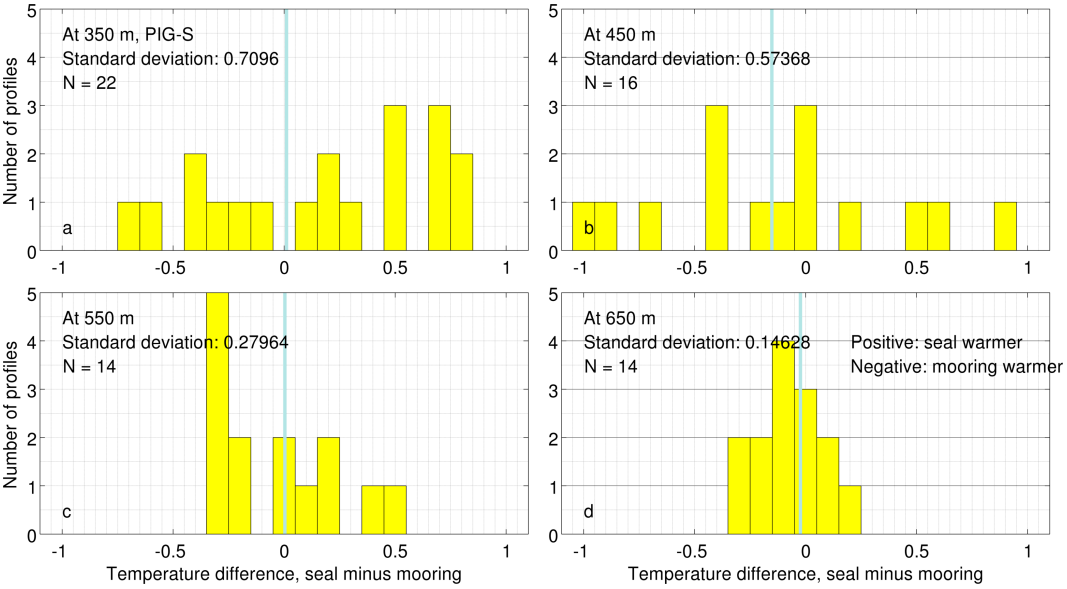

Figure 4.10: Histogram of temperature difference between the data sources (seal tag minus mooring) for the PIB-S mooring and seal profiles within 20 km, at a) 350 m, b) 450 m, c) 550 m and d) 650 m depth. The mean of the temperature difference at each depth is marked by the blue line. The top of the mooring is at 263 m at the beginning of the dataset, dragged down to below 300 m in July.

and reinforces the need for seal tag deployments (which provide a spatial spread of observations) to help quantify spatial variability and to provide a more complete picture of the water masses of the Amundsen Sea than moorings are capable of alone.

In temperature-salinity space, the seal profiles near PIB-N reach greater extremes of

temperature and salinity, but all of these are along the same mixing line, and as such the seal profiles are sampling the same water masses as the mooring (Figure 4.11a). This consistent mixing line observed by both mooring and seal tags also acts to reinforce confidence in the seal tag measurements, despite the aforementioned temperature differences between the observation methods. At PIB-S this is less true - mooring observations are not spread along a clear mixing line, and the seal observations are along a mixing line which passes through the mooring observations, but which also samples much denser water (Figure 4.11b). This is partly because PIB-S is shallower, and observes more of the upper ocean variabiity, and partly because PIB-S is located in an area of steep bathymetry. This steep bathymetry means flow is likely to be more restricted to move along these bathymetry contours than at PIB-N, amplifying the differences between seal profiles and mooring that result from the distance between them. The denser observations are likely from north of PIB-S, nearer the centre of PIB. Despite these differences between observation methods, the seal observations are not of unfeasible water masses, again increasing confidence that these differences are a result of high variability at small (< 20 km) spatial scales, and not of sensor error.

The seal tag dataset provides a useful opportunity to examine the degree to which temperature measured at the top of a mooring can be used to estimate upper ocean conditions, information useful when only mooring data are available. Timeseries of the seal data at the depth of the top of the PIB-N mooring (448 m) and at the surface (red, figure 4.13) show a considerable degree of anti-correlation (Figure 4.14b). At some times (i.e., $\sim$ 6 June) when deep temperatures drop sharply, the surface temperatures rise. This is likely due to bursts of wind-driven mixing, where the very cool uppermost layer mixes with the warmer water just beneath, while the cool mixed layer is deepened (as observed, Figure 4.3a).

In order to find the depths at which temperature and its variability can be estimated by the temperature and variability measured at the top of the mooring, we use the seal observations to find the correlation coefficient between the temperatures measured at the depth of the top of each mooring and at various heights above. If variability at the top of

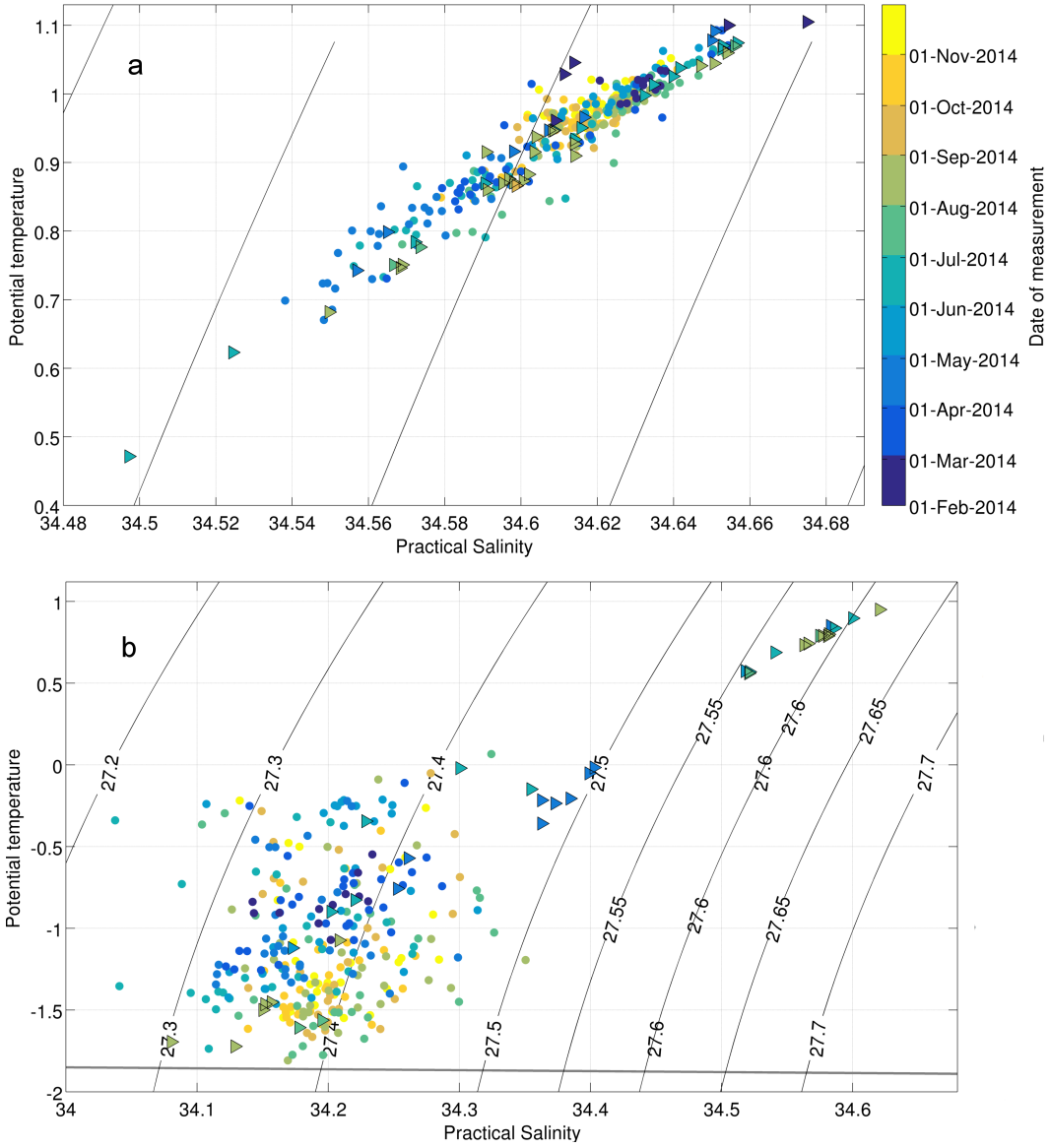

Figure 4.11: Potential temperature and practical salinity of PIB-N (a) and PIB-S (b) mooring observations (circles) and seal profiles interpolated to the depths of the mooring MicroCats (triangles), between February and November 2014, coloured by date of measurement.

the mooring were strongly linked to variability at a particular depth above the mooring, high correlation values would be expected. We expect correlation with the surface to be low, as sun, wind and ice-cover change surface temperatures considerably. At depths close to the top of the mooring, a much stronger correlation is expected.

At PIB-N, temperature at depths close to the top of the mooring is, as expected, highly correlated with temperature at the depth of the top of the mooring (Figure 4.12. This is seen in the timeseries (green, figure 4.13) and correlation plot (Figure 4.14a) 200 m above

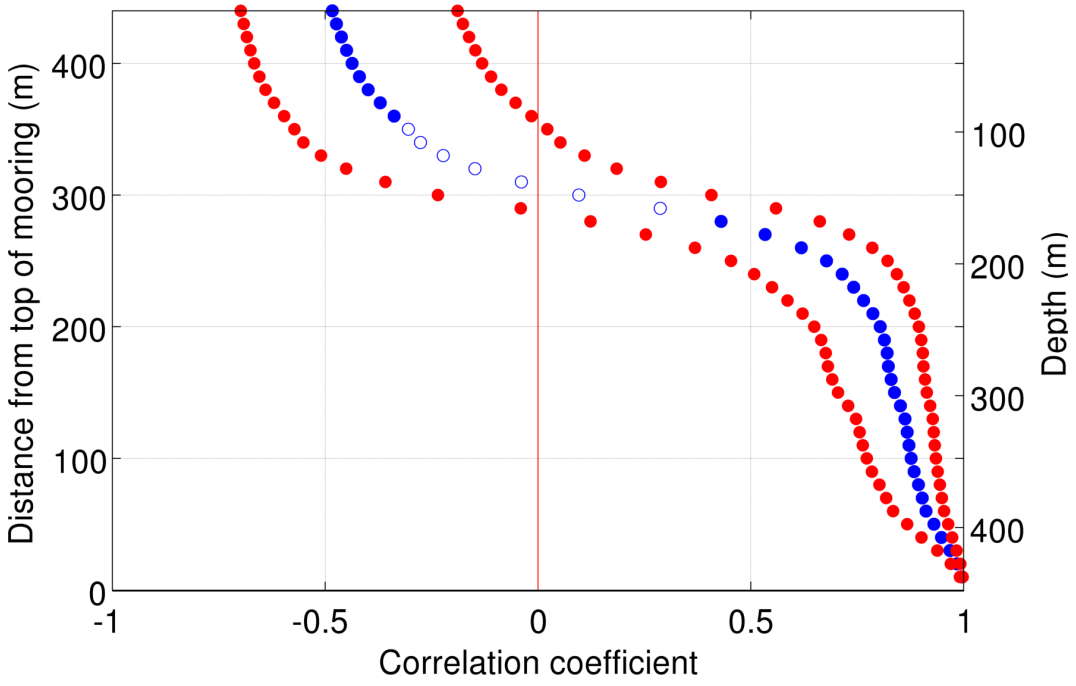

Figure 4.12: The correlation coefficient between temperature at the depth of the top of the PIB-N mooring, and the temperature at varying distances above, all from co-located seal profiles. True depth on right y-axis. Correlation coefficients are in blue circles, which are empty where the coefficient is not significant at the p=0.05 level. The red dots mark the upper and lower bounds for a 95% confidence interval for the coefficient at each depth level.

the top of the mooring, with a correlation coefficient of 0.8. This extends 230 m upwards from the top of the mooring (up to 218 m true depth). At distances greater than 230 m above the mooring top, correlation rapidly decreases. In the upper $\sim$ 90 m an anti-correlation is observed, as discussed above.

At PIB-S, there is an anti-correlation of -0.5 at the surface (Figure 4.15), which, as for PIB-N, may come from short bursts of mixing, some of which are at the same times as those seen at PIB-N (i.e. early June, red, figure 4.16 and figure 4.7a). This is not unexpected, given the close proximity of the moorings, and the overlap of seal profiles considered co-located with each (figure 4.2). The layer of high correlation above the top of the mooring is thinner at PIB-S (to 110 m above the mooring top) than at PIB-N (to 230 m above the mooring top), but this is in part because PIB-S is a shallower mooring and it's top is closer to the more variable surface waters (Figure 4.2). The poorly or anti correlated layer at the surface extends down to 220 m (true depth, PIB-N, figure 4.12) or 150 m (PIB-S, figure 4.15). The difference between the two moorings in the thickness of this anti / poorly correlated layer indicates that conditions (ice cover, wind, MLD, local

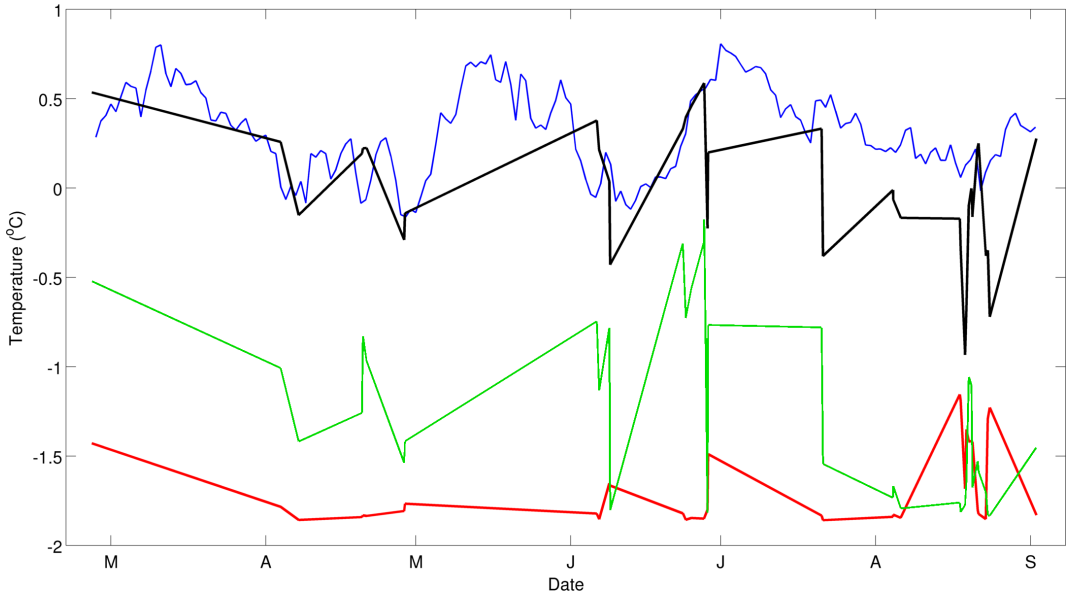

Figure 4.13: At PIB-N, for each co-located (within 20 km of mooring) seal profile which is sufficiently deep, the temperature at the depth of the top of the mooring (black, 448 m), and the temperature 400 m (red) above and 200 m (green) above. In blue is the temperature at the top of the mooring, as measured by the mooring, for the same period.

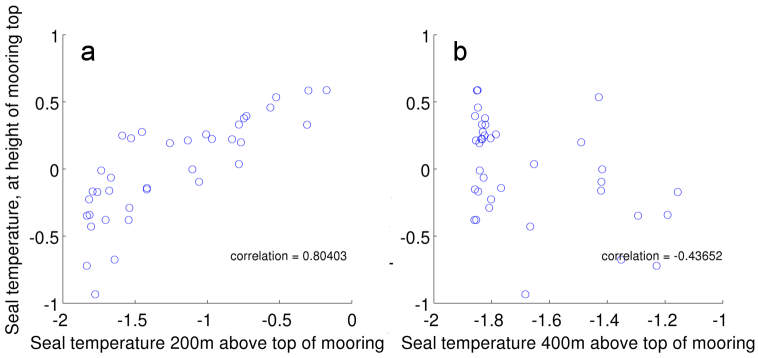

Figure 4.14: At PIB-N, for each co-located seal profile, the temperature at the depth of the top of the mooring (y-axis), against the temperature, 200 m (a) and 400 m (b) above (x-axis).

flow, etc.) at the two locations are sufficiently distinct to necessitate this separate analysis at each mooring location, rather than considering them together, or considering the whole of the Amundsen Sea at once.

Temperature and its variability at the top a mooring is well correlated for a layer above the mooring approximately 110 to 230 m thick. Above this, other processes such as surface layer mixing are stronger and mooring temperatures are not a good indicator. Although temperatures at the very surface are anti-correlated to those at the top of the moorings, the anti-correlation values are not high enough to be of great use (Figure 4.17).

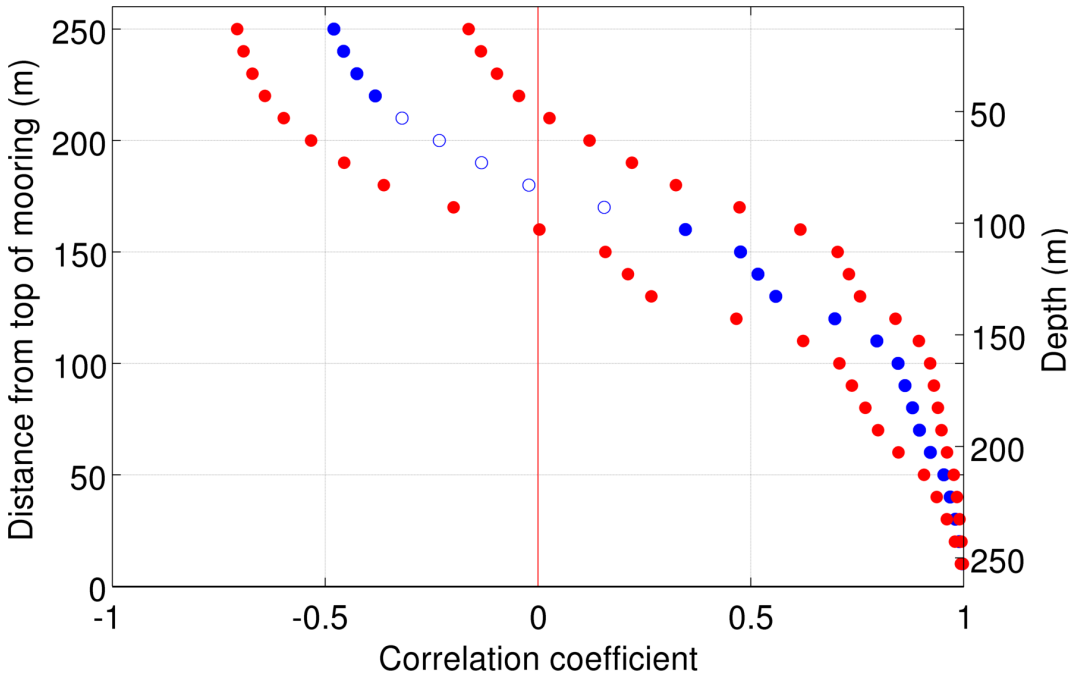

Figure 4.15: As in figure 4.12, but for PIB-S.

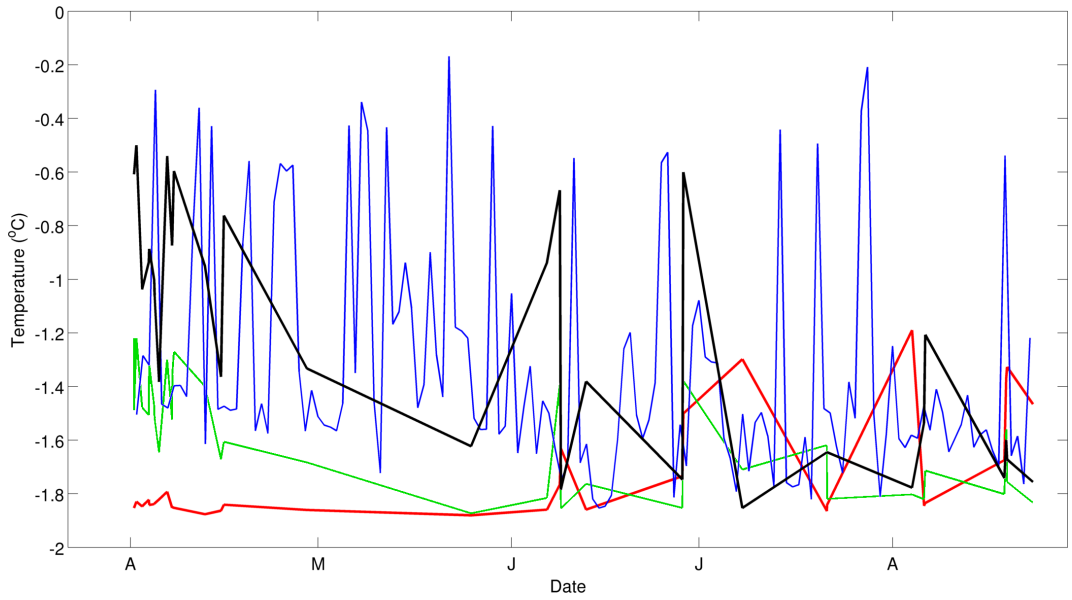

Figure 4.16: At PIB-S, for each co-located seal profile, the temperature at the depth of the top of the mooring (black, 263 m), and the temperature 250 m (red) above and 100 m (green) above. In blue is the temperature at the top of the mooring, as measured by the mooring, for the same period.

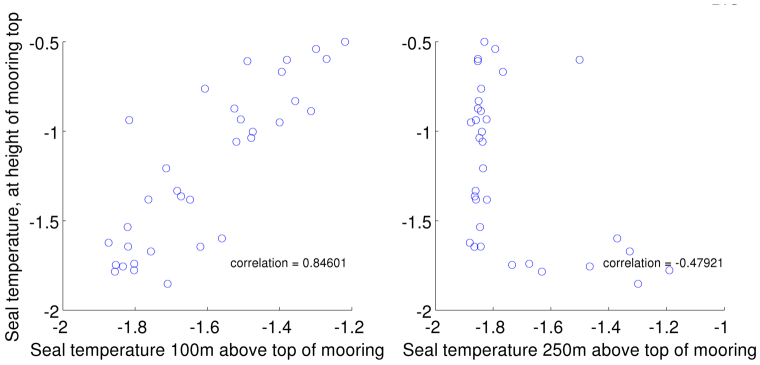

Figure 4.17: At PIB-S, for each co-located seal profile, the temperature at the depth of the top of the mooring (y-axis), against the temperature, 100 m (a) and 250 m (b) above (x-axis).

4.2 Surface waters in the Amundsen Sea

In chapter 3 a thorough examination of seasonal variation in CDW was presented. In the following section, this is extended into the upper ocean, using the first comprehensive observations available of the upper ocean in winter in the Amundsen Sea.

4.2.1 Overview

Air-sea interactions are thought to play a pivotal role in the heat content of water flowing toward the ice shelves, in the mixed layer. This is particularly true in polynyas, where persistent openings in sea ice allow winter atmospheric conditions to influence the mixed layer throughout the winter season, deepening the thermocline, cooling the surface and driving sea ice formation and associated brine rejection. Ocean processes near ice shelves are particularly important, and particularly hard to measure.

The abundance of profiles is one of the most valuable features of this dataset, and even at 300 m, a depth within reach of (some) moorings, the seal tag dataset provides an order of magnitude more information than previous historical data, in a fraction of the time period (Figure 4.18). From these numerous profiles a much more comprehensive picture of conditions is built, and this can be used in the analysis of both deep water (as in chapter 3) and shallow water, where such data has never before been available in winter. This abundance is utilised to examine seasonal variation in conditions at and near the glacier termini.

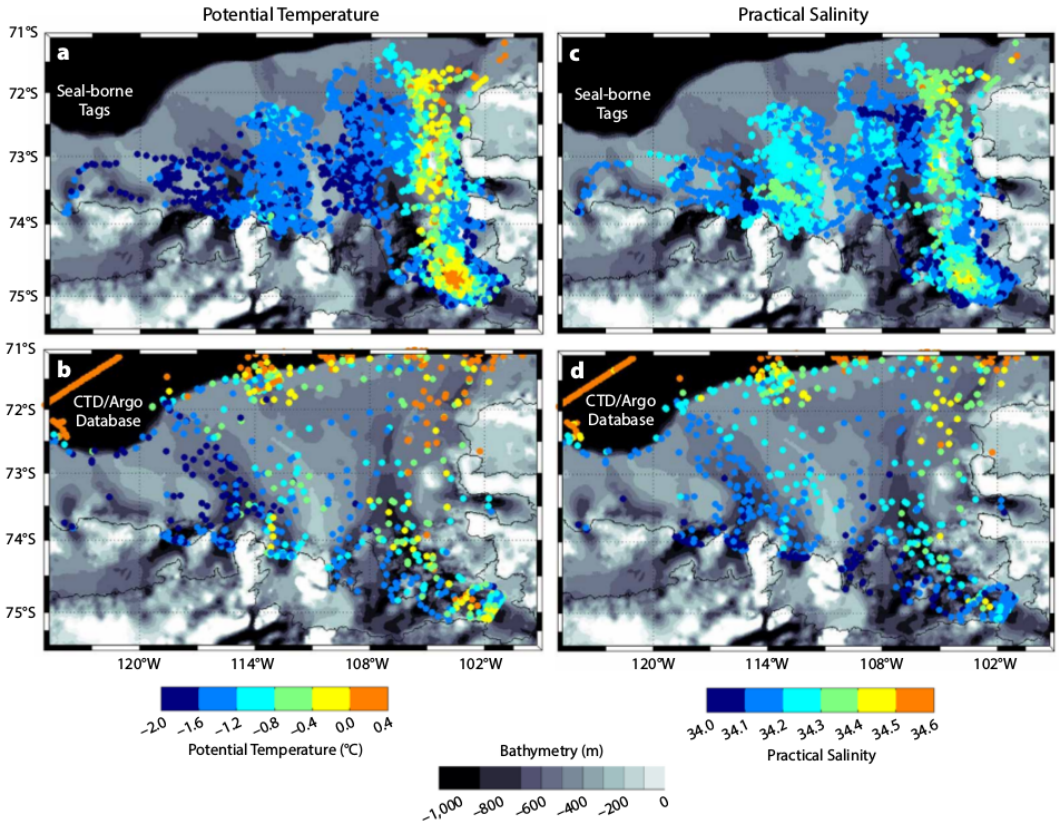

Figure 4.18: Measurements at 300 m of potential temperature (a,b) and practical salinity (c,d) from seal-borne CTD tags during 2014 (a,c) and from historical CTD and Argo float data between 1994 and 2014 (b,d). Figure from Heywood *et al.* (2016). Figure not adapted, as it is the authors work.

First, a timeseries of all the seal profiles on the continental shelf (figure 4.19) shows that from the beginning of the dataset in February the mixed layer depth deepens from less than 25 db to greater than 50 by the end of March. This deepening is accompanied by a cooling and a salinification of that mixed layer. Throughout the whole period, from February to October, the upper 300 db gets cooler and saltier. This is as expected - cold atmospheric temperatures in winter cool the ocean surface where exposed, driving sea ice production which in turn increases salinity in the upper ocean through brine rejection. It is unprecedented to have observations able to confirm this.

Here three regions where sufficient seal profiles are available through the seasons are investigated. These are at or near glacier fronts - at Thwaites, between Getz and Dotson, and in PIB, and at the PIG front.

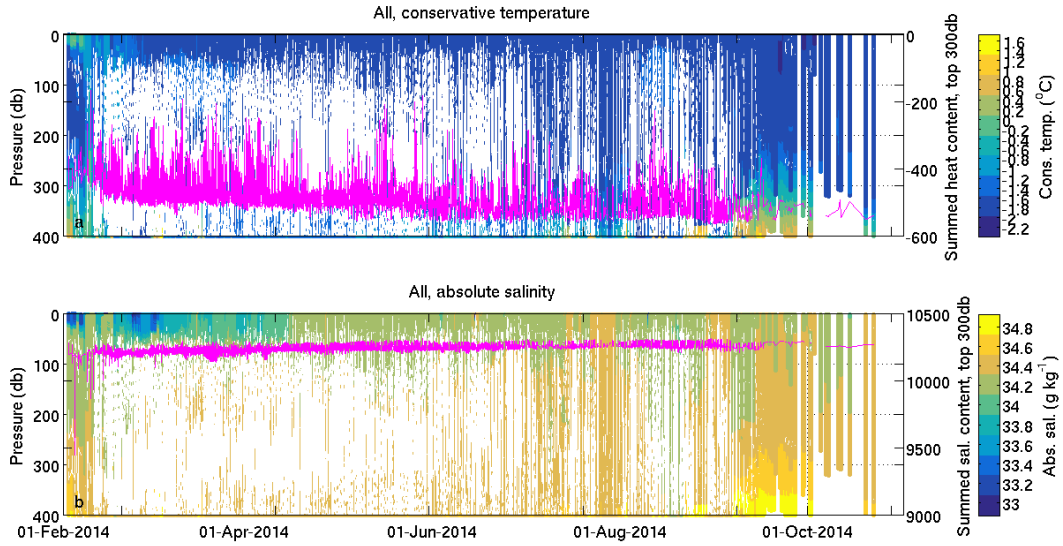

Figure 4.19: Time series of whole of Amundsen Sea (all seal tag profiles on the continental shelf in 2014). a) coloured by conservative temperature and b) by absolute salinity. Overlaid are lines of constant potential density anomaly (white) at 27.4, 27.5 and 27.6 kg/m^3, and a proxy for heat content (pink). This proxy is a sum of conservative temperature for every 1 db of a profile, between 0 and 300 db (a, pink) and the equivalent for salt content and absolute salinity (b, pink).

4.2.2 Thwaites Glacier

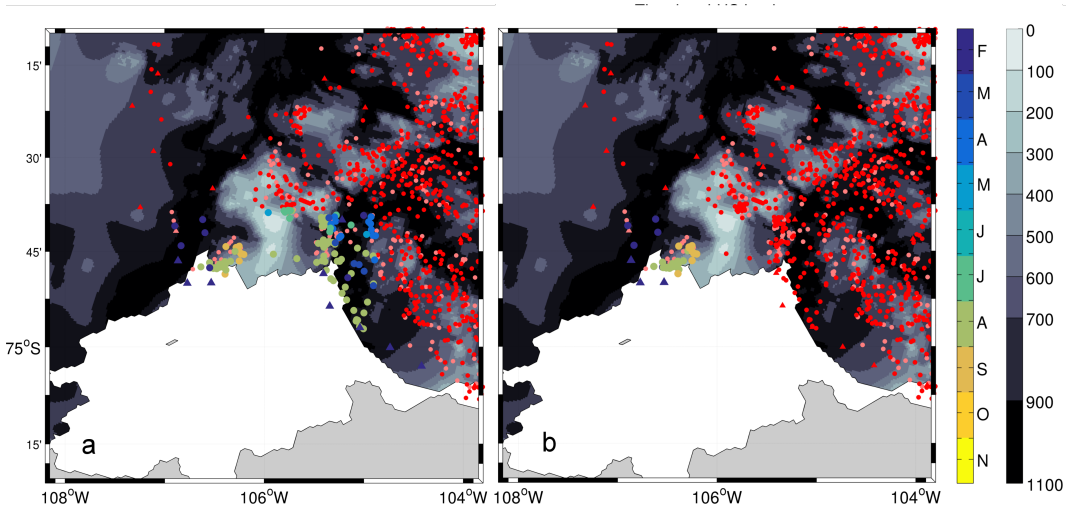

Figure 4.20: a) locations of profiles near Thwaites glacier. Coloured by date are the profiles used in the analysis, with seal data (circles) and ship-CTDs (triangles). Also plotted are locations of seal profiles outside the region (red) and locations of seal profiles failing quality control (pink, not included in analysis). b) as in a), but for the western profiles only

Thwaites, like PIG, is rapidly loosing mass (Rignot *et al.*, 2008), but fewer moorings and studies have focused on this ice shelf. Here timeseries and TS diagrams for seal profiles close to the ice shelf are presented. At Thwaites glacier (Figure 4.20a) there are data from both winter and summer, either side of a north-south bathymetric ridge. This ridge

is expected to mark a divide between water masses recirculating in PIB and those flowing south to the west of Thwaites. To evaluate this we also separate out the western half of the Thwaites region (Thwaites-W, figure 4.20b). A distinct seasonal divide is seen (Figure 4.21), where surface water, winter water, and the CDW endpoint are all colder and saltier in winter. This is consistent either side of this ridge (Figure 4.22), although observations on the eastern side of Thwaites, in PIB, show some cooler winter water than those on the western side, in August (winter, not shown). This is likely the result of a polynya enabling more cooling and ice formation and the brine rejection leading to a deeper mixed layer in PIB.

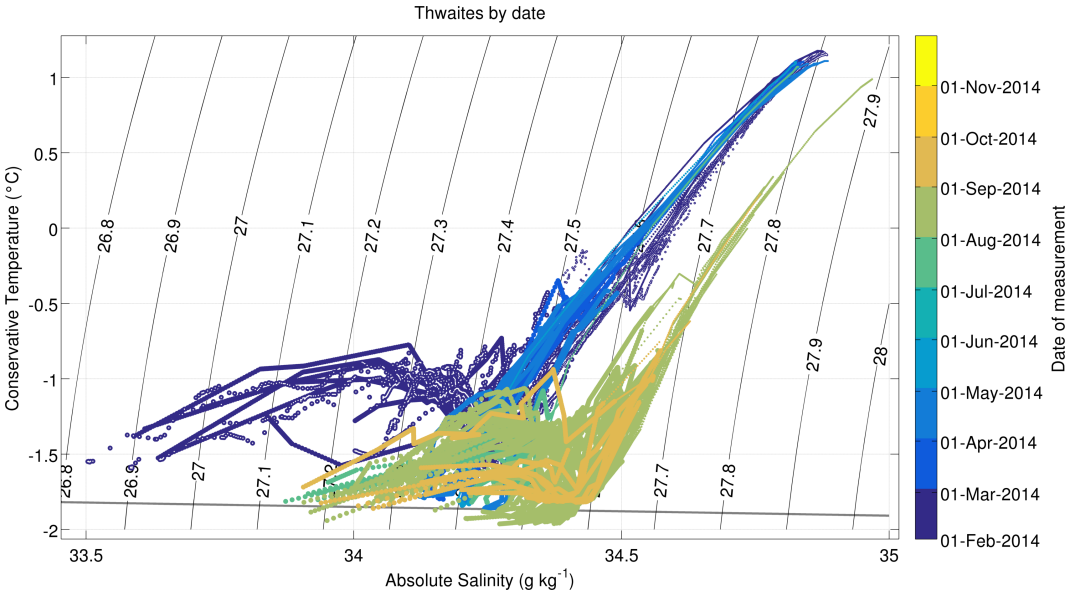

Figure 4.21: Seal profiles by absolute salinty and conservative temperature, coloured by date. Ship-CTD data are included, coloured with a white centre. Later observations are plotted over older. All data deeper than 400 m are plotted smaller/thinner. Behind in black are the freezing line (straight) and lines of potential density (curved).

A timeseries at Thwaites (Figure 4.23) shows the salinification of the surface waters through the year, with the salt content increasing from summer to winter due to brine rejection associated with sea ice formation. In August the difference between the eastern and western sides of Thwaites is more clearly visible (Figure 4.24), with much cooler, saltier observations on the eastern side, in PIB.

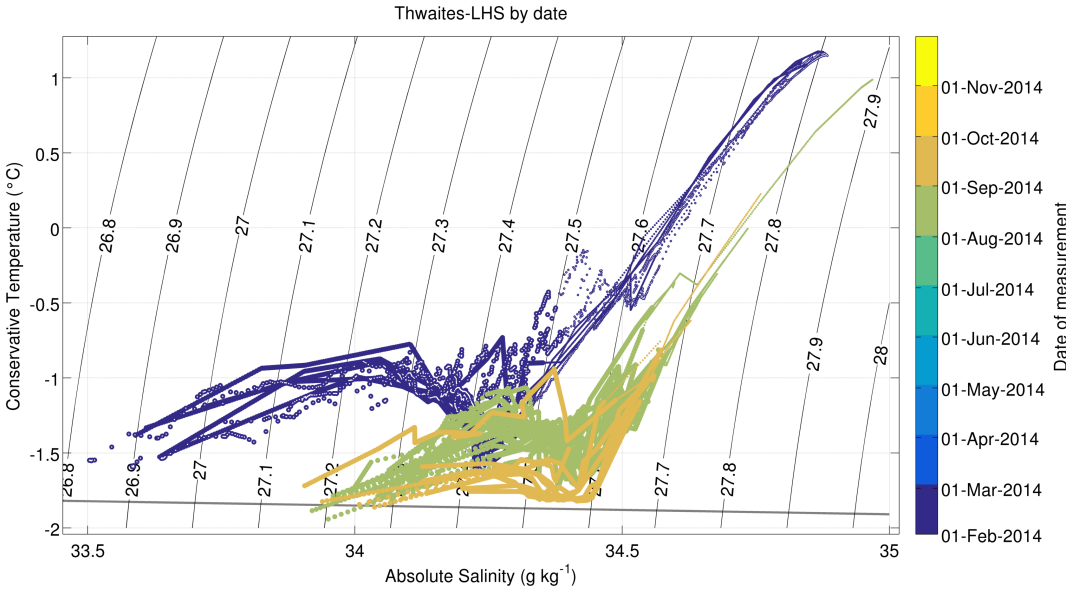

Figure 4.22: As in figure 4.21, but for the western profiles only.

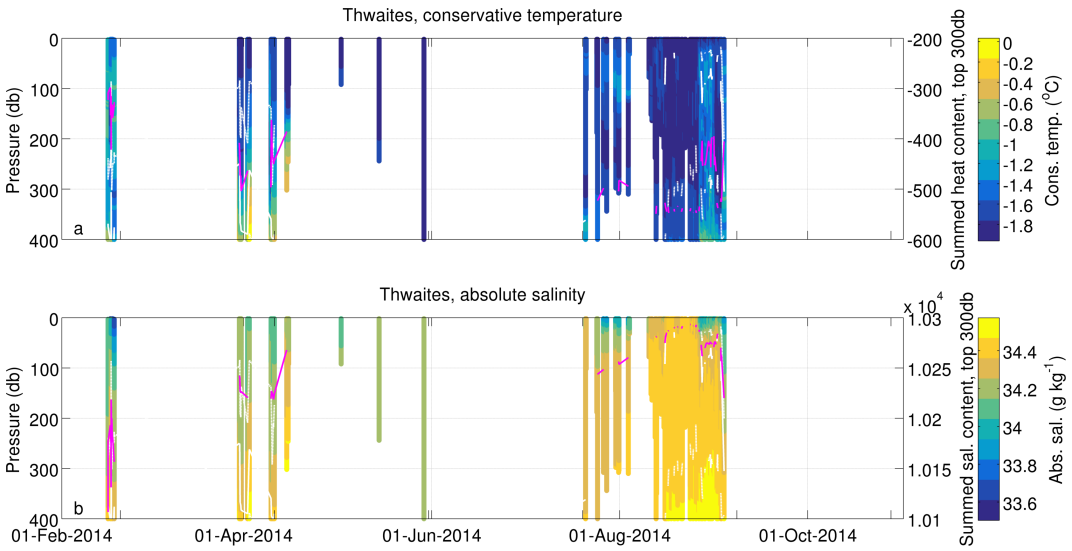

Figure 4.23: Timeseries for the Thwaites region coloured by a) conservative temperature and b) absolute salinty. Overlaid are lines of constant potential density anomaly (white), at 27.4 (dotted, shallowest), 27.5 (solid) and 27.6 kg/m^3 (dotted, deepest). Also overlaid is a proxy for heat content, where conservative temperature at every 1 db is summed, from 1 to 300 db (a, pink) and the equivalent for salt content in absolute salinity (b, pink).

4.2.3 Getz and Dotson Glaciers

Between Getz and Dotson (Figure 4.25) there are 574 profiles, well spread between mid March and mid September, collected around the peninsula (Figure 4.25). Two female Southern Elephant seals and one female Weddell seal swam to Getz, and sampled heavily at depths between 400 and 700 db where there is presumably an optimal food source.

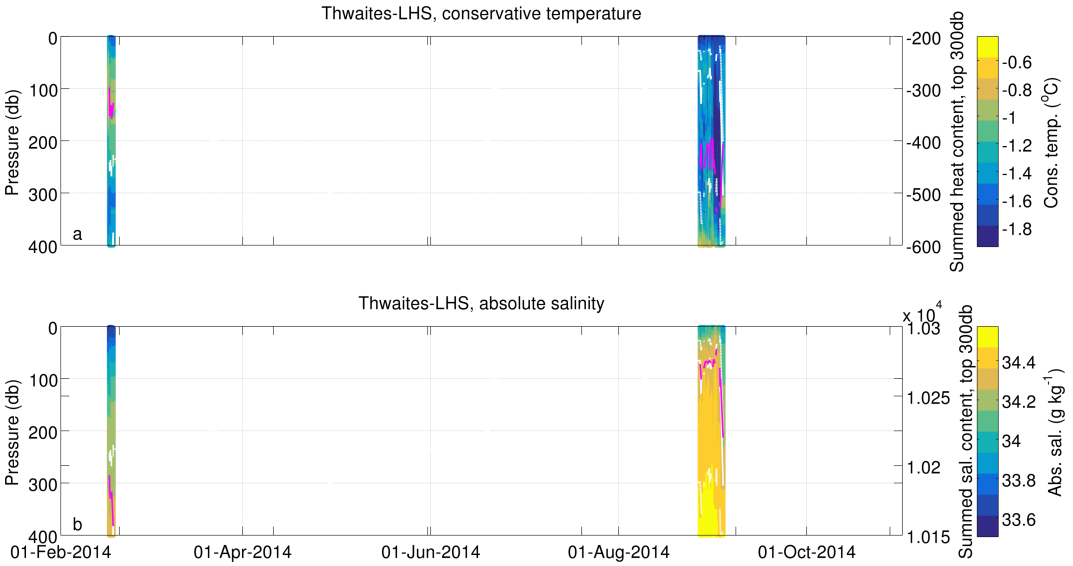

Figure 4.24: As in figure 4.23, but for the western profiles only.

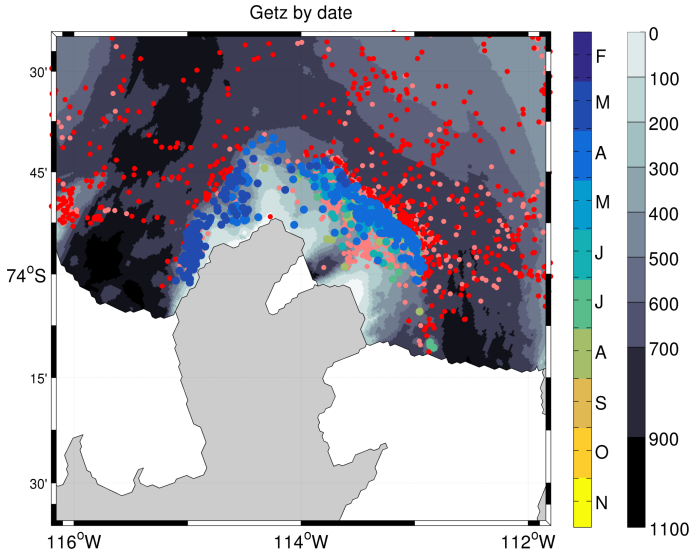

Figure 4.25: As in figure 4.20, but for Getz, and including only profiles within a 500 m depth band on slope of the coast bathymetry. Getz ice shelf is to the west, on the left hand side, Dotson ice shelf is to the east, on the right hand side.

The water masses on either side of the peninsula, near to Getz (west) or near to Dotson (east) are very different. Those west of 114°W show an abundance of cold (< -0.5°C) and very fresh (< 34.3 g/kg) surface water (Figure 4.26), in summer (Figure 4.27). These cold, fresh observations, measured along the western boundary of the peninsula (Figure 4.25), must be a result of melting, either from icebergs and sea ice, or from the ice shelf. East of 114°W observations suggest the water column at the western edge of Dotson is a straightforward mix between mCDW and Winter Water (WW). These observations range from April to August, and observations toward winter have a WW end-point which is

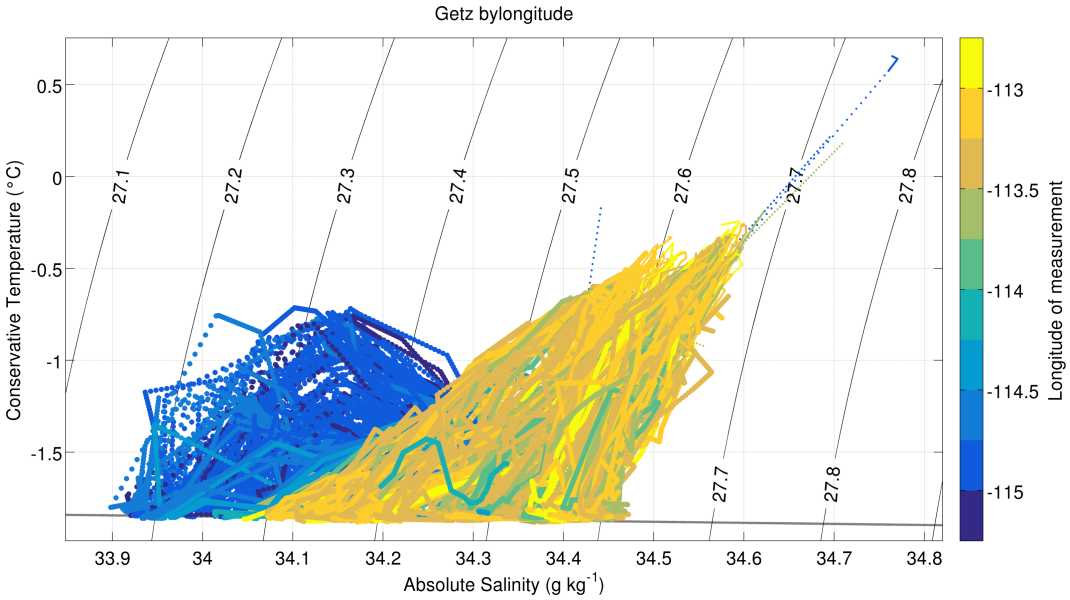

Figure 4.26: As in figure 4.21, but for Getz, coloured by longitude, and including only profiles within a 500 m depth band on slope of the coast bathymetry.

much saltier (Figure 4.27), likely a result of brine rejection from sea ice formation.

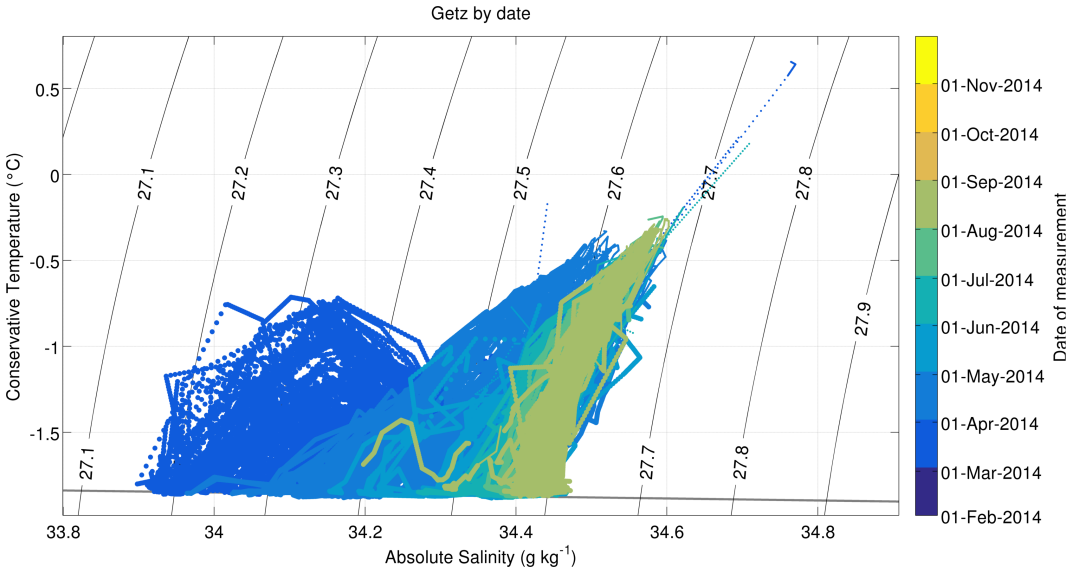

Figure 4.27: As in figure 4.21, but for Getz.

The mixed layer depth is approximately 100 m in mid March, rapidly deepening to a maximum of approximately 350 m in June, before rising again to approximately 250 m in mid September (Figure 4.28), presumably as ice-cover forms and protects the ocean surface from the wind and atmospheric influence.

In the latter half of March, west of 114°W (near Getz) at approximately 100 - 150 db, just below the mixed layer, a thin layer of warmer water (up to -0.7°C) is observed, with cooler water above and below it (Figure 4.28). This signal is sustained and observed by > 30 profiles, and so is not likely to be an error in the data. The water beneath is saltier, to a sufficient extent that the water column is still density stratified. One possible explanation is that buoyant fresh cold ice melt from beneath Getz rises, mixing as it passes with the saltier, warmer mCDW and rising until it meets the underside of the very cold, very fresh surface layer.

The winter salinification from brine rejection is particularly clear here, with a consistent increase in salinity in the upper 100 m between the end of March and the middle of May, from approximately 34.15 g/kg to approximately 34.4 g/kg.

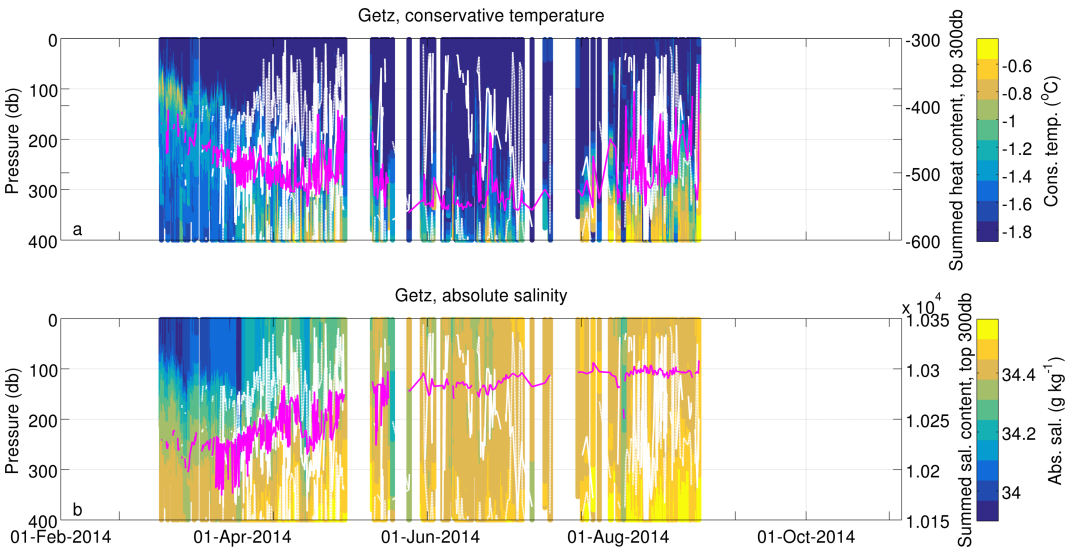

Figure 4.28: As in figure 4.23, but for Getz.

A basic estimate of the necessary conditions to produce such changes in the mixed layer is undertaken. This will focus on the Getz/Dotson area, where a timeseries with interesting fluctuations in upper ocean heat and salt content is observed (Figure 4.28). At 114°W, 73.75°S, in the centre of the Getz region used to produce Figure 4.28, sensible latent heat transfer away from the ocean surface increases gradually from February to mid April, though with high temporal variability (Figure 4.29). Sea ice concentration increases sharply from the beginning of March, though barely exceeds 80% until mid June

(Figure 4.29). The period beginning in April to mid May has a greater sea ice concentration than before or for the following month. The expectation is that this sensible heat flux, when combined with limited sea ice cover, would increase sea ice production, increasing salinity in the upper ocean below. It appears here that the greater sea ice concentrations seen between the beginning of April and mid May may be a result of increased sea ice production instead, as the salinity in the surface water beneath rises steadily through this period.

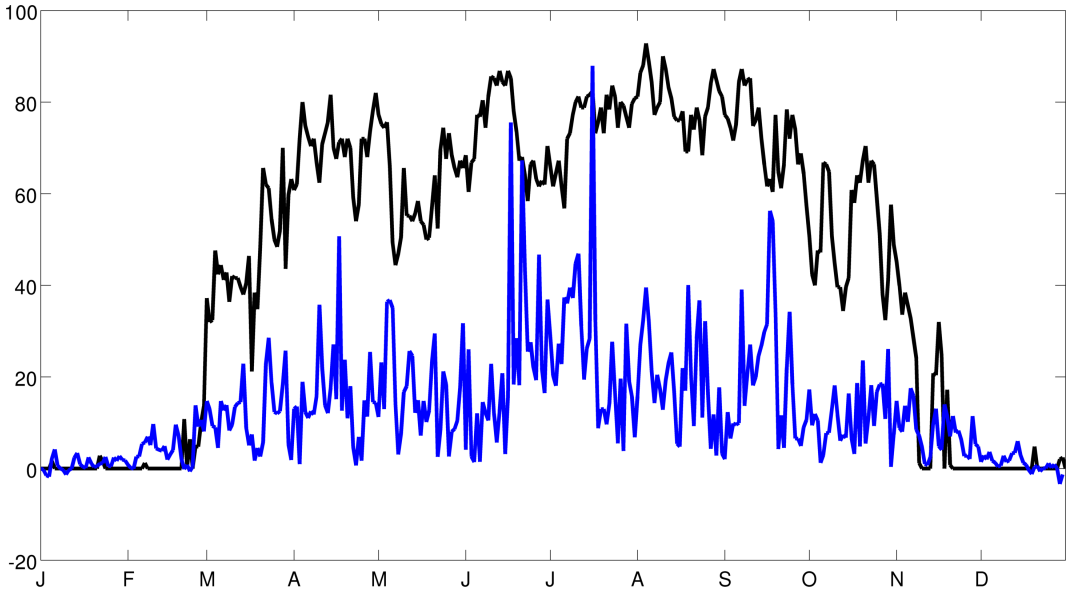

Figure 4.29: Sea ice concentration through 2014 (black), from Nimbus-7 SMMR and DMSP SSM/I-SSMIS Passive Microwave Data (Cavalieri et al., 1996), and sensible heat flux (blue, x100), calculated using ERA-Interim reanalysis data (Dee *et al.*, 2011), both at 114°W, 73.75°S.

4.2.4 Pine Island Glacier

For profiles in PIB, where bathymetry is between 200 and 600 db, there are 610 profiles, spread between February and September. The shallow bathymetry is excluded so that the analysis does not include multiple water massses, but as a result the profiles are likely to be contained within the PIB gyre, and thus observe water masses constantly recirculating and mixing with each other, minimising seasonality that may be more prevalent elsewhere. The PIB gyre is clearly visible in seal tag data in a figure previously published by Heywood et al. (2016, figure 4.18a,c).

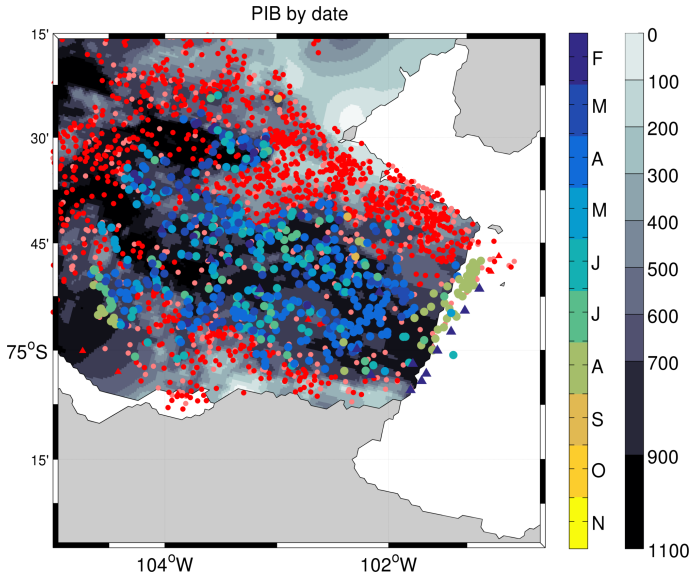

Figure 4.30: As in figure 4.20, but for the profiles in PIB where bathymetry is between 200 and 600 db.

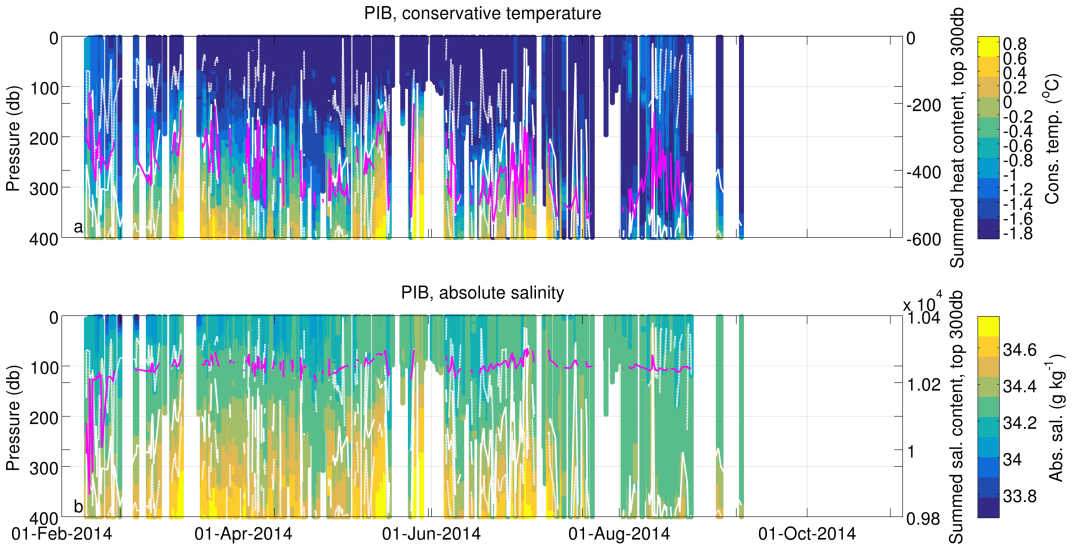

Figure 4.31: As in figure 4.23, but for PIB.

A timeseries of temperature and salinity reveals (Figure 4.31) salt content in the upper 300 m varies a similar amount between the end of February and the end of August as in other locations (Figure 4.31b). There are also coherent changes in the deep isotherms, where the warmer water rises and falls (mid March, late May, beginning of July). This is likely a result of local wind forcing causing doming of the isopycnals and isotherms of the gyre as it speeds up and slows down (Figure 4.32).

At PIG (Figure 4.33) summer salinities appear well stratified, with temperatures in the upper 400 m often greater than some at observation below. In winter, when the most high

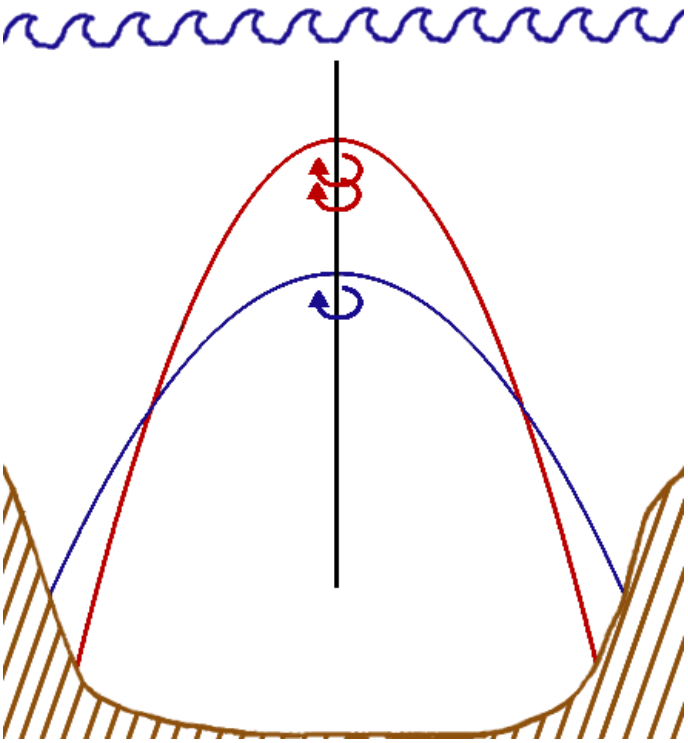

Figure 4.32: Schematic of the doming of isopycnals that might result from a faster circulating gyre. The red line represents an isopycnal in a faster rotating gyre, while the blue line represents the same isopycnal in a slower rotating gyre.

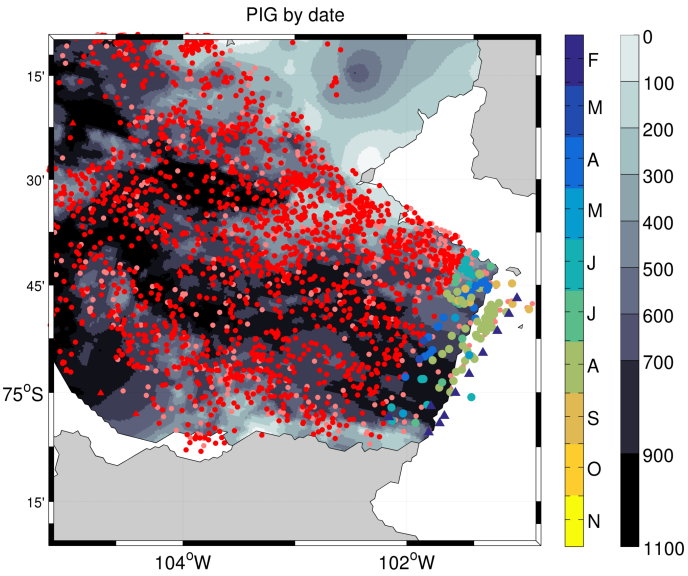

Figure 4.33: As in figure 4.20, but for PIG.

resolution section is available, we see a very uniform mixed layer depth of approximately 400 db along the section, with a few spots of higher temperatures above this mixed layer (Figure 4.34c).

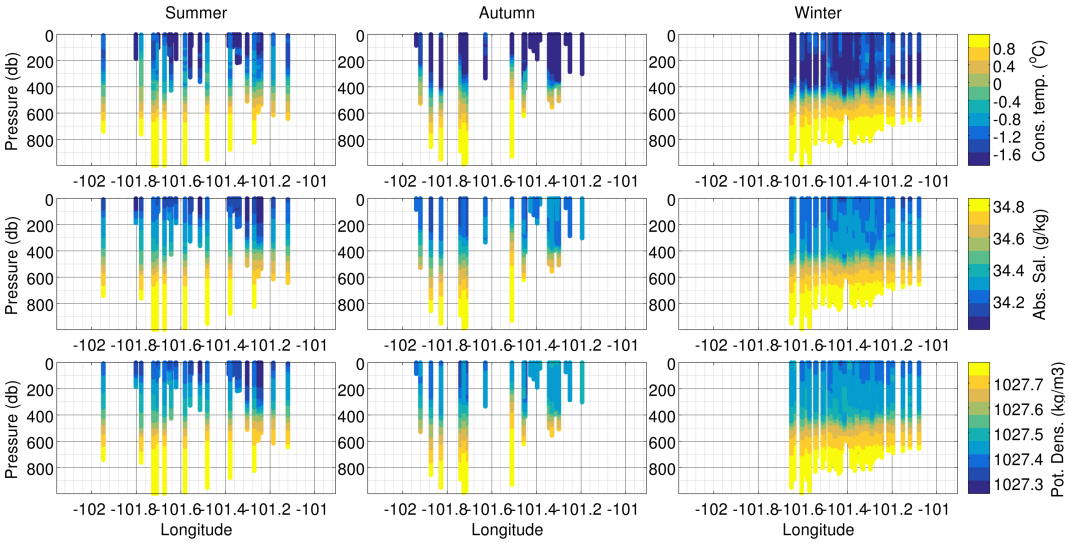

Figure 4.34: Sections along PIG, profiles projected perpendicular to ice front. Summer (left), autumn (middle) and winter (right) sections for conservative temperature (top), absolute salinity (middle) and potential density (bottom).

4.3 Summary

With the aid of some co-located moorings, the seal tag dataset carefully corrected in chapter 2 is checked once more against more traditional observation techniques. Although differences in temperature between the two are present, the comparisons in temperature-salinity space (Figure 4.11) of the water masses observed suggests that, post-corrections, the seal tag dataset is well matched to the mooring data, confirming that the corrections process was successful.

The distance to which partial-depth moorings can be used to estimate conditions in the upper ocean above is examined. There is good correlation for a layer above the mooring approximately 110 to 230 m thick. Over this distance, the data examined here suggest that moorings can indicate conditions above, where other observation techniques are unavailable. Above this layer, surface processes dominate, and mooring temperatures are not a good indicator of surface conditions. Other observation techniques are necessary in this depth range.

For the first time, the seasonal variation in the upper ocean is comprehensively examined. Surface salinification begins as soon as seal tag observations are available, in February, and probably begins earlier - tagging happens once there is sufficient open

water to get a science team to the seals, and this open water will provide the necessary ocean-atmosphere interface for surface salinification. The thermocline deepends from less than 50 m to approximately 250m in June / July. This and the smaller scale timeseries' presented in section 4.2 provide an essential foundation for future work on upper ocean seasonality in the region, and for model validation, as will be discussed in more detail in chapter 5.

Chapter 5

Conclusions and future work

5.1 Summary and recommendations for extracting maximum scientific value from seal tag data

In much of Antarctica, seal tag data provides the bulk of the observations available (Heywood *et al.*, 2016), and in winter, some of the only upper ocean observations available. As such, the quality of these measurements is crucial, as is getting the most informative data from each observation. After an introduction to the relevant scientific literature and key research questions in chapter 1, chapter 2 evaluates the performance of 16 tags in detail, providing significant opportunity to improve the design of future seal tag deployments. Chapter 3 utilises the abundance of the seal data to evaluate seasonal variations in CDW in the Amundsen Sea, an important step towards the accurate prediction of glacier melt and associated sea level rise. In chapter 4 the value of this seal tag data in observing the upper ocean seasonal cycle is demonstrated, and the validity of using subsurface mooring data to estimate surface conditions evaluated.

5.1.1 Seal tag data - quality control and tag design

Detailed evaluation of 16 tags revealed temperature and conductivity sensor error varied with pressure (up to 0.2 °C over 1000 db). Until the tag sensors are improved such that they no longer exhibit such large changes with pressure, tags must be calibrated with a pre-deployment test dive preferably at least as deep as the seals are likely to dive in that deployment. This is particularly true for deep deployments, where sensor errors with

pressure will be amplified. Without these pre-deployment tests, the analysis presented in section 2.3 indicates that some tags may produce data that do not meet the MEOP accuracies of +/-0.03 °C for temperature and +/-0.05 for salinity. This is particularly important given how many new conclusions are now being drawn with seal tag data, and given the paucity of data available to compare with these seal measurements in many of the study areas. Just 90 of the 349 tags (26%) described by Roquet *et al.* (2013) were corrected for pressure induced biases using at-sea comparisons with ship-based CTD profiles. For the rest, such comparisons were unavailable. We estimate Kitade *et al.* (2014) could have used data from no more than 20 tags in their study, with the availability of pressure corrections unknown. Zhang *et al.* (2016) use 80 tags, with the availability of pressure corrections unknown. Ohshima *et al.* (2013) use 16 tags, 3 of which have corrections for pressure induced biases. Many such studies have many tags, or use seal data in combination with other datasets, or are shallow deployments, and so the likelihood of erroneous conclusions is reduced. However, for a study with few tags, where pressure-error corrections and complementary traditional hydrographic observations are unavailable, if even one tag has pressure induced errors such as those observed here, then confidence in the results will be detrimentally affected. It is crucial that these pressure induced errors are addressed as a priority in seal tagging for oceanographic purposes. At the very least, studies using seal data must report how many tags comprised their datasets, and for how many of those tags corrections for pressure induced error were available. At present, some oceanographic studies using seal data omit this crucial information.

The tag compression algorithm used in this deployment did not include the MLD, and the MLD found from the compressed profiles was less accurate that the MLD found from a higher resolution profile (section 2.7). The inclusion of the MLD in the tag compression algorithm would be relatively simple, and greatly beneficial in improving understanding of the Antarctic upper ocean, particularly in winter when the upper ocean is largely unobserved. Understanding of the seasonal cycle and variability of MLD is crucial for the improvement of ocean-ice-atmosphere interaction representation in models, and the resultant effects on oceanic mixing and heat uptake.

There are purposes for which a higher vertical resolution would be desirable or necessary (e.g. investigating instabilities or stratification). Given ongoing improvements in battery life and technology, it is feasible that in future the tag compression algorithm might be altered to report higher vertical resolution (more data points per profile). However, the message length restriction (256 bytes) would necessitate any additional data points being communicated in an additional message. The more messages per profile, the more likely that one or more of those messages is not successfully received (and so some portion of the profile would be missing). It is recommended that any additional depth levels reported in an additional message be interspersed with those reported in other messages, in order to maximise the usefulness of profiles where not all messages are received. These changes could also be made without the altering the tag hardware and battery, by instead sacrificing the length of time the tags are expected to last (by using the battery faster). Alternatively, a single value which communicates some of this information could be used: for example, the percentage of the water column which was unstable. This would allow for further analysis while leaving the tag compression mostly unchanged.

5.1.2 Spatial and temporal variability of CDW in the Amundsen Sea

A priority of this thesis was to improve the knowledge of the spatial and temporal variability of CDW in the Amundsen Sea. The CDW layer was found to be $\sim$ 50 m thicker in winter in 2014, and as such contained more heat and more salt in winter (Mallett *et al.*, 2018). This is the reverse of the seasonal cycle in thickness observed in the western trough (Ha *et al.*, 2014; Kim *et al.*, 2017; Wåhlin *et al.*, 2013). In order to extend these observations of seasonal variations in 2014 into observations of a regular seasonal cycle, repeat deployments over a number of years are required. Webber *et al.* (2017) saw a seasonal cycle in CDW layer thickness using 5 years of mooring data, but this is at a single location. Since the analysis presented in chapter 3 revealed such spatial variation in seasonal variability, for example that seasonal variability in Pine Island Bay is reduced compared with the rest of the eastern Amundsen Sea, it is seal tag data in particular that are required to reveal whether these larger and smaller scale seasonal variabilities are consistent seasonal cycles, or not. No other observation technique is at present able to provide the necessary

spatial spread of observations through the seasons. A mixture of Elephant and Weddell seals is appropriate, as Weddell seals tend to spread their observations out more, providing a good spatial coverage, while Elephant seals tend to provided many repeat observations in confined areas (Figure 2.3) ensuring localised comparison between seasons is possible.

The observation of reduced seasonal variability in Pine Island Bay suggests a particular focus on this region is necessary, for both seal tagging and other observation techniques, in order to develop the understanding required to accurately predict heat delivery to the ice shelf and the associated melt. 4 of 7 Elephant seals and 2 of 7 Weddell seals (Figure 2.3) tagged visited the Pine Island Bay, and some of these seals visited only briefly, or only sampled a small area of it. In order to maximise chances of the area being well sampled, a similar number of tags must be deployed in future years, if not more.

On density surfaces, the CDW was cooler and fresher in winter, suggesting winter shoaling of density surfaces offshelf. Confirmation that this is part of a regular seasonal cycle will require future years of seal deployments to be paired with concurrent moorings at the shelf break in the eastern and central troughs.

One of the hardest aspects of analysing the seal data is the unlikely occurrence of repeat observations, where a seal returns to an exact location at a later date. Instead, here such repeat observations were simulated by averaging, for example in chapter 3 by:

- gridding data into a rectangular grid of 23 km latitudinally by 22 km longitudinally, to enable comparison between different times even when seal profiles are not exactly colocated
- excluding cells containing insufficient observations to reduce the likelihood of disproportionately weighting single profiles that might be erroneous, or not representative of the cell
- averaging within cells where enough observations are available, to provide a mean observation for each cell.

Of course, it is still possible that all seal profiles in one cell might come from one smaller

location within the cell that is not representative of the cell at large, or that the observations might all be closely spaced in time at a time when some disturbance is present (e.g. icebergs), and in such situations the calculated mean observations for such cells would not be representative. Alternative gridding could be used - perhaps based on bathymetry, in an effort to better group similar observations together, and avoid averaging across water masses, and over steep bathymetric changes. Whilst the analysis presented in this thesis sometimes added bathymetric constraints in an effort to do just this (e.g. figure 4.25), a more sophisticated grid would achieve this more effectively. Choosing any grid will inevitably be a trade-off between small localised grid cells and grid cells large enough to include a sufficient number of observations. As a result, some grid cells will contain a small number of profiles, and will be vulnerable to the same possible errors as mentioned above.

5.1.3 Observing seasonal variability in the upper ocean

Over the whole of the Amundsen Sea (Figure 4.19), surface salinification begins as soon as observations are available (February), deepening the thermocline from $<$ 50 m to $\sim$ 250 m in late June / early July (Figure 4.19). In the Amundsen Sea this surface seasonal cycle has not been observed before, as a result of the harsh conditions there preventing most winter observations, and icebergs preventing full-depth moorings.

The concurrent seal and mooring data analysed in section 4.1 show that for one mooring (PIB-N, top at 482 m depth), temperature and its variability were well correlated between the mooring top and up to 230 m above (up to $\sim$ 250 m depth, Figure 4.12). For another, shallower mooring (PIB-S, top at 303 m), the correlation extended to 110 m above (up to $\sim$ 190 m depth, Figure 4.15). Neither mooring is usable for estimating surface conditions. The difference in thickness of correlated measurements above the two moorings could be related to the different depths of those mooring tops, or to differing local flow and stratification, or sea ice cover. Given this difference between just two available moorings, the thicknesses of correlated measurements found here can be used only as estimates for other moorings, but an estimate is still useful. More concurrent and

colocated seal tag and mooring observations are necessary to constrain the variability of the correlated thickness between different moorings in different places.

5.2 Future work and recommendations

5.2.1 Future work with this dataset

With more time, the analysis would be extended by examining meltwater in the Amundsen Sea, as Zhang *et al.* (2016) did for the Bellingshausen Sea. With the aid of a trusted product for sea ice cover through time, many more opportunities for analysis could be pursued. Fluxes of heat and freshwater from the upper ocean (Pellichero *et al.*, 2018) from within polynyas could be investigated with the aid of atmospheric reanalysis data and a calculation of polynya locations (Labrousse *et al.*, 2018). Many of the seal profiles observed water that is to some degree unstable. Seal tags offer a good opportunity to investigate the frequency and locations in which instabilities occur, depending of course on where the seals are, and when, and with the caveat that seals might prefer to forage in water masses with more or less instability. With more time it would be interesting to investigate the incidence of instabilities observed closer and farther from the glacier outlets, close to known or suspected icebergs, and within and outside of polynyas. However, given the coarse vertical resolution of seal tag profiles, any such analysis would be limited to this simple spatial investigation; more detailed investigation into individual observations of instabilities would require a different tag compression algorithm, one focused on the depths at which an instability is observed.

With a database of $>$11,000 oceanographic observations, this thesis focused more on larger scale analysis where possible, averaging multiple observations to draw broader conclusions. However, many individual profiles are of great value and merit closer investigation in the future, particularly considering the sparsity of traditional observations in certain areas. The seals provide a number of profiles close the the glacier termini, where winter observations are particularly valuable.

More thorough comparison with existing models of the area would be valuable in identifying particular mechanisms, locations and parameterisations for which the models perform well or poorly, and would provide some suggestion as to where modellers might best focus their efforts for improving model performance.

5.2.2 Suggestions for future seal tagging campaigns and the Southern Ocean Observing System

In an ideal world with unlimited funds, the initial priority would be, as previously mentioned, to find and fix the cause of pressure-induced bias in the tags, or to conduct a pre-deployment tag test for every tag. Beyond this more technical concern, tags offer great opportunity to shed light on many of the unknowns of the Southern Ocean. For the Amundsen Sea, 15 plus tags every year for the next 30 years (more tags if fewer years, to ensure coverage of key areas), in combination with moorings at the shelf break and in PIB, would yield an unrivalled dataset able to describe not only seasonal cycles in almost every watermass and location of the Amundsen Sea, but how these seasonal cycles were changing with climate change, undoubtedly enabling much more accurate predictions of glacial melt. These tags would ideally be deployed on seals not only near PIG, but on those occupying the west of the Amundsen Sea as well, depending on such seals existing and being found. Repeated tag deployments have been conducted on the Kerguelen Islands for over 10 years, and a similar campaign in the Amundsen is not impossible, though it is more remote.

As part of The International Thwaites Glacier Collaboration, the Thwaites-Amundsen Regional Survey and Network Integrating Atmosphere-Ice-Ocean Processes Affecting the Sub-Ice-Shelf Environment (TARSAN) project will tag more seals in the Amundsen Sea in the next few years, with the intention of measuring oceanographic properties on the continental shelf adjacent to Thwaites, and providing the first opportunity to compare seasonal variation over the Amundsen Sea between multiple years.

More generally, a regular commitment to long-term seal tagging deployments across

the Antarctic continental shelf would provide the aforementioned benefits in many more key / under-studied regions, and would provide plentiful observations of the undersampled region of the Southern Ocean south of the ACC, providing information essential for climate modellers to improve representation of pivotal Southern Ocean processes. Likewise, the temperature data from such a database might be fed into operational ocean models, if data transmission is timely, thus increasing available observations in the high-latitude Southern Ocean (Carse *et al.*, 2015).

The author believes a new Southern Ocean Observing System (SOOS, www.soos.aq) Regional Working Group has recently been approved for the Amundsen/Bellingshausen sector. It is suggested that this working group coordinate the aforementioned sustained seal tagging program in the area, as part of fulfilling the SOOS objectives. At its minimum and as a priority, this should consist of coordinating research groups planning to send vessels, and those wishing to deploy tags, so that they might share resources and obtain tag observations in more years than if operating independently. It might also facilitate deep test dives for tags that will later be deployed from different vessels or research stations, thus increasing the value of the deployment by resolving the pressure-induced biases. At least one of the SOOS endorsed programs already plan to include seal tagging as a part of their activities in the Atlantic Sector (Ocean Regulation of Climate through Heat and Carbon Sequestration and Transports (ORCHESTRA)), but this is one project in one place, and SOOS and its constituents would benefit from broader and longer term plans for tagging. As demonstrated in this thesis, tags offer valuable and unique opportunities to resolve seasonal variation in the upper ocean and deep CDW in regions covered with sea ice. Consequently, seal tag deployments are an obvious tool for the Capability Working groups for Observing and Understanding the Ocean below Antarctic Sea Ice and Ice Shelves (OASIIS) and Southern Ocean Fluxes (SOFLUX).

The effort of finding and retagging particular seals may well be worthwhile, since seals are so variable in where they sample. For seals known to have spent a significant amount of time in a particularly important location (for example PIB), retagging would increase the chances of obtaining more data from this area. This is of course dependent

on the seal returning to the same locations at sea, and where they were originally tagged (consequently Weddell seals, tagged on sea ice, are not easily re-taggable), and on the ability of a research vessel to reach this location under differing conditions. Of course, the wellbeing of the animal is of primary importance and only an appropriately trained biologist can judge if and when retagging is acceptable.

Co-deployment of seal tags and a glider is another avenue worth pursuing. If the problems of glider deployment in cold environments could be resolved (some Antarctic deployments have been successful (Azaneu *et al.*, 2017)), glider and seal tag co-deployment would allow for the quality of the datasets to be compared, would enable estimation of the head effect on salinity in tags where other comparisions are unavailable, and might provide estimates of bathymetry to complement studies comparing seal-tag bathymetry and available bathymetric products. Gliders would be best used (in tandem with seal tags) to conduct repeat sections previously occupied by helpful seals, thus addressing the lack of reliable repeat observations that are an inevitable part of seal tag data.

Surface vehicles such as Wavegliders or Autonauts might also, in future, offer interesting opportunities when paired with seal data. Currently, deployment of such vehicles is also fraught with the dangers of the harsh conditions, and the problems of ice accumulation. Provided such problems could be overcome, a pairing of a surface vehicle within a polynya and concurrent, co-located seal tag observations would offer an unrivalled opportunity to examine winds and fluxes in heat and freshwater in Antarctic polynyas, and their effects on the mixed layer and water transformation below.

This work has focused on seasonal variation in the water masses of the Amundsen sea, from the deep warm CDW which melts the Amundsen Sea ice shelves, to the upper ocean, where winter observations have never before been available. The value and caveats of seal tag data are thoroughly demonstrated, and recommendations put forward for future deployments in similar locations. The Amundsen Sea Embayment is a continental shelf region with warm CDW flooding toward and melting ice shelves, and there are many similar locations around Antarctica where similar processes are thought to be, or have

been observed occurring. The use of the methods described here in these other locations would offer improved prediction of sea level rise.

Appendix A

Model details

Table A.1: Model details

Model reference	Thoma et al., 2008	Schodlok et al., 2012	Steig et al., 2012	St Laurent et al., 2013	Rodriguez et al, 2016	Nakayama et al., 2017
Model / Region	Regional ice–ocean model. Miami Isopycnic Coordinate Ocean Model. Isotropic grid	Eastern & central Amundsen Sea. MITgcm, ECCO2 configuration	Uses Thoma et al. (2008) monthly output	ROMS v3.4. 600 km x 300 km. Represents idealized coastal segment.	Coast to continental shelf, 124.258W and 98.428W. Southern Ocean State Estimate. MITgcm	Regional model. MITgcm.
Horizontal spacing	13.5 km in south, 28 km in north	1km	--	Eddy resolving. 1 km	1/6th degree Eddy permitting	Approximately 10 km
Vertical spacing	11 layers	50 levels, varying thickness	--	--	42 levels, varying thickness	50 levels varying in thickness.
Forcing	Sea-level pressure, sea surface temperature from NCEP/NCAR reanalysis. Coupled with simple sea ice model	Dynamic/ thermodynamic sea-ice model. Initial conditions: World Ocean Atlas 2005. Atmos: JRA-25	--	Idealized	Observational constraints. No ice shelf model. Constrained to sea ice observations.	Dynamic/thermodynamic sea ice. Thermodynamic ice shelves. No explicit representation of ocean - ice shelf interactions
Bathymetry	Blending BEDMAP with Nitsche et al. [2007]	2 simulations: BEDMAP , and NASA IceBridge-derived	--	Represents idealized coastal segment	--	IBCSO
Ice draft	Sub-ice-shelf cavities	--	--	400 m to zero over 110 km. Ice shelf static but thermodynamically active.	--	BEDMAP-2

Appendix B

Supplementary Material

This supporting information provides figures supplementary to those presented in the main article. Included is a salinity section, equivalent to Figure 3.2, and a number of maps of fields relevant to Figure 3.3.

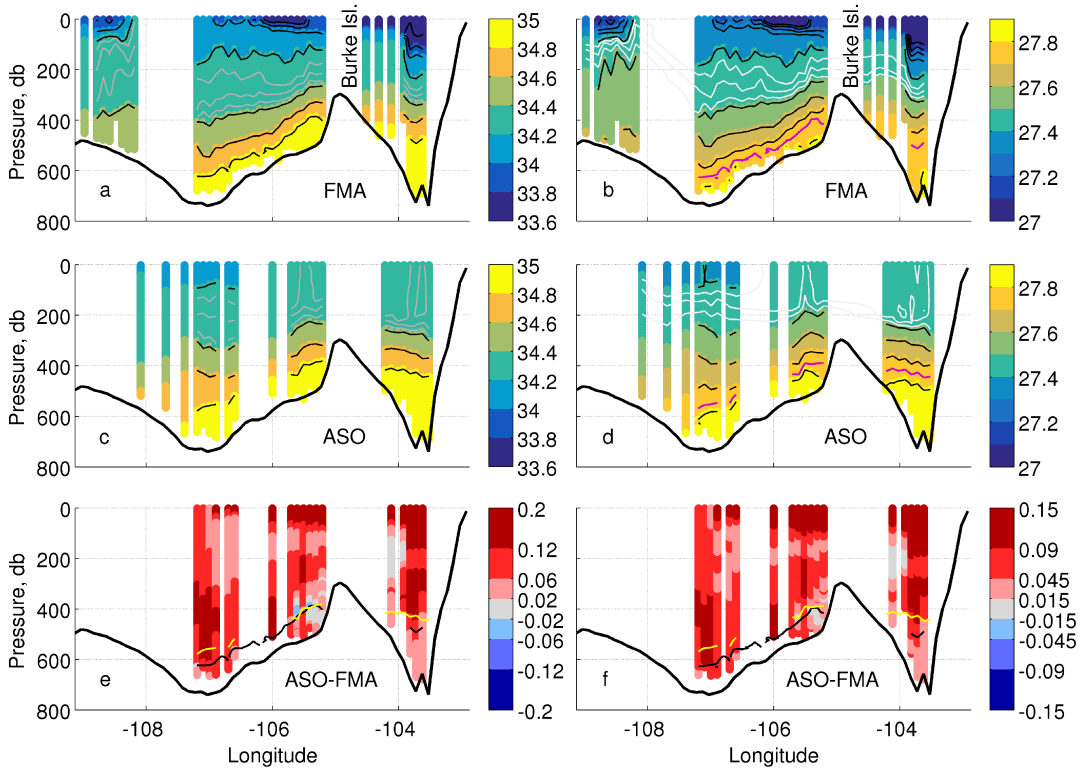

Figure B.1: As in Figure 3.2 in the main article, but where (a,c and e) show absolute salinity. Black and yellow contours in (e) are at 34.8 g/kg in summer and winter respectively.

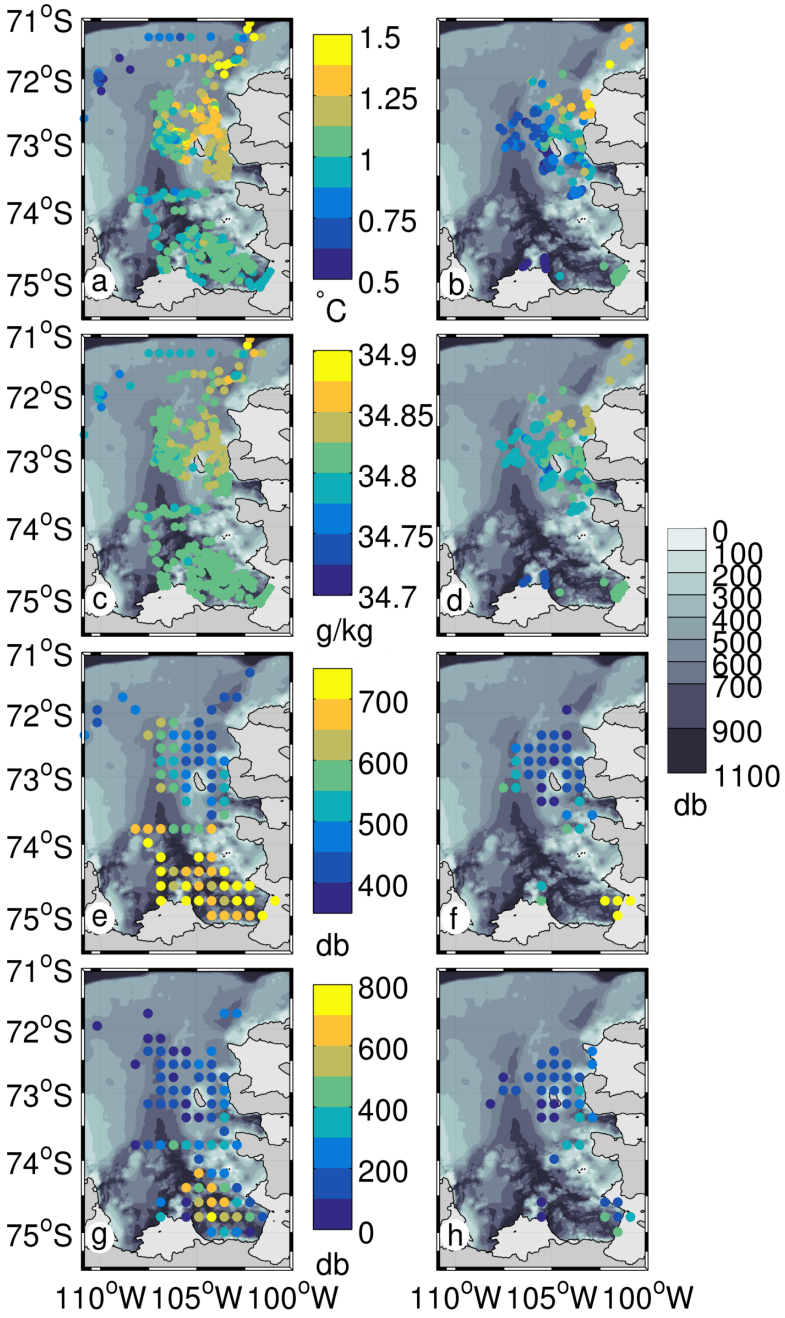

Figure B.2: The fields used to produce the seasonal difference maps presented in Figure 3.3 in the main article. Panels on the left are in summer, on the right in winter. (a,b) conservative temperature, and (c,d) absolute salinity, on the 27.76 isopycnal. (e,f) the pressure of the 27.76 isopycnal, and (g,h) the thickness of the layer beneath the 0°C isotherm, where observations are gridded in latitude and longitude.

Appendix C

Additional sections

Additional sections are provided: one just south of Burke Island, one crossing PIB, and one north of Dotson and Getz ice shelves (Figure C.1).

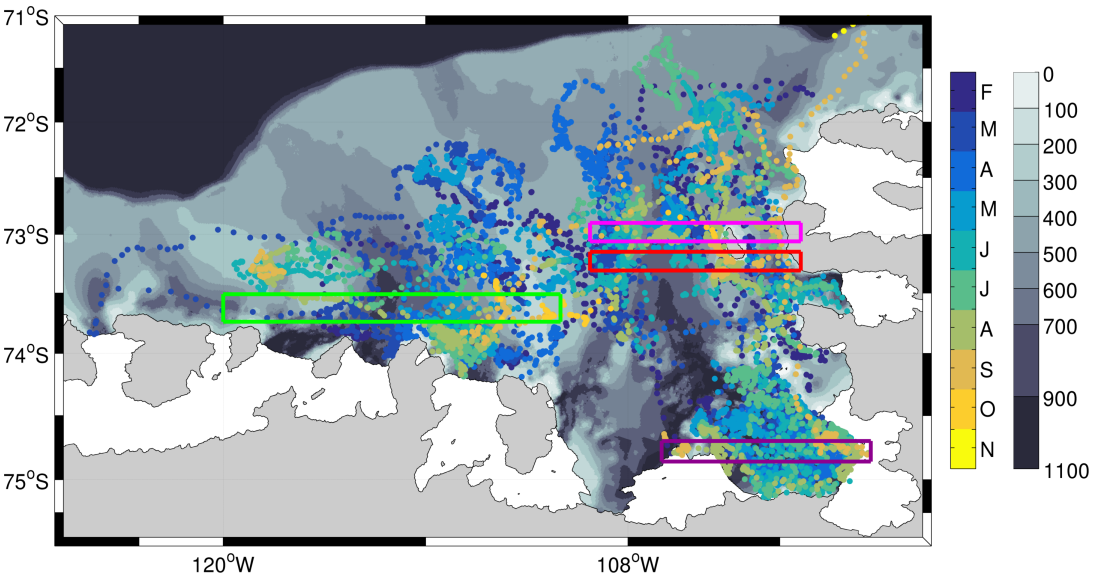

Figure C.1: The Amundsen Sea with CTD profiles collected by seals, coloured by date. Winter profile locations overlie some summer and autumn locations. The coloured rectangles contain the observations used in the sections. The pink rectangle is the section as in figure 3.2, while the red, purple and green rectangles are the additional sections not previously published. Bathymetry is IBCSO (Arndt *et al.*, 2013), coastline and grounding line are Bedmap2 in white and grey (Fretwell *et al.*, 2013).

More obvious south of Burke Island (figure C.2) than in the section in the paper, north of Burke Island (figure 3.2, is the thicker layer of CDW to the east of Burke Island. South of Burke Island the temperature through much of the upper water column is greater in summer (FMA) than winter (ASO), with little change in the CDW layer (figure C.2g),

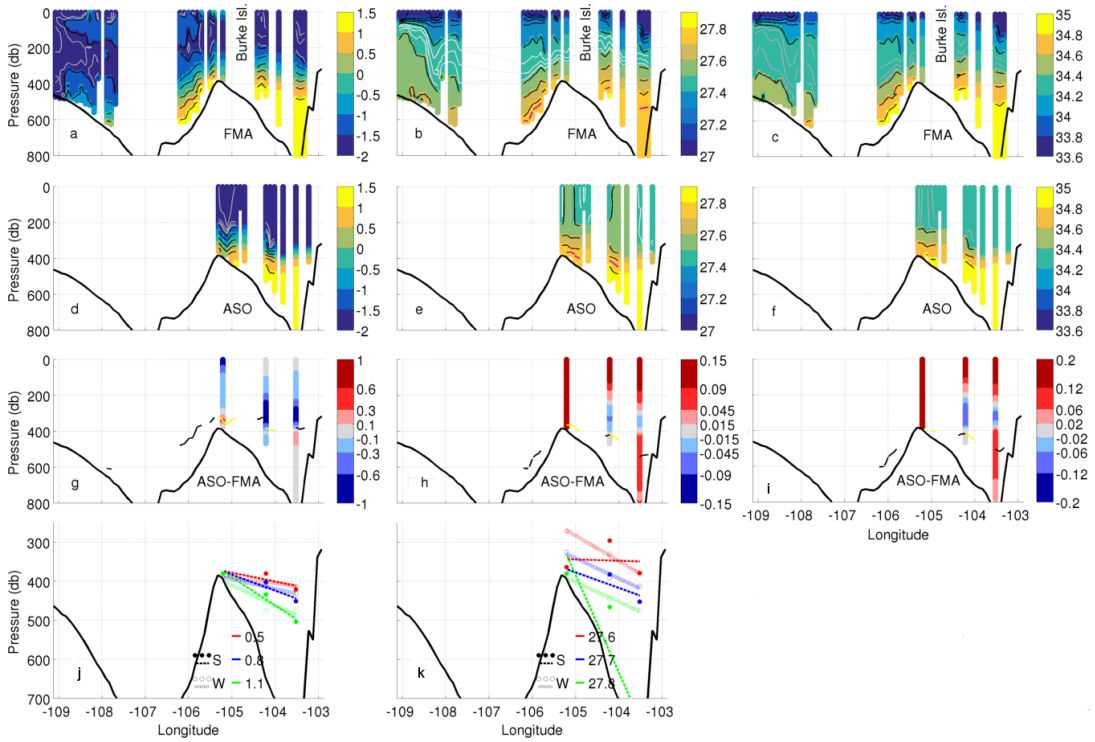

Figure C.2: As in figures 3.2 and B.1, conservative temperature (left), potential density anomaly (middle) and absolute salinity (right), but for the section marked in red in figure C.1 (using the same colour scales as figures 3.2 and B.1, for ease of comparison).

but north of Burke Island the whole water column is warmer in winter on pressure surfaces (figure 3.2e). For both seasons most of the water column is denser in winter (winter shoaling of density surfaces), but for a layer at $\sim$ 300 m (figure C.2h), which is denser in summer (sinking density surface in summer).

Through PIB the doming of the isopycnals, resulting from the crculating gyre, is clearly visible in summer and autumn (figure C.3b,e). In winter, a lack of profiles in the centre of PIB means this cannot be judged. Between summer and autumn density surfaces in the centre of the gyre shoal (denser in autumn, figure C.3h), while toward the western edge of PIB the reverse is true, suggesting perhaps an autumn increase in the gyre speed, or a lateral movement of the gyre from one season to the next. Deep CDW temperatures change little season to season (figure C.3g,m).

North of Getz and Dotson a section reveals very localised reversals in isopycnal shoaling and sinking between summer and autumn, between 114 and 116 ^{circ} W, north east of Getz ice shelf (figure C.4h). This suggests changes in flow that are confined in depth,

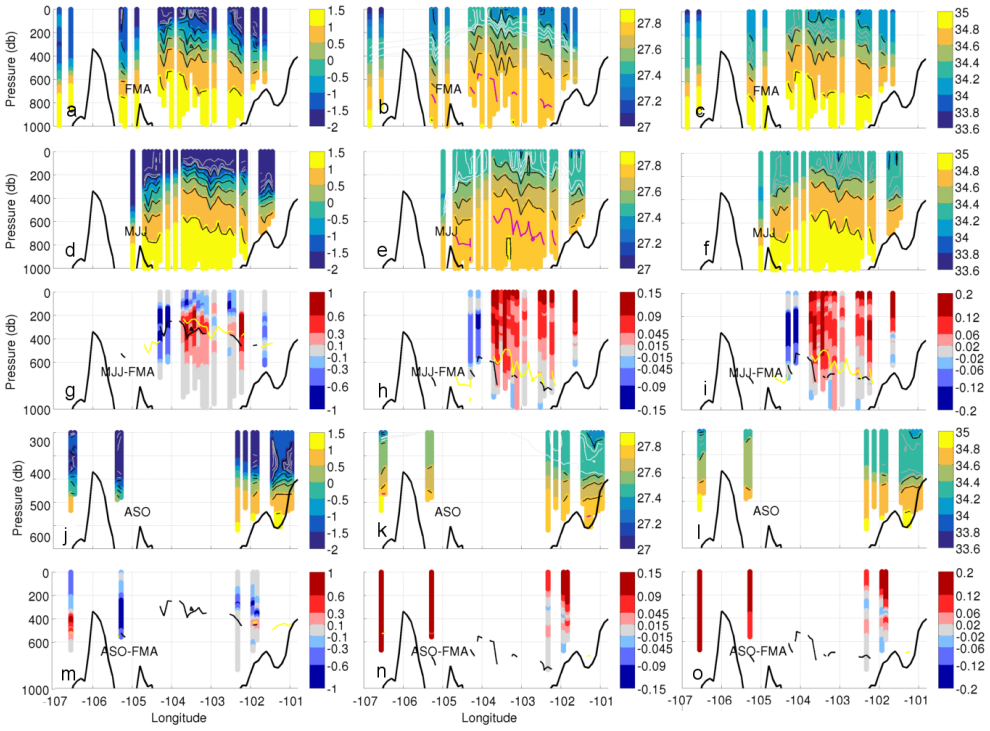

Figure C.3: Similar to figure C.2, conservative temperature (left), potential density anomaly (middle) and absolute salinity (right), but for the section marked in purple in figure C.1, and with Autumn (MJJ) and Autumn - Summer (MJJ-FMA) panels.

possibly as a result of changing glacial outflow.

These sections provide an insight into the seasonal changes in these areas, and highlight how localised many off these changes in density surfaces and in temperature and salinty are. Much of the local influence is likely local atmospheric forcing, and in chapter 4 the seasonal changes in the upper ocean are investigated, and the usefulness of subsurface moorings for extrapolating upper ocean conditions is examined.

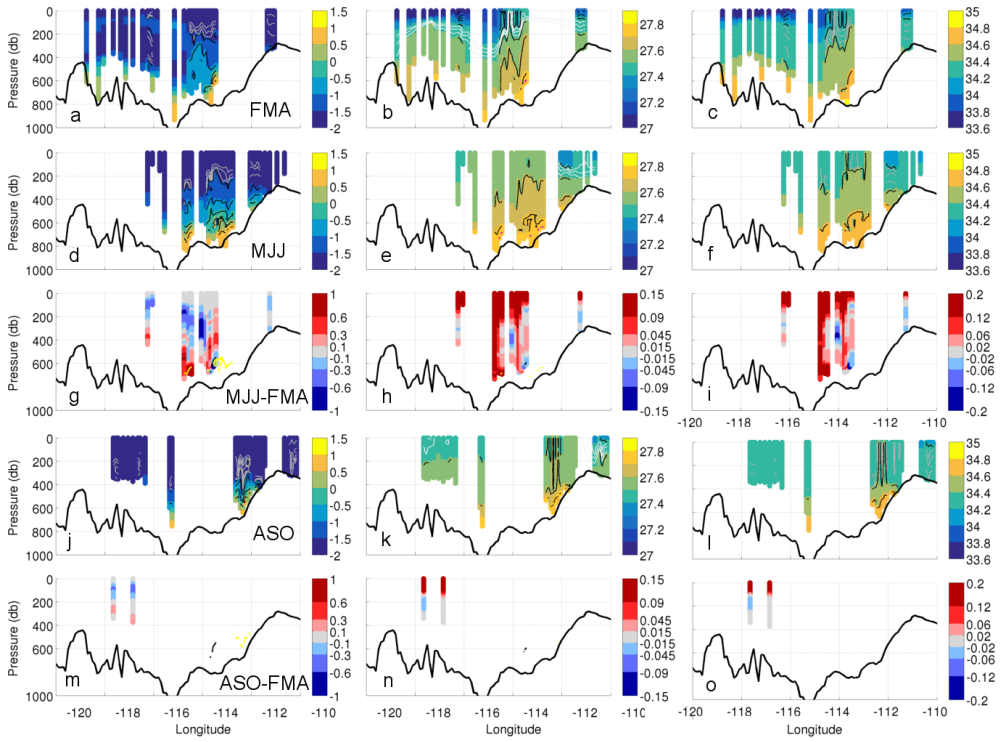

Figure C.4: As in figure C.3, conservative temperature (left), potential density anomaly (middle) and absolute salinity (right), but for the section marked in green in figure C.1 (using the same colour scales as figures 3.2 and B.1).

References

Adcock, S. T., and D. P. Marshall (2000), Interactions between Geostrophic Eddies and the Mean Circulation over Large-Scale Bottom Topography, *Journal of Physical Oceanography*, *30*(12), 3223–3238.

Arndt, J. E., H. W. Schenke, M. Jakobsson, F. O. Nitsche, G. Buys, B. Goleby, M. Rebesco, F. Bohoyo, J. Hong, J. Black, R. Greku, G. Udintsev, F. Barrios, W. Reynoso-Peralta, M. Taisei, and R. Wigley (2013), The international bathymetric chart of the Southern Ocean (IBCSO) version 1.0-A new bathymetric compilation covering circum-Antarctic waters, *Geophysical Research Letters*, *40*(12), 3111–3117.

Arneborg, L., A. K. Wåhlin, G. Björk, B. Liljebladh, and A. H. Orsi (2012), Persistent inflow of warm water onto the central Amundsen shelf, *Nature Geoscience*, *5*(12), 876–880.

Azaneu, M., K. J. Heywood, B. Y. Queste, and A. F. Thompson (2017), Variability of the Antarctic Slope Current System in the Northwestern Weddell Sea, *Journal of Physical Oceanography*, *47*(12), 2977–2997.

Bailleul, F., M. Authier, S. Ducatez, F. Roquet, J.-B. Charrassin, Y. Cherel, and C. Guinet (2010), Looking at the unseen: combining animal bio-logging and stable isotopes to reveal a shift in the ecological niche of a deep diving predator, *Ecography*, *33*(4), 709–719.

Bamber, J. L., R. E. M. Riva, B. L. A. Vermeersen, and A. M. LeBrocq (2009), Reassessment of the Potential Sea-Level Rise from a Collapse of the West Antarctic Ice Sheet, *Science*, *324*(5929), 901–903.

Barker, P. M., and T. J. McDougall (2017), Stabilizing Hydrographic Profiles with Minimal Change to the Water Masses, *Journal of Atmospheric and Oceanic Technology*, *34*(9), 1935–1945.

Biuw, M., L. Boehme, C. Guinet, M. Hindell, D. Costa, J.-B. Charrassin, F. Roquet, F. Bailleul, M. Meredith, S. Thorpe, Y. Tremblay, B. McDonald, Y.-H. Park, S. R. Rintoul, N. Bindoff, M. Goebel, D. Crocker, P. Lovell, J. Nicholson, F. Monks, and M. A. Fedak (2007), Variations in behavior and condition of a Southern Ocean top predator in relation to in situ oceanographic conditions, *Proceedings of the National Academy of Sciences*, *104*(34), 13,705–13,710.

Boehme, L., K. Kovacs, C. Lydersen, O. A. Nøst, M. Biuw, J.-B. Charrassin, F. Roquet, C. Guinet, M. Meredeth, K. Nichols, S. Thorpe, D. P. Costa, B. Block, M. Hammill, G. Stenson, M. Muelbert, M. N. Bester, J. Plötz, H. Bornemann, M. Hindell, S. Rintoul, P. Lovell, and M. A. Fedak (2010), Biologging in the Global Ocean Observing System, in: *Proceedings of OceanObs'09: Sustained Ocean Observations and Information for Society*, pp. 47–55, European Space Agency.

Boehme, L., P. Lovell, M. Biuw, F. Roquet, J. Nicholson, S. E. Thorpe, M. P. Meredith, and M. Fedak (2009), Technical Note: Animal-borne CTD-Satellite Relay Data Loggers for real-time oceanographic data collection, *Ocean Science*, *5*(4), 685–695.

Böhme, L., and U. Send (2005), Objective analyses of hydrographic data for referencing profiling float salinities in highly variable environments, *Deep Sea Research Part II: Topical Studies in Oceanography*, *52*(3-4), 651–664.

Carse, F., M. J. Martin, A. Sellar, and E. W. Blockley (2015), Impact of assimilating temperature and salinity measurements by animal-borne sensors on FOAM ocean model fields, *Quarterly Journal of the Royal Meteorological Society*, *141*(693), 2934–2943.

Cavalieri, D. J., C. L. Parkinson, P. Gloersen, and H. J. Zwally (1996), Sea Ice Concentrations from Nimbus-7 SMMR and DMSP SSM/I-SSMIS Passive Microwave Data, Version 1, *Boulder, Colorado USA. NASA National Snow and Ice Data Center Distributed Active Archive Center*.

Costa, D. P., J. M. Klinck, E. E. Hofmann, M. S. Dinniman, and J. M. Burns (2008), Upper ocean variability in west Antarctic Peninsula continental shelf waters as measured using instrumented seals, *Deep Sea Research Part II: Topical Studies in Oceanography*, *55*(3-4), 323–337.

de Boyer Montégut, C., G. Madec, A. S. Fischer, A. Lazar, and D. Iudicone (2004), Mixed layer depth over the global ocean: An examination of profile data and a profile-based climatology, *Journal of Geophysical Research*, *109*(C12), C12,003.

Dee, D. P., S. M. Uppala, A. J. Simmons, P. Berrisford, P. Poli, S. Kobayashi, U. Andrae, M. A. Balmaseda, G. Balsamo, P. Bauer, P. Bechtold, A. C. M. Beljaars, L. van de Berg, J. Bidlot, N. Bormann, C. Delsol, R. Dragani, M. Fuentes, A. J. Geer, L. Haimberger, S. B. Healy, H. Hersbach, E. V. Hólm, L. Isaksen, P. Kållberg, M. Köhler, M. Matricardi, A. P. McNally, B. M. Monge-Sanz, J.-J. Morcrette, B.-K. Park, C. Peubey, P. de Rosnay, C. Tavolato, J.-N. Thépaut, and F. Vitart (2011), The ERA-Interim reanalysis: configuration and performance of the data assimilation system, *Quarterly Journal of the Royal Meteorological Society*, *137*(656), 553–597.

Dinniman, M. S., J. M. Klinck, E. E. Hofmann, and W. O. Smith (2018), Effects of Projected Changes in Wind, Atmospheric Temperature, and Freshwater Inflow on the Ross Sea, *Journal of Climate*, *31*(4), 1619–1635.

Dong, S., J. Sprintall, S. T. Gille, and L. Talley (2008), Southern Ocean mixed-layer depth from Argo float profiles, *Journal of Geophysical Research*, *113*(C6), C06,013.

Dutrieux, P., J. De Rydt, A. Jenkins, P. R. Holland, H. K. Ha, S. H. Lee, E. J. Steig, Q. Ding, E. P. Abrahamsen, and M. Schröder (2014), Strong sensitivity of Pine Island ice-shelf melting to climatic variability., *Science*, *343*(6167), 174–8.

Fedak, M. (2004), Marine animals as platforms for oceanographic sampling: a " win/win " situation for biology and operational oceanography, *Mem. Natl Inst. Polar Res.*, (Special Issue 58), 133–147.

Fedak, M. (2013), The impact of animal platforms on polar ocean observation, *Deep Sea Research Part II: Topical Studies in Oceanography*, *88-89*, 7–13.

Fedak, M., P. Lovell, B. McConnell, and C. Hunter (2002), Overcoming the Constraints of Long Range Radio Telemetry from Animals: Getting More Useful Data from Smaller Packages, *Integrative and Comparative Biology*, *42*(1), 3–10.

Fretwell, P., H. D. Pritchard, D. G. Vaughan, J. L. Bamber, N. E. Barrand, R. Bell, C. Bianchi, R. G. Bingham, D. D. Blankenship, G. Casassa, G. Catania, D. Callens, H. Conway, A. J. Cook, H. F. J. Corr, D. Damaske, V. Damm, F. Ferraccioli, R. Forsberg, S. Fujita, Y. Gim, P. Gogineni, J. A. Griggs, R. C. A. Hindmarsh, P. Holmlund, J. W. Holt, R. W. Jacobel, A. Jenkins, W. Jokat, T. Jordan, E. C. King, J. Kohler, W. Krabill, M. Riger-Kusk, K. A. Langley, G. Leitchenkov, C. Leuschen, B. P. Luyendyk, K. Matsuoka, J. Mouginot, F. O. Nitsche, Y. Nogi, O. A. Nost, S. V. Popov, E. Rignot, D. M. Rippin, A. Rivera, J. Roberts, N. Ross, M. J. Siegert, A. M. Smith, D. Steinhage, M. Studinger, B. Sun, B. K. Tinto, B. C. Welch, D. Wilson, D. A. Young, C. Xiangbin, and A. Zirizzotti (2013), Bedmap2: Improved ice bed, surface and thickness datasets for Antarctica, *Cryosphere*, *7*(1), 375–393.

Garabato, A. C. N., A. Forryan, P. Dutrieux, L. Brannigan, L. C. Biddle, K. J. Heywood, A. Jenkins, Y. L. Firing, and S. Kimura (2017), Vigorous lateral export of the meltwater outflow from beneath an Antarctic ice shelf, *Nature*, *542*(7640), 219–222.

Ha, H. K., A. K. Wåhlin, T. W. Kim, S. H. Lee, J. H. Lee, H. J. Lee, C. S. Hong, L. Arneborg, G. Björk, and O. Kalén (2014), Circulation and Modification of Warm Deep Water on the Central Amundsen Shelf, *Journal of Physical Oceanography*, *44*(5), 1493–1501.

Herraiz-Borreguero, L., R. Coleman, I. Allison, S. R. Rintoul, M. Craven, and G. D. Williams (2015), Circulation of modified Circumpolar Deep Water and basal melt beneath the Amery Ice Shelf, East Antarctica, *Journal of Geophysical Research C: Oceans*, *120*(4), 3098–3112.

Heywood, K., L. Biddle, L. Boehme, P. Dutrieux, M. Fedak, A. Jenkins, R. Jones, J. Kaiser, H. Mallett, A. Naveira Garabato, I. Renfrew, D. Stevens, and B. Webber (2016), Between the Devil and the Deep Blue Sea: The Role of the Amundsen Sea Continental Shelf in Exchanges Between Ocean and Ice Shelves, *Oceanography*, *29*(4), 118–129.

Heywood, K. J., L. Biddle, M. Preston, G. Damerell, S. Woodward, S. Kimura, R. Jones, B. Queste, A. Bigdeli, B. Loose, A. Forryan, A. Naviera Garaboto, J. Wynar, A. Jenkins, P. Dutrieux, S. McPhail, P. Abrahamsen, P. Provost, and M. Fedak (2014), *JR294/295 Cruise Report Ice Sheet Stability Programme (iSTAR)*, Tech. rep., Centre for Ocean and Atmospheric Sciences, University of East Anglia.

Hindell, M., H. Burton, and D. Slip (1991), Foraging areas of southern elephant seals, Mirounga leonina, as inferred from water temperature data, *Marine and Freshwater Research*, *42*(2), 115.

Holte, J., and L. Talley (2009), A New Algorithm for Finding Mixed Layer Depths with Applications to Argo Data and Subantarctic Mode Water Formation*, *Journal of Atmospheric and Oceanic Technology*, *26*(9), 1920–1939.

Jacobs, S. S., C. F. Giulivi, and P. A. Mele (2002), Freshening of the Ross Sea During the Late 20th Century, *Science*, *297*(5580), 386–389.

Jacobs, S. S., A. Jenkins, C. F. Giulivi, and P. Dutrieux (2011), Stronger ocean circulation and increased melting under Pine Island Glacier ice shelf, *Nature Geoscience*, *4*(8), 519–523.

Jacobs, S. S., A. Jenkins, H. H. Hellmer, C. F. Giulivi, F. Nitsche, B. Huber, and R. Guerrero (2012), The Amundsen Sea and the Antarctic Ice Sheet, *Oceanography*, *25*(3), 154–163.

Jenkins, A., P. Dutrieux, S. S. Jacobs, S. D. McPhail, J. R. Perrett, A. T. Webb, and D. White (2010), Observations beneath Pine Island Glacier in West Antarctica and implications for its retreat, *Nature Geoscience*, *3*(7), 468–472.

Jenkins, A., D. G. Vaughan, S. S. Jacobs, H. H. Hellmer, and J. R. Keys (1997), Glaciological and oceanographic evidence of high melt rates beneath Pine Island Glacier, West Antarctica, *Journal of Glaciology*, *43*(143), 114–121.

Johnson, J. A., and N. Rockliff (1986), Shelf Break Circulation Processes, in: *Baroclinic Processes on Continental Shelves Vol. 3, Coastal and Estuarine Sciences*, vol. 3, pp. 19–31, American Geophysical Union.

Jones, R. W., I. A. Renfrew, A. Orr, B. G. M. Webber, D. M. Holland, and M. A. Lazzara (2016), Evaluation of four global reanalysis products using in situ observations in the Amundsen Sea Embayment, Antarctica, *Journal of Geophysical Research: Atmospheres*, *121*(11), 6240–6257.

Kim, T., H. Ha, S. Lee, C. Kim, J. Lee, and Y. Cho (2017), Is Ekman pumping responsible for the seasonal variation of warm circumpolar deep water in the Amundsen Sea?, *Continental Shelf Research*, *132*, 38–48.

Kitade, Y., K. Shimada, T. Tamura, G. D. Williams, S. Aoki, Y. Fukamachi, F. Roquet, M. Hindell, S. Ushio, and K. I. Ohshima (2014), Antarctic bottom water production from the Vincennes Bay Polynya, East Antarctica, *Geophysical Research Letters*, *41*(10), 3528–3534.

Klinck, J. M. (1996), Circulation near submarine canyons: A modeling study, *Journal of Geophysical Research: Oceans*, *101*(C1), 1211–1223.

Labrousse, S., J. Vacquié-Garcia, K. Heerah, C. Guinet, J.-B. Sallée, M. Authier, B. Picard, F. Roquet, F. Bailleul, M. Hindell, and J.-B. Charrassin (2015), Winter use of sea ice and ocean water mass habitat by southern elephant seals: The length and breadth of the mystery, *Progress in Oceanography*, *137*, 52–68.

Labrousse, S., G. Williams, T. Tamura, S. Bestley, J.-B. Sallée, A. D. Fraser, M. Sumner, F. Roquet, K. Heerah, B. Picard, C. Guinet, R. Harcourt, C. McMahon, M. A. Hindell, and J.-B. Charrassin (2018), Coastal polynyas: Winter oases for subadult southern elephant seals in East Antarctica, *Scientific Reports*, *8*(1), 3183.

Lopez, R., J.-P. Malardé, P. Danès, P. Gaspar, R. Lopez, J.-P. Malarde, F. Royer, P. Gaspar, H. Blom, Y. Bar-Shalom, R. Kalman, X. Li, V. Jilkov, F. Gustafsson, D. Fraser, J. Potter, H. Rauch, F. Tung, C. Striebel, R. Helmick, W. Blair, S. Hoffman, D. Barber, B. Mesot, D. Barber, D. Barber, G. Ackerson, K. Fu, W. Koch, L. Hawkes, S. Balachandran, N. Batbayar, P. Butler, P. Frappell, W. Milsom, N. Tseveenmyadag, S. Newman, G. Scott, P. Sathiyaselvam, J. Takekawa, M. Wikelski, C. Bishop, S. Benhamou, J. Sudre, J. Bourjea, S. Ciccione, A. Santis, P. Luschi, S. Villegas-Amtmann, S. Simmons, C. Kuhn, L. Huckstadt, D. Costa, P. Robinson, D. Costa, D. Crocker, J. Gallo-Reynoso, C. Champagne, M. Fowler, C. Goetsch, K. Goetz, J. Hassrick, L. Hückstädt, C. Kuhn, J. Maresh, S. Maxwell, B. McDonald, S. Peterson, S. Simmons, N. Teutschel, S. Villegas-Amtmann, K. Yoda, A.-C. Dragon, P. Monestiez,

A. Bar-Hen, C. Guinet, A.-C. Dragon, A. BarHen, P. Monestiez, C. Guinet, D. Douglas, R. Weinzierl, S. Davidson, R. Kays, M. Wikelski, G. Bohrer, Y. Tremblay, S. Shaffer, S. Fowler, C. Kuhn, B. McDonald, M. Weise, C.-A. Bost, H. Weimerskirch, D. Crocker, M. Goebel, D. Costa, F. Royer, M. Lutcavage, I. Jonsen, J. Flemming, R. Myers, B. McConnell, C. Chambers, K. Nicholas, M. Fedak, D. Austin, J. McMillan, and W. Bowen (2015), Improving Argos Doppler location using multiple-model smoothing, *Animal Biotelemetry*, *3*(1), 32.

Lopez, R., J.-P. Malardé, F. Royer, and P. Gaspar (2014), Improving Argos Doppler Location Using Multiple-Model Kalman Filtering, *IEEE Transactions on Geoscience and Remote Sensing*, *52*(8), 4744–4755.

Lorbacher, K., D. Dommenget, P. P. Niiler, and A. Köhl (2006), Ocean mixed layer depth: A subsurface proxy of ocean-atmosphere variability, *Journal of Geophysical Research*, *111*(C7), C07,010.

Mallett, H. K. W., L. Boehme, M. Fedak, K. J. Heywood, D. P. Stevens, and F. Roquet (2018), Variation in the Distribution and Properties of Circumpolar Deep Water in the Eastern Amundsen Sea, on Seasonal Timescales, Using Seal-Borne Tags, *Geophysical Research Letters*, *45*(10), 4982–4990.

Mankoff, K. D., S. S. Jacobs, S. M. Tulaczyk, and S. E. Stammerjohn (2012), The role of pine island glacier ice shelf basal channels in deep-water upwelling, polynyas and ocean circulation in pine island bay, antarctica, *Annals of Glaciology*, *53*(60), 123–128.

McConnell, B. J., C. Chambers, and M. A. Fedak (1992), Foraging Ecology of Southern Elephant Seals in Relation to the Bathymetry and Productivity of the Southern-Ocean, *Antarctic Science*, *4*(4), 393–398.

McDougall, T., and P. Barker (2011), Getting started with TEOS-10 and the Gibbs Seawater (GSW) Oceanographic Toolbox, in: *SCOR/IAPSO WG127*, p. 28pp.

McIntyre, T., P. J. N. de Bruyn, I. J. Ansorge, M. N. Bester, H. Bornemann, J. Plötz, and C. A. Tosh (2010), A lifetime at depth: Vertical distribution of southern elephant seals in the water column, *Polar Biology*, *33*(8), 1037–1048.

Mensah, V., F. Roquet, L. Siegelman-Charbit, B. Picard, E. Pauthenet, and C. Guinet (2018), A Correction for the Thermal MassInduced Errors of CTD Tags Mounted on Marine Mammals, *Journal of Atmospheric and Oceanic Technology*, *35*(6), 1237–1252.

Mouginot, J., E. Rignot, and B. Scheuchl (2014), Sustained increase in ice discharge from the Amundsen Sea Embayment, West Antarctica, from 1973 to 2013, *Geophysical Research Letters*, *41*(5), 1576–1584.

Nakayama, Y., D. Menemenlis, M. Schodlok, and E. Rignot (2017), Amundsen and Bellingshausen Seas simulation with optimized ocean, sea ice, and thermodynamic ice shelf model parameters, *Journal of Geophysical Research: Oceans*, *122*(8), 6180–6195.

Nakayama, Y., M. Schröder, and H. H. Hellmer (2013), From circumpolar deep water to the glacial meltwater plume on the eastern Amundsen Shelf, *Deep-Sea Research Part I: Oceanographic Research Papers*, *77*, 50–62.

Nakayama, Y., R. Timmermann, C. B. Rodehacke, M. Schröder, and H. H. Hellmer (2014), Modeling the spreading of glacial meltwater from the Amundsen and Bellingshausen Seas, *Geophysical Research Letters*, *41*(22), 7942–7949.

Nitsche, F. O., S. S. Jacobs, R. D. Larter, and K. Gohl (2007), Bathymetry of the Amundsen Sea continental shelf: Implications for geology, oceanography, and glaciology, *Geochemistry, Geophysics, Geosystems*, *8*(10).

Ohshima, K. I., Y. Fukamachi, G. D. Williams, S. Nihashi, F. Roquet, Y. Kitade, T. Tamura, D. Hirano, L. Herraiz-Borreguero, I. Field, M. Hindell, S. Aoki, and M. Wakatsuchi (2013), Antarctic Bottom Water production by intense sea-ice formation in the Cape Darnley polynya, *Nature Geoscience*, *6*(3), 235–240.

Orsi, A. H., T. Whitworth, and W. D. Nowlin (1995), On the meridional extent and fronts of the Antarctic Circumpolar Current, *Deep-Sea Research Part I*, *42*(5), 641–673.

Padman, L., D. P. Costa, S. T. Bolmer, M. E. Goebel, L. A. Huckstadt, A. Jenkins, B. I. McDonald, and D. R. Shoosmith (2010), Seals map bathymetry of the Antarctic continental shelf, *Geophysical Research Letters*, *37*(21), n/a–n/a.

Paolo, F. S., H. A. Fricker, and L. Padman (2015), Volume loss from Antarctic ice shelves is accelerating, *Science*, *348*(6232), 327–332.

Payne, A. J., P. R. Holland, A. P. Shepherd, I. C. Rutt, A. Jenkins, and I. Joughin (2007), Numerical modeling of ocean-ice interactions under Pine Island Bay's ice shelf, *Journal of Geophysical Research*, *112*(C10), C10,019.

Payne, A. J., A. Vieli, A. P. Shepherd, D. J. Wingham, and E. Rignot (2004), Recent dramatic thinning of largest West Antarctic ice stream triggered by oceans, *Geophysical Research Letters*, *31*(23), 1–4.

Pellichero, V., J.-B. Sallée, C. C. Chapman, and S. M. Downes (2018), The southern ocean meridional overturning in the sea-ice sector is driven by freshwater fluxes, *Nature Communications*, *9*(1), 1789.

Photopoulou, T., M. A. Fedak, J. Matthiopoulos, B. McConnell, and P. Lovell (2015), The generalized data management and collection protocol for Conductivity-Temperature-Depth Satellite Relay Data Loggers, *Animal Biotelemetry*, *3*(1), 21.

Rignot, E., J. L. Bamber, M. R. van den Broeke, C. Davis, Y. Li, W. J. van de Berg, and E. van Meijgaard (2008), Recent Antarctic ice mass loss from radar interferometry and regional climate modeling, *Nature Geosci*, *1*(February), 106–110.

Rignot, E., J. Mouginot, M. Morlighem, H. Seroussi, and B. Scheuchl (2014), Widespread, rapid grounding line retreat of Pine Island, Thwaites, Smith, and Kohler glaciers, West Antarctica, from 1992 to 2011, *Geophysical Research Letters*, *41*(10), 3502–3509.

Rintoul, S. R. (2007), Rapid freshening of Antarctic Bottom Water formed in the Indian and Pacific oceans, *Geophysical Research Letters*, *34*(6), L06,606.

Rodriguez, A. R., M. R. Mazloff, and S. T. Gille (2016), An oceanic heat transport pathway to the Amundsen Sea Embayment, *Journal of Geophysical Research: Oceans*, *121*(5), 3337–3349.

Roquet, F., J. B. Charrassin, S. Marchand, L. Boehme, M. Fedak, G. Reverdin, and C. Guinet (2011), Delayed-mode calibration of hydrographic data obtained from animal-borne satellite relay data loggers, *Journal of Atmospheric and Oceanic Technology*, *28*(6), 787–801.

Roquet, F., Y.-H. Park, C. Guinet, F. Bailleul, and J.-B. Charrassin (2009), Observations of the Fawn Trough Current over the Kerguelen Plateau from instrumented elephant seals, *Journal of Marine Systems*, *78*(3), 377–393.

Roquet, F., G. Williams, M. A. Hindell, R. Harcourt, C. McMahon, C. Guinet, J.-B. Charrassin, G. Reverdin, L. Boehme, P. Lovell, and M. Fedak (2014), A Southern Indian Ocean database of hydrographic profiles obtained with instrumented elephant seals., *Scientific data*, *1*, 140,028.

Roquet, F., C. Wunsch, G. Forget, P. Heimbach, C. Guinet, G. Reverdin, J. B. Charrassin, F. Bailleul, D. P. Costa, L. A. Huckstadt, K. T. Goetz, K. M. Kovacs, C. Lydersen, M. Biuw, O. A. Nøst, H. Bornemann, J. Ploetz, M. N. Bester, T. McIntyre, M. C. Muelbert, M. A. Hindell, C. R. McMahon, G. Williams, R. Harcourt, I. C. Field, L. Chafik, K. W. Nicholls, L. Boehme, and M. A. Fedak (2013), Estimates of the Southern Ocean general circulation improved by animal-borne instruments, *Geophysical Research Letters*, *40*(23), 6176–6180.

Schodlok, M. P., D. Menemenlis, E. Rignot, and M. Studinger (2012), Sensitivity of the ice-shelf/ocean system to the sub-ice-shelf cavity shape measured by nasa icebridge in pine island glacier, west antarctica, *Annals of Glaciology*, *53*(60), 156–162.

St-Laurent, P., J. M. Klinck, and M. S. Dinniman (2013), On the Role of Coastal Troughs in the Circulation of Warm Circumpolar Deep Water on Antarctic Shelves, *Journal of Physical Oceanography*, *43*(1), 51–64.

St-Laurent, P., J. M. Klinck, and M. S. Dinniman (2015), Impact of local winter cooling on the melt of Pine Island Glacier, Antarctica, *Journal of Geophysical Research: Oceans*, *120*(10), 6718–6732.

Steig, E. J., Q. Ding, D. S. Battisti, and A. Jenkins (2012), Tropical forcing of circumpolar deep water inflow and outlet glacier thinning in the amundsen sea embayment, west antarctica, *Annals of Glaciology*, *53*(60), 19–28.

Thoma, M., A. Jenkins, D. Holland, and S. Jacobs (2008), Modelling Circumpolar Deep Water intrusions on the Amundsen Sea continental shelf, Antarctica, *Geophysical Research Letters*, *35*(18), L18,602.

Thomas, R. H. (1979), The Dynamics of Marine Ice Sheets, *Journal of Glaciology*, *24*(90), 167 – 177.

Thompson, D. W. J., and J. M. Wallace (2000), Annular Modes in the Extratropical Circulation. Part I: Month-to-Month Variability*, *Journal of Climate*, *13*(5), 1000–1016.

Thurnherr, A. M., S. S. Jacobs, P. Dutrieux, and C. F. Giulivi (2014), Export and circulation of ice cavity water in Pine Island Bay, West Antarctica, *Journal of Geophysical Research: Oceans*, *119*(3), 1754–1764.

Treasure, A., F. Roquet, I. Ansorge, M. Bester, L. Boehme, H. Bornemann, J.-B. Charrassin, D. Chevallier, D. Costa, M. Fedak, C. Guinet, M. Hammill, R. Harcourt, M. Hindell, K. Kovacs, M.-A. Lea, P. Lovell, A. Lowther, C. Lydersen, T. McIntyre, C. McMahon, M. Muelbert, K. Nicholls, B. Picard, G. Reverdin, A. Trites, G. Williams, and P. N. de Bruyn (2017), Marine Mammals Exploring the Oceans Pole to Pole: A Review of the MEOP Consortium, *Oceanography*, *30*(2), 132–138.

Turner, J. (2004), The El Niñosouthern oscillation and Antarctica, *International Journal of Climatology*, *24*(1), 1–31.

Turner, J., A. Orr, G. H. Gudmundsson, A. Jenkins, R. G. Bingham, C. D. Hillenbrand, and T. J. Bracegirdle (2017), Atmosphere-ocean-ice interactions in the Amundsen Sea Embayment, West Antarctica.

Wåhlin, A. K., O. Kalén, L. Arneborg, G. Björk, G. K. Carvajal, H. K. Ha, T. W. Kim, S. H. Lee, J. H. Lee, and C. Stranne (2013), Variability of Warm Deep Water Inflow in a Submarine Trough on the Amundsen Sea Shelf, *Journal of Physical Oceanography*, *43*(10), 2054–2070.

Wåhlin, A. K., R. D. Muench, L. Arneborg, G. Björk, H. K. Ha, S. H. Lee, and H. Alsén (2012), Some Implications of Ekman Layer Dynamics for Cross-Shelf Exchange in the Amundsen Sea, *Journal of Physical Oceanography*, *42*(9), 1461–1474.

Wåhlin, A. K., X. Yuan, G. Björk, and C. Nohr (2010), Inflow of Warm Circumpolar Deep Water in the Central Amundsen Shelf, *Journal of Physical Oceanography*, *40*(6), 1427–1434.

Walker, D. P., M. A. Brandon, A. Jenkins, J. T. Allen, J. A. Dowdeswell, and J. Evans (2007), Oceanic heat transport onto the Amundsen Sea shelf through a submarine glacial trough, *Geophysical Research Letters*, *34*(2), L02,602.

Walker, D. P., A. Jenkins, K. M. Assmann, D. R. Shoosmith, and M. A. Brandon (2013), Oceanographic observations at the shelf break of the Amundsen Sea, Antarctica, *Journal of Geophysical Research: Oceans*, *118*(6), 2906–2918.

Webber, B. G. M., K. J. Heywood, D. P. Stevens, P. Dutrieux, E. P. Abrahamsen, A. Jenkins, S. S. Jacobs, H. K. Ha, S. H. Lee, and T. W. Kim (2017), Mechanisms driving variability in the ocean forcing of Pine Island Glacier, *Nature Communications*, *8*, 14,507.

Whitworth III, T., A. H. Orsi, S. J. Kim, W. D. Nowlin Jr., R. A. Locarnini, T. Whitworth III, and W. Nowlin Jr. (1998), Water masses and mixing near the Antarctic Slope Front, *Ocean, Ice, and Atmosphere: Interactions at the Antarctic Continental Margin*, *75*, 1–27.

Williams, G. D., L. Herraiz-Borreguero, F. Roquet, T. Tamura, K. I. Ohshima, Y. Fukamachi, A. D. Fraser, L. Gao, H. Chen, C. R. McMahon, R. Harcourt, and M. Hindell (2016), The suppression of Antarctic bottom water formation by melting ice shelves in Prydz Bay, *Nature Communications*, *7*, 12,577.

Zhang, X., A. F. Thompson, M. M. Flexas, F. Roquet, and H. Bornemann (2016), Circulation and meltwater distribution in the Bellingshausen Sea: From shelf break to coast, *Geophysical Research Letters*, *43*(12), 6402–6409.